BRNO UNIVERSITY OF TECHNOLOGY
VYSOKÉ UČENÍ TECHNICKÉ V BRNĚ

FACULTY OF MECHANICAL ENGINEERING
FAKULTA STROJNÍHO INŽENÝRSTVÍ

INSTITUTE OF PHYSICAL ENGINEERING
ÚSTAV FYZIKÁLNÍHO INŽENÝRSTVÍ

COOLING OF THERMAL MOTION OF OPTICALLY LEVITATED NANOOBJECTS

CHLAZENÍ TEPELNÉHO POHYBU OPTICKY LEVITUJÍCÍCH NANOOBJEKTŮ

MASTER'S THESIS
DIPLOMOVÁ PRÁCE

AUTHOR AUTOR PRÁCE	Bc. Tereza Zemánková
SUPERVISOR VEDOUCÍ PRÁCE	Mgr. Alexandr Jonáš, Ph.D.

BRNO 2023

Assignment Master's Thesis

Institut: Institute of Physical Engineering
Student: **Bc. Tereza Zemánková**
Degree programm: Physical Engineering and Nanotechnology
Branch: no specialisation
Supervisor: **Mgr. Alexandr Jonáš, Ph.D.**
Academic year: 2022/23

As provided for by the Act No. 111/98 Coll. on higher education institutions and the BUT Study and Examination Regulations, the director of the Institute hereby assigns the following topic of Master's Thesis:

Cooling of thermal motion of optically levitated nanoobjects

Brief Description:

Optical levitation harnesses the transfer of momentum between photons and a nanoobject to stably confine the nanoobject in air or in vacuum using a laser beam. An idealized model of light–nanoobject interaction describes the optically trapped object as a system of three independent damped harmonic oscillators vibrating in mutually orthogonal directions with generally different frequencies. According to the fluctuation–dissipation theorem (FDT), collisions between the levitated nanoobject and molecules of the ambient medium (thermal noise) randomly drive the oscillators and, at the same time, damp their motion. In equilibrium, the energy of each oscillator is determined by the effective temperature of the environment. Application of an external force acting against the instantaneous direction of oscillators' motion leads to dissipation of their kinetic energy through effective friction that is decoupled from the viscous environment surrounding the nanoobject. This approach allows circumventing the FDT and removing mechanical energy from the levitated object, eventually cooling its motion to the ground–state level of a quantum oscillator. Cooling of thermal motion of a charged nanoobject can be realized using an external electric field controlled by a feedback loop that adjusts the intensity and direction of the field according to the actual measured kinetic state of the nanoobject. The above described experimental methodology will allow realizing a number of unique experiments providing quantitative insight into the properties of microscopic stochastic systems and their transition from the classical to the quantum dynamical regime. Experimental work will be carried out in the Department of Microphotonics of the Institute of Scientific Instruments of the CAS in Brno.

Master's Thesis goals:

1) Insight into optical levitation of nanoobjects and their response to controlled external forces.
2) Realization and operation of an experimental setup allowing the study of selected processes.
3) Comparison of obtained experimental results with theoretical models and numerical simulations.

Recommended bibliography:

J. MILLEN et al. Optomechanics with levitated particles. Rep. Prog. Phys 83, 026401, 2020

P. JONES, O. MARANGO, G. VOLPE. Optical tweezers – Principles and application, Cambridge University Press, 2015

L. MAGRINI. Quantum measurement and control of mechanical motion at room temperature. PhD Thesis, University of Vienna, 2021

Deadline for submission Master's Thesis is given by the Schedule of the Academic year 2022/23

In Brno,

L. S.

prof. RNDr. Tomáš Šikola, CSc. Director of the Institute	doc. Ing. Jiří Hlinka, Ph.D. FME dean

Summary

The master's thesis deals with optical levitation of dielectric nanoparticles and cooling of their thermal motion. By focusing two counter-propagating laser beams, the particle can be stably trapped between the foci of the two beams. By subsequently applying an external electric field to the optically trapped charged particle and properly adjusting the feedback loop, it is possible to remove energy from the particle, reduce its position variance, and thus cool the particle thermal motion. The thesis is divided into three main chapters. The first discusses the theoretical introduction to optical trapping, describes the dynamics of the trapped particle, and connects it to the experimental section. A schematic of the experimental setup, preparation of particles for experiments, detection of the particle position, instructions on how to properly tune the optical setup, and calibration of the data to SI units are described. In the second part, various methods of cooling the thermal motion of an optically levitating particle are presented. Experiments performed with a single captured particle are compared with the theoretical model. In a laser beam with circular profile, the particle was cooled in one axis and the elliptical profile of the beam allowed cooling the thermal motion of the particle in two axes. In the third part, the trapping and interaction of two levitating particles, the formation of normal modes and their subsequent cooling are discussed. The experimentally obtained data are compared with theoretical models.

Abstrakt

Diplomová práce se zabývá optickou levitací dielektrických nanočástic a chlazením jejich tepelného pohybu. Zafokusováním dvou protiběžných laserových svazků lze částici stabilně zachytit mezi ohnisky obou svazků. Následnou aplikací vnějšího elektrického pole na opticky zachycenou nabitou částici a správným nastavením zpětnovazebné smyčky je možné částici odebírat energii, zmenšovat její varianci polohy, a tedy chladit tepelný pohyb částice. Práce je rozdělena do tří hlavních kapitol. V první je rozebrán teoretický úvod do optického chytání, popsána dynamika zachycené částice a propojení s experimentální částí. Je zde popsáno schéma experimentální sestavy, příprava částic pro experimenty, detekce polohy částice, návod, jak správně optickou sestavu naladit, a kalibrace dat na jednotky SI. Ve druhé části jsou uvedeny různé způsoby chlazení tepelného pohybu opticky levitující částice. Experimenty provedené s jednou zachycenou částicí jsou porovnány s teoretickým modelem. V laserovém svazku s kruhovým profilem byla částice chlazena v jedné ose a eliptický profil svazku umožnil chladit tepelný pohyb částice ve dvou osách. Ve třetí části je rozebráno zachycení a interakce dvou levitujících částic, vznik normálních módů a jejich následné chlazení. Experimentálně získaná data jsou porovnána s teoretickými modely.

Keywords
optical levitation, cooling by an electric field, optical binding, stochastic motion, harmonic oscillator

Klíčová slova
optická levitace, chlazení elektrickým polem, optická vazba, stochastický pohyb, harmonický oscilátor

ZEMÁNKOVÁ, T. *Chlazení tepelného pohybu opticky levitujících nanoobjektů.* Brno: Vysoké učení technické v Brně, Fakulta strojního inženýrství, 2023. 83 s. Vedoucí Mgr. Alexandr Jonáš, Ph.D.

I declare that I have written my Master's thesis entitled *Cooling of thermal motion of optically levitated nanoobjects* independently under the supervision of Mgr. Alexandr Jonáš, Ph.D. and exclusively using cited sources, literature, and other professional sources listed at the end of this thesis.

Bc. Tereza Zemánková

At this point, I would like to thank my supervisor Mgr. Alexandr Jonáš, Ph.D. for his help in the preparation of this thesis, his patience and willingness to provide valuable and very useful advices and comments.

I am gratefull to the Institute of Scientific Instruments of the Czech Academy of Sciences to work at its labarotories and the entire Team of levitation photonics at for their support and kind approach. Special thanks go to Mgr. Oto Brzobohatý, Ph.D. for his guiding regarding the evaluation of the experimental data of two particles and to Ing. Petr Jákl, Ph.D. for his advices regarding DMD and software control of the experimental set-up.

Finally, I would like to thank very much my parents and my whole family for their support during my studies.

Bc. Tereza Zemánková

Contents

1. Introduction

Optical manipulations refer to the use of the momentum of light for trapping and manipulation of objects of micro- and nanometer dimensions. Upon illumination with suitably shaped laser beams, such objects can be sorted, transported in space, and self-organized. The history of optical trapping started in the 1970s when Arthur Ashinkin conducted his seminal experiments exploiting the transfer of momentum between light and small particles. In these experiments, he used a moderately focused laser beam that illuminated particles suspended in water. He demonstrated that the beam moved the particles in the direction of light propagation and, simultaneously, pulled them to the most intense region of the beam located on its axis [1]. To stably confine dielectric particles at a fixed spatial location in aqueous suspensions, he used the geometry of two counter-propagating laser beams in which radiation pressure forces compensated each other. A year later, he introduced optical levitation of microscopic particles in air and vacuum, where the radiation pressure of a laser beam pointing upwards was compensated by the weight of the particle [2]. The most significant discovery of A. Ashkin in the field of optical manipulation was the introduction of the so-called optical tweezers [3, 4], which use a single strongly focused laser beam to trap an illuminated particle in all three dimensions via all-optical forces. Optical tweezers have become an invaluable tool in various branches of natural sciences, as they enable contactless and non-destructive handling of objects with micrometer and submicrometer dimensions, e.g., bacteria, viruses, living cells or subcellular organelles. In addition, they also allow measuring the very weak forces generated by various kinds of molecular motors operating inside living cells [5].

In the last decade, optical manipulation experiments expanded into the novel direction of optical levitation of nanoparticles in a vacuum, also known as levitated optomechanics. While the previous manipulation activities mainly focused on handling objects suspended in liquids, in levitated optomechanics, the trapped objects are located in air or in an environment with lower pressure than atmospheric. It turns out that at ambient pressures around 10^{-6} mbar and lower, the interaction of the trapped particle with the gas molecules is strongly suppressed and the main interaction with the environment is mediated by the photons of the laser beam scattered by the object. A momentum exchange between the photons and the object is responsible for the optical trapping; however, at the same time, the randomness of the scattering events causes the main contribution to the stochastic nature of this interaction and, consequently, to the heating of object's mechanical degrees of freedom. Therefore, at low pressure, the levitating particle behaves as a stochastically driven underdamped mechanical oscillator with a very narrow resonant frequency and a very high quality factor [6]. By extracting the mechanical energy of the trapped oscillating particle, it is possible to bring it from the classical to the quantum dynamical regime. This opens up a unique possibility to obtain a mesoscopic version of a quantum oscillator and investigate quantum-mechanical phenomena using a relatively massive object. In addition, optically levitated and cooled particles can serve as an attractive experimental platform for testing fundamental ideas of statistical mechanics and for implementing highly sensitive detection schemes for characterizing extremally weak static and dynamic interaction forces [7]. Currently, there exist multiple experimental strategies for reducing the effective kinetic temperature of the center-of-mass motion of the trapped particle that operate either autonomously or with the assistance of external feedback loops that monitor the particle position. Among these different approaches to particle cooling, cold damping of the motion of a charged particle in a controlled external electric field has demonstrated the feasibility of reaching the ground state of the particle mechanical motion [8, 9].

In my diploma thesis, I experimentally investigated cold damping of the thermal motion of optically levitated charged nanoparticles in one or two dimensions, using an experimental set-up built around a dual-beam optical trap complemented by a system of electrodes that allowed applying an external electric field to the trapped particles. The cooled particles (one or two) were stably confined in vacuum in counter-propagating laser beams, dynamically generated by a digital micromirror device, and subjected to an electric field whose magnitude and direction were controlled by an electronic feedback loop to be proportional to the instantaneous velocity of the particles. Following the experiments, the recorded trajectories of the cooled particles were analyzed using the power spectral density of the particle position to quantify the reduction of the thermal motion of the particles by evaluating their effective kinetic temperature T_{eff}. For a single trapped particle, the value of T_{eff} was directly proportional to the variance of the particle position, whereas for two simultaneously trapped particles coupled by optical binding, T_{eff} was derived from the coordinates of the normal modes of particles' oscillation. My overall goal was to create a tool for cooling the thermal motion of optically levitated particles that would allow reaching the lowest possible value of T_{eff}. In the future, the results obtained in my diploma project will be used to approach the quantum ground state of the center-of-mass oscillatory motion of the particles and, in the case of two simultaneously levitated particles, to perform experiments directed towards investigation of quantum entanglement between mesoscopic objects.

2. Optical levitation and particle position detection

2.1. Optical trapping

In this section, the main motivation for using optically trapped nanoparticles as a model of nanomechanical oscillators will be provided and their main advantages in comparison to other experimental micromechanical platforms will be discussed. Subsequently, a theoretical description of the Gaussian laser beam, which is typically used for optical trapping experiments, will be introduced. Finally, the two basic geometries used most often for optical trapping of micro- and nanoobjects – optical tweezers and dual-beam optical trap – will be presented and the advantages of each method will be described.

2.1.1. Motivation

Optically levitated micro- and nanoparticles (MPs and NPs) [10] have recently gained more and more attention, serving as an attractive experimental platform for testing fundamental ideas of quantum physics [6, 11] and statistical mechanics [12, 13]. Levitated particles can also be used for implementing highly sensitive detection schemes for characterizing static and dynamic interaction forces and potentials on the nanometer spatial scale [7, 14, 15]. A small particle levitated in a focused laser beam or beams in vacuum represents a nano-mechanical oscillator whose stiffness can be dynamically controlled by shaping the intensity or phase profile of the trapping light [13]. An external force acting on the NP then results in its displacement, which can in turn serve to quantify the magnitude and dynamical profile of the force. Owing to their unique characteristics, nanomechanical oscillators optically levitated in vacuum have allowed achieving zepto-Newton sensitivity in detecting resonant forces [7] and atto-Newton sensitivity in mapping the spatial distribution of static gravitational and electric forces [15].

A huge advantage of optically levitated MPs or NPs – in comparison to other nanomechanical oscillators such as micromembranes, microcantilevers, or nanowires – is the fact that the levitated particles are not mechanically or thermally coupled to the rest of the experimental set-up. Consequently, they do not suffer from problems with the transfer of mechanical vibrations or heat from the bulk of the experimental set-up to the actual nano-mechanical oscillator under investigation. The only source of thermal decoherence in the levitated NPs case is the surrounding ambient atmosphere in the vacuum chamber; however, this potential disturbance can be largely eliminated by sufficiently reducing the ambient pressure. Hence, optically levitated NPs provide direct access to the observation of quantum-mechanical phenomena on the mesoscopic scale.

2.1.2. Gaussian laser beam

The main part of an optical trapping set-up is the laser beam, in which the MPs and NPs can be stably trapped. Most high-quality lasers emit an output beam in the form of the so-called TEM$_{00}$ mode, also known as the Gaussian laser beam. Using the paraxial approximation (meaning that the light propagates mostly in a single spatial direction that defines the optical axis of the system), the Gaussian beam can be mathematically expressed in the form [16]

$$\mathbf{E}(\rho, z) = \mathbf{E}_0 \frac{w_0}{w(z)} \mathrm{e}^{-\frac{\rho^2}{w^2(z)}} \mathrm{e}^{\mathrm{i}\left[kz - \eta(z) + \frac{k\rho^2}{2R(z)}\right]}, \tag{2.1}$$

where the optical axis coincides with the z-axis, $\mathbf{E}(\rho,\, \mathrm{z})$ is the electric field of the Gaussian beam, $\rho = \sqrt{x^2 + y^2}$ is the transverse polar coordinate related to the Cartesian coordinates $[x, y]$, w_0 is the so-called beam waist radius that characterizes the minimal transverse extent of the Gaussian beam along the propagation direction (located at $z = 0$, which defines the beam focal plane; see Fig. 2.1), i is the imaginary unit, $\mathbf{E}_0 = \mathbf{E}(0, 0)$ and the remaining quantities are defined as follows [16]

$$\begin{aligned} w(z) &= w_0 \sqrt{1 + \frac{z^2}{z_0^2}}, & (2.2)\\ R(z) &= z \left(1 + \frac{z_0^2}{z^2}\right), & (2.3)\\ \eta(z) &= \arctan\left(\frac{z}{z_0}\right), & (2.4) \end{aligned}$$

where $w(z)$ is the local transverse radius of the Gaussian beam, $R(z)$ is the radius of curvature of the beam wavefront, $\eta(z)$ represents the Gouy phase shift, and z_0 is the Rayleigh length, defined as $z_0 = k w_0^2/2$, where $k = n_1 2\pi/\lambda$ is the light wavenumber, n_1 is the refractive index of the surrounding medium and λ is the wavelength of light. Distance $2z_0$ then characterizes the axial range where the beam stays approximately collimated.

Another characteristic of the Gaussian beam is the angular divergence $\Theta_{1/2}$, which expresses how quickly the beam spreads with axial distance from $z = 0$ in both positive and negative directions. For $z \gg z_0$, $\Theta_{1/2}$ can be expressed in the form $\Theta_{1/2} = 2/(k w_0)$ [16].

The optical intensity $I(\rho, z)$ of the Gaussian beam can be expressed in the form of the following equation

$$I(\rho, z) = C\mathbf{E}(\rho, z) \cdot \mathbf{E}^*(\rho, z) = I_0 \frac{w_0^2}{w(z)^2} \mathrm{e}^{-\frac{2\rho^2}{w(z)^2}}, \tag{2.5}$$

where $C = n_1 \epsilon_0 c/2$ [17], c is the speed of light in vacuum, ϵ_0 is the vacuum permittivity and $I_0 = C|\mathbf{E}_0|^2$.

2.1.3. Origin of optical forces

In this subsection, the origin of optical forces acting on small particles illuminated by a laser beam will be explained for two opposite limiting cases: geometrical optics valid for particle sizes $a \gg \lambda$ and Rayleigh approximation valid for particle sizes $a \ll \lambda$. Despite their limited range of validity, these approximations provide an intuitive insight into the nature of the interaction between light and material objects.

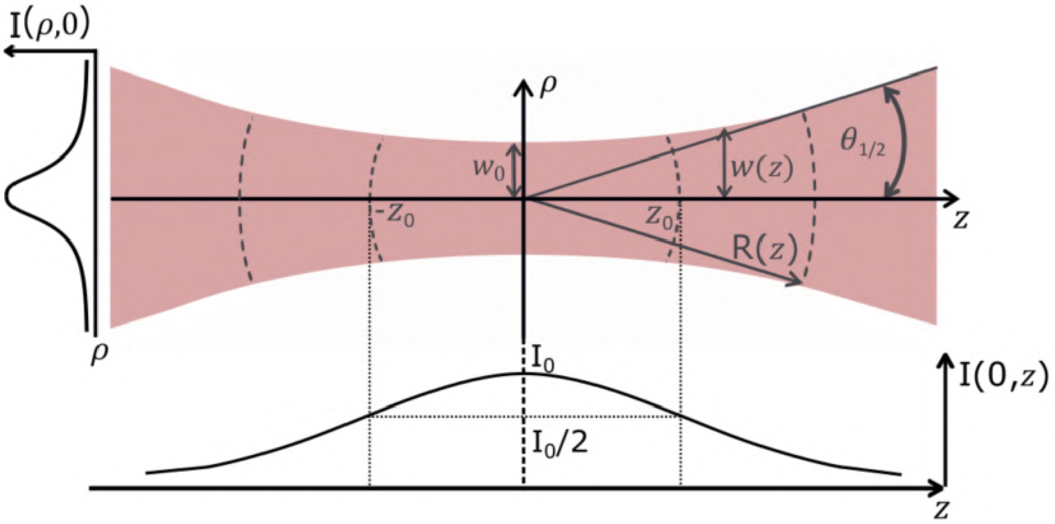

Figure 2.1: Schematic illustration of a Gaussian beam with the description of the most important propagation characteristics mathematically expressed in equations (2.2) – (2.4). The plots show the profiles of the beam intensity in the transverse direction ($I(\rho, 0)$) and axial direction ($I(0, z)$).

Optical forces in the geometrical optics approximation

The principles of geometrical optics can be used if the trapped particle is much larger than the wavelength λ of the trapping beam and the wave nature of light can be neglected [18]. Geometrical optics represents the light beam as a bundle of optical rays along which streams of photons propagate. The momentum $\mathbf{p}$ of each photon can be expressed by the relation $\mathbf{p} = \hbar\mathbf{k}$, where $\hbar$ is the reduced Planck constant and $\mathbf{k}$ is the wave vector of the incident light in the surrounding medium.

The origin of optical forces is illustrated by Fig. 2.2. To derive the optical force acting on an illuminated particle, the transfer of momentum to the particle from the incident and transmitted photons is considered. For the sake of simplicity, let us assume a dielectric particle with a negligible reflectivity, i.e. virtually all incident photons are refracted at the particle surface. These refracted photons change the direction of propagation with respect to the incident photons, which results in a change in the light momentum assigned to the given ray. Based on the validity of the law of conservation of total momentum for the joint system "particle + light", it can be established that a change in the momentum of photons also leads to a change in the momentum of the particle that is equal in magnitude and opposite in direction. According to Newton's second law, the change $\Delta\mathbf{p}_{\text{ray}}$ in the net momentum of incident photons representing a given light ray, caused by the refraction of the ray from the particle, is related to the net force $\mathbf{F}_{\text{ray}}$ acting on the ray photons as $\mathbf{F}_{\text{ray}} = \Delta\mathbf{p}_{\text{ray}}/\Delta t$. Here, Δt represents the time interval in which the momentum change occurs. Newton's third law then requires that the refracted photons must exert an equal and oppositely oriented optical force $\mathbf{F}_{\text{opt}} = -\mathbf{F}_{\text{ray}}$ on the particle. The optical force $\mathbf{F}_{\text{opt}}$ due to the given ray can be written in a simplified form [18] as $\mathbf{F}_{\text{opt}} = P\frac{n_1\mathbf{Q}}{c}$, where P denotes the total power associated with the ray, c is the light speed in vacuum, n_1 is the refractive index of the surrounding medium, and $\mathbf{Q}$ is a vector indicating the direction of force action for the particular ray. The total resulting optical force $\mathbf{F}_{\text{opt}}^{\text{net}}$ acting on the particle is then the vector sum of the force contributions from the individual incident rays. This force depends on the geometry of the incident light beam and the shape and material of the particle.

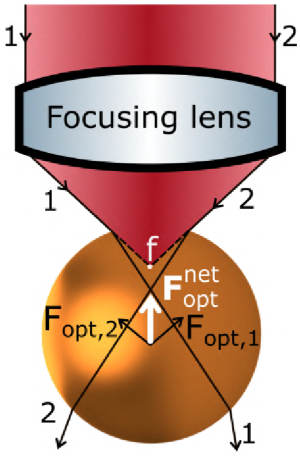

Figure 2.2: Illustration of the origin of optical forces in the geometrical optics regime. From the focused incident laser beam, only two symmetrically located extreme rays 1 and 2 are shown, which have the greatest force effect on the illuminated particle. The optical forces $\mathbf{F}_{\mathrm{opt},1}$ and $\mathbf{F}_{\mathrm{opt},2}$ arise due to the refraction of rays 1 and 2 on the particle. The resulting optical force $\mathbf{F}^{\mathrm{net}}_{\mathrm{opt}}$ acting on the particle is the vector sum of $\mathbf{F}_{\mathrm{opt},1}$ and $\mathbf{F}_{\mathrm{opt},2}$. For the given geometry of the focused laser beam and position of the particle with respect to the beam focus f, the net force $\mathbf{F}^{\mathrm{net}}_{\mathrm{opt}}$ from the two extreme rays points towards the focus.

Optical forces in the Rayleigh approximation

The Rayleigh approximation can be used when the radius a of the trapped particle is much smaller than the wavelength λ of the incident laser beam [18]. Typically, it is assumed that the radius of the particle fulfills $a \leq \lambda/20$ [17]. The illuminated particle is then understood as an induced electric dipole with dipole moment $\mathbf{p}(\mathbf{r}) = \alpha\mathbf{E}(\mathbf{r})$, where α is the complex polarizability of the particle and $\mathbf{E}(\mathbf{r})$ is the intensity of the electric field at the particle location $\mathbf{r}$. The polarizability of the particle can be expressed in the following form [19]

$$\alpha = \alpha' + \mathrm{i}\alpha'' = \frac{\alpha_0}{1 - \frac{2}{3}\frac{\mathrm{i}k^3\alpha_0}{4\pi\epsilon_0\epsilon_1}} \simeq \alpha_0 + \mathrm{i}\frac{|\alpha_0|^2 k^3}{6\pi\epsilon_0\epsilon_1}, \tag{2.6}$$

$$\alpha_0 = 4\pi a^3 \epsilon_0 \frac{\epsilon_2 - \epsilon_1}{\epsilon_2 + 2\epsilon_1}, \tag{2.7}$$

where α' and α'' is the real and imaginary part of the polarizability, respectively, k is the wavenumber, ϵ_0 is the vacuum permittivity, ϵ_1 is the relative permittivity of the surrounding medium, and ϵ_2 is the relative permittivity of the particle.

Let us write the components of the complex electric field as $E_m = E'_m \mathrm{e}^{\mathrm{i}\phi'}$, where E'_m is the real amplitude and ϕ' is the real phase of the field ($m \in \{x, y, z\}$). The components $F_m(\mathbf{r})$ of the resulting optical force acting on a Rayleigh particle along the axis m can then be expressed in the following form [19]

$$F_m(\mathbf{r}) = \frac{1}{4}\alpha' \sum_{j=x,y,z} \frac{\partial(E'^2_j(\mathbf{r}))}{\partial r_m} + \frac{1}{2}\alpha'' \sum_{j=x,y,z} E'^2_j(\mathbf{r}) \frac{\partial \phi'(\mathbf{r})}{\partial r_m}. \tag{2.8}$$

Equation (2.8) for the net optical force can be divided into two parts corresponding to two force components with different properties. Specifically, the first part of Eq. (2.8) represents the *gradient* force that is proportional to the real part of the particle polarizability α' and to the gradient of the optical intensity. Depending on the sign of α', the gradient force points either to the location of the highest optical intensity ($\alpha' > 0$ or $\epsilon_2 > \epsilon_1$) or away from it ($\alpha' < 0$ or $\epsilon_2 < \epsilon_1$). Thus, particles with relative permittivity higher than that of the surrounding medium are attracted towards the intensity maximum, whereas low-permittivity particles are repelled from the maximum. The second part of Eq. (2.8) then represents the *scattering* force (radiation pressure) that is proportional to the imaginary part of the particle polarizability α'', the optical intensity, and the gradient of the light wave phase. For an incident Gaussian beam, the scattering force always points in the direction of the beam propagation, regardless of the relationship between ϵ_1 and ϵ_2. Spatial profiles of the gradient and scattering forces for a Rayleigh particle with $\epsilon_2 > \epsilon_1$ illuminated with a focused Gaussian beam are illustrated in the Fig. 2.3.

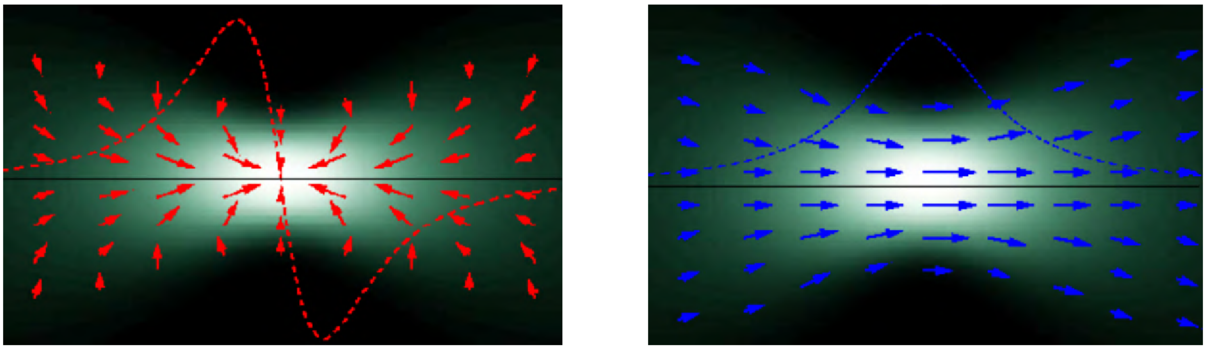
(a) (b)

Figure 2.3: Graphical representation of (a) the gradient forces and (b) the scattering forces (radiation pressure) acting on a very small particle (a point dipole) located in the vicinity of the intensity maximum of a focused Gaussian trapping beam. The arrows in the plots represent the direction of the forces (the direction of the arrows) and the local strength of the forces (the length of the arrows – the longer the arrow the greater the magnitude of the force) at different locations in the focused laser beam that is shown in the background. Gradient forces act along both transverse and longitudinal directions and pull the particle to the place of the greatest optical intensity (the brightest spot), if the particle has greater relative permittivity than the surrounding medium. On the other hand, the scattering force always pushes the particle in the direction of the beam propagation.

2.1.4. Geometries used for optical trapping

In the field of optical levitation, two different configurations for the optical confinement of small particles are typically used. The first, known as the optical tweezers (OT), uses a single, highly focused laser beam to trap the particle. Alternatively, particles can be confined in the dual-beam trap formed by two counter-propagating beams, which can be either interfering or non-interfering. The following section describes the main characteristics of both trapping schemes and compares their principal advantages and limitations.

Optical tweezers

Optical tweezers (OT) use a single strongly focused laser beam to achieve stable three-dimensional confinement of a particle with a relative permittivity higher than that of the surrounding medium, as illustrated in Fig. 2.4. For this reason, high numerical aperture lenses are used to focus the trapping beam. In the OT configuration, the optical forces are typically much stronger than the gravitational force acting on the trapped particle, so this force does not have a significant effect on the trapping.

In the terminology of the Rayleigh approximation (see Section 2.1.3), the gradient force will stably confine the particle in the transverse direction, pulling the particle towards the beam axis (see Fig. 2.4(a)). In the longitudinal direction, the particle will be trapped at an equilibrium position determined by the balance between the gradient and scattering force. In general, this equilibrium position will be displaced from the beam focal plane in the direction of the beam propagation (see Fig. 2.4(b)).

The main advantages of the OT are simple experimental implementation, the need for fewer optical components (which translates into a lower cost of the experimental setup), better thermal stability for long-term trapping experiments, and precise spatial localization of the trapped particle. The principal limitation of the OT results from the asymmetry of the longitudinal trapping potential caused by the unbalanced scattering force (see Fig. 2.4(b)), which decreases the overall stability of trapping and imposes practical limitations on the size range of particles that can be stably confined. Specifically, in the optical levitation experiments carried out with the OT in vacuum, the diameter of the trapped particles is typically restricted from above to a few hundred of nm [6]. In addition, the OT can capture only one particle in its single trapping location.

Dual-beam trap

A dual-beam trap is formed by two laser beams propagating against each other along a common axis (see Fig. 2.5). In the transverse direction, the stability of the particle is ensured by the gradient force, as in the case of OT. In the longitudinal direction, the cancellation of scattering forces from both beams (if we consider beams with the same spatial profiles and total powers) ensures symmetrization of the trapping potential and contributes to stable capture. The actual profile of the longitudinal trapping potential then depends on the polarization state of the two trapping beams. Let us assume that both beams are linearly polarized and have equal powers. If the beam polarizations are mutually perpendicular, the beams do not interfere and a cross-polarized (CP) dual-beam optical trap is formed (Fig. 2.5(a)). In this case, the particles are confined at a single trapping location on the common optical axis of the two beams, situated symmetrically between the beam focal planes. On the other hand, if the beam polarizations are parallel to each other, the beams interfere and a standing wave (SW) optical trap is created (Fig. 2.5(b)). In this interference structure, multiple stable trapping locations exist along the optical axis. Depending on their size, the trapped particles can be captured either in the interference maxima or minima. Moreover, there exist specific particle sizes that are not affected by the standing wave at all [20].

The main advantage of dual-beam optical traps is the possibility of stable confinement of particles over wider ranges of sizes and refractive indices, using moderately focused laser beams. With these more stable traps, trap loading is a significantly easier task, especially in underdamped conditions typically encountered in vacuum optical levitation experi-

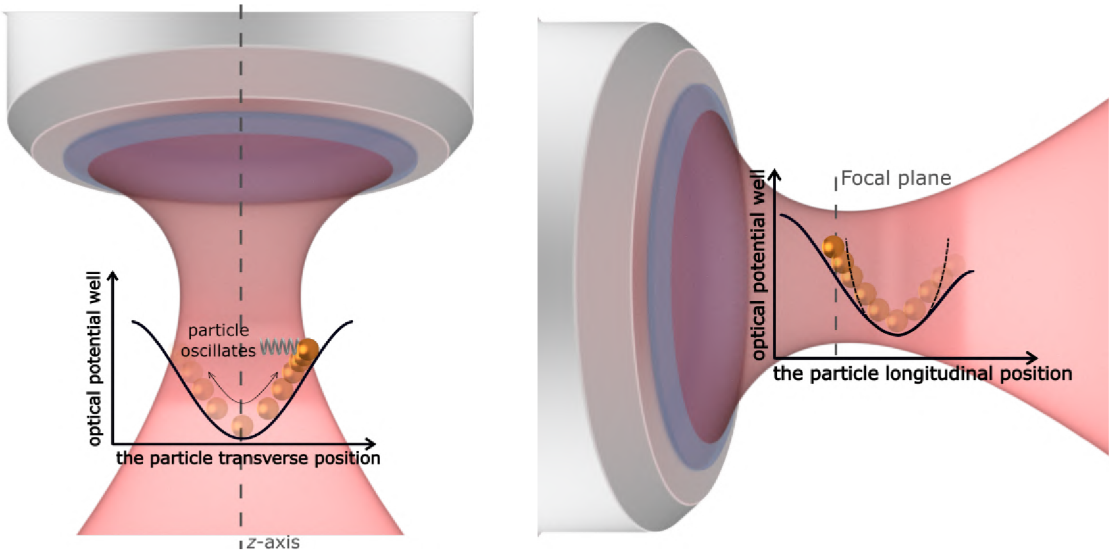

(a) (b)

Figure 2.4: A schema of optical trapping of a particle (orange ball) using the optical tweezers (OT) geometry. To achieve three-dimensional confinement of the particle, OT uses a laser beam that is tightly focused by a lens with a high numerical aperture. Figure insets show the profiles of the optical trapping potential in (a) the transverse direction and (b) the longitudinal direction. (a) In the transverse direction, the particle is confined on the beam axis by the gradient force. For small displacements from the trap center, the trapped particle can be described as a harmonic oscillator with a certain stiffness (represented by a spring). The motion of the particle in the trap during one-half of the oscillation period is represented by different shades of the orange ball (the darkest color at the beginning, gradually fading with increasing time). (b) In the longitudinal direction (beam axis direction), the particle is stably trapped at an equilibrium position determined by the balance between the gradient and scattering forces. Due to the spatial profiles of these two force components (see Fig. 2.3), the longitudinal trapping potential is not symmetric; the scattering force reduces the depth of the longitudinal potential well on the side located behind the focus (in the beam propagation direction). This reduced potential depth represents the typical escape route of the particle from the trap. For comparison, the dashed line shows the profile of an ideal harmonic potential well that approximates the real longitudinal potential for small displacements from the equilibrium position.

ments. In the SW traps, the interference of counter-propagating trapping beams leads to the generation of steep axial gradients of optical intensity. These intensity gradients then enable the formation of optical traps with greater stiffness and depth than a single-beam OT with the same total trapping power. Moreover, in the SW trap, multiple particles can be simultaneously confined in adjacent trapping locations. Drawbacks of dual-beam optical trapping are associated with a greater complexity of experimental realization that leads to challenges with the correct alignment of the trap and more expensive implementation (all components are needed twice).

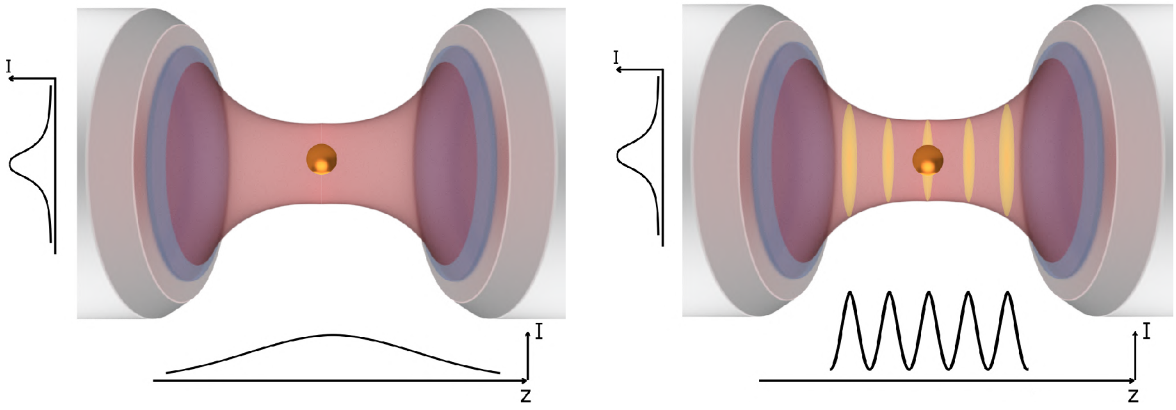

(a) (b)

Figure 2.5: A schema of optical trapping of a particle (orange ball) using the geometry of two counter-propagating trapping beams. (a) Cross-polarized case: the two trapping beams have their electric field vectors oriented along mutually perpendicular directions and, thus, do not interfere with each other. In the transverse direction, optical trapping is provided by the gradient force as in the case of the single-beam OT. In the longitudinal direction, the stability of the particle is enhanced by the cancellation of the radiation pressure forces from both laser beams. Spatial profiles of the optical intensity I in the lateral and longitudinal directions are drawn. (b) Creation of an optical standing wave due to the interference of two coherent trapping beams with parallel polarizations. Orange ellipses indicate the adjacent interference maxima. Depending on their size, the particles are trapped by the longitudinal optical gradient forces either in the interference maxima (shown in the picture) or in the minima. For certain particle sizes, the net longitudinal optical force is zero regardless of the particle position.

2.2. Underdamped dynamics of optically levitated particle

In this section, the dynamics of the thermal motion of a particle trapped in a harmonic potential well will be characterized. First, the stochastic Langevin equation of particle motion driven by random collisions with the ambient molecules (Brownian motion) will be formulated. The solution to the Langevin equation using the power spectral density will then be outlined. Finally, the characterization of the particle motion via histograms of the particle position will be introduced. For the sake of simplicity, all formulas in this section will be analyzed for the one-dimensional (1D) case, with a straightforward extension to all three dimensions.

2.2.1. Langevin equation

The Langevin equation (LE) is a stochastic differential equation of motion based on Newton's laws of motion. It describes the dynamics of a small particle moving under the influence of randomly acting forces originating in the thermal environment. One of the well-known examples of this system is the Brownian motion of a small particle immersed in a liquid [21].

A particle optically trapped in a low vacuum can be modeled as a thermally driven underdamped harmonic oscillator [22]. Thus, its 1D Langevin equation of motion can be written in the form

$$m\ddot{x}(t) + \gamma\dot{x}(t) + m\omega_{0x}^2 x(t) = F_{\text{th}}(t), \tag{2.9}$$

where $x(t)$ is the position of the particle, m is the mass of the particle, γ is the friction coefficient, ω_{0x} is the resonant frequency in the form: $\omega_{0x} = \sqrt{\frac{\kappa_x}{m}}$, where κ_x is the stiffness of the harmonic potential well, and $F_{\text{th}}(t)$ is the thermal Langevin force depending on the ambient temperature T and on γ.

The motion of the trapped particle is influenced by three forces acting on it:

1. Viscous drag F_{visc} (deterministic force), which causes the dynamic friction and slows down the particle motion (second term on the left-hand side of Eq. (2.9): $F_{\text{visc}} = -\gamma\dot{x}(t)$). For a spherical particle with the radius a, the friction coefficient γ can be expressed in the form of Stokes' law

$$\gamma = 6\pi\eta a, \tag{2.10}$$

   where η is the dynamic viscosity of the surrounding medium.
2. Harmonic confinement force F_{trap} caused by the trapping potential well (the third term on the left-hand side of Eq. (2.9): $F_{\text{trap}} = -m\omega_{0x}^2 x(t)$).
3. Stochastic Langevin force $F_{\text{th}}(t)$, which rapidly fluctuates in comparison to $x(t)$. It arises from random collisions between the ambient molecules in the vacuum chamber and the trapped particle. In our case $F_{\text{th}}(t)$ has a white-noise spectral distribution and can be described by the following equations [21]

$$\langle F_{\text{th}}(t)\rangle = 0, \tag{2.11}$$

$$\langle F_{\text{th}}(t)F_{\text{th}}(t')\rangle = 2\gamma k_{\text{B}}T\delta(t-t'), \tag{2.12}$$

   where k_{B} is the Boltzmann constant, $2\gamma k_{\text{B}}T$ defines the power spectral density of $F_{\text{th}}(t)$ that can be calculated from the Wiener-Khinchin theorem (more information in Section 2.2.2), $\delta(t-t')$ is the Dirac delta function, which expresses that there is no connection between two collisions at different times t and t', and $\langle\rangle$ indicates the statistical ensemble average over different realizations[1]. The Langevin force drives the particle motion.

Using Eq. (2.12), friction coefficient γ can be related to the stochastic Langevin force $F_{\text{th}}(t)$ via the fluctuation-dissipation theorem, which can be written as [21]

$$\gamma = \frac{1}{k_{\text{B}}T}\int_0^\infty \langle F_{\text{th}}(t)F_{\text{th}}(t+\tau)\rangle d\tau, \tag{2.13}$$

where $t' = t + \tau$.

2.2.2. Solution of the Langevin equation

The power spectral density (PSD) of the stochastic force $F_{\text{th}}(t)$ can be calculated using the Wiener-Khinchin theorem, which states that the autocorrelation function $\langle F_{\text{th}}(t)F_{\text{th}}(t+\tau)\rangle$

---

[1] For a continuous random variable x, mean value can be generally defined as : $\langle x\rangle = \int_{-\infty}^{\infty} xp(x)dx$, where $p(x)$ is the probability density.

of $F_{\mathrm{th}}(t)$ and its power spectral density $S_{F_{\mathrm{th}}}(\omega)$ form a Fourier transform pair. The mathematical form of the Wiener-Khinchin theorem is expressed by equations [21, 23]

$$\begin{aligned} \langle F_{\mathrm{th}}(t)F_{\mathrm{th}}(t+\tau)\rangle &= \frac{1}{2\pi}\int_{-\infty}^{\infty} S_{F_{\mathrm{th}}}(\omega)e^{\mathrm{i}\omega\tau}d\omega, &(2.14)\\ S_{F_{\mathrm{th}}}(\omega) &= \int_{-\infty}^{\infty}\langle F_{\mathrm{th}}(t)F_{\mathrm{th}}(t+\tau)\rangle e^{-\mathrm{i}\omega\tau}d\tau, &(2.15)\end{aligned}$$

where i is the imaginary unit and ω is the angular frequency.

Using Eq. (2.12) together with Eq. (2.15) and substitution $t' = t+\tau$, we get the PSD of the Langevin force in the form

$$S_{F_{\mathrm{th}}}(\omega) = \int_{-\infty}^{\infty}\langle F_{\mathrm{th}}(t)F_{\mathrm{th}}(t+\tau)\rangle e^{-\mathrm{i}\omega\tau}d\tau = 2\gamma k_{\mathrm{B}}T\int_{-\infty}^{\infty}\delta(\tau)e^{-\mathrm{i}\omega\tau}d\tau = 2\gamma k_{\mathrm{B}}T, \tag{2.16}$$

where we used the definition of the Fourier transform of δ-function, $\int_{-\infty}^{\infty}\delta(\tau)e^{-\mathrm{i}\omega\tau}d\tau = 1$.

In order to find the PSD $S_x(\omega)$ of the particle position x, LE is first expressed in the frequency domain by Fourier-transforming Eq. (2.9) as

$$-\omega^2\hat{x}(\omega) + \mathrm{i}\Gamma\omega\hat{x}(\omega) + \omega_{0x}^2\hat{x}(\omega) = \frac{\hat{F}_{\mathrm{th}}(\omega)}{m}, \tag{2.17}$$

where $\Gamma = \gamma/m$ is the viscous damping rate, $\hat{F}_{\mathrm{th}}(\omega)$ and $\hat{x}(\omega)$ is the Fourier transform of $F_{\mathrm{th}}(t)$ and $x(t)$, respectively:

$$\hat{F}_{\mathrm{th}}(\omega) = \int_{-\infty}^{\infty}F_{\mathrm{th}}(t)e^{-\mathrm{i}\omega t}dt, \quad \hat{x}(\omega) = \int_{-\infty}^{\infty}x(t)e^{-\mathrm{i}\omega t}dt. \tag{2.18}$$

It is then possible to solve Eq. (2.17) for $\hat{x}(\omega)$ and obtain

$$\hat{x}(\omega) = \frac{\hat{F}_{\mathrm{th}}(\omega)}{m(\omega_{0x}^2 - \omega^2 + \mathrm{i}\Gamma\omega)} = \hat{F}_{\mathrm{th}}(\omega)\chi_{\mathrm{m}}(\omega), \tag{2.19}$$

where $\chi_{\mathrm{m}}(\omega) = [m(\omega_{0x}^2 - \omega^2 + \mathrm{i}\Gamma\omega)]^{-1}$ is the complex mechanical susceptibility that characterizes the response of the harmonic oscillator to external forces. We can use Eq. (2.16) to express the power spectral density of particle position as [21]

$$S_x(\omega) = \lim_{T_{\mathrm{m}}\to\infty}\frac{1}{T_{\mathrm{m}}}\hat{x}(\omega)\hat{x}(\omega)^* = \frac{1}{m^2}\frac{S_{F_{\mathrm{th}}}(\omega)}{[(\omega_{0x}^2-\omega^2)^2+\Gamma^2\omega^2]} = \frac{1}{m}\frac{2\Gamma k_{\mathrm{B}}T}{[(\omega_{0x}^2-\omega^2)^2+\Gamma^2\omega^2]}, \tag{2.20}$$

where * is the complex conjugation and T_{m} corresponds to the time of the measurement. The PSD of the particle position in the form of Eq. (2.20) fully describes the dynamics of the trapped particle in the frequency domain. Maximum of the power spectrum describes the following equation

$$\omega^2 = \omega_0^2 - \frac{\Gamma^2}{2}. \tag{2.21}$$

The model done by Eq. (2.20) is used to fit the experimental data [24] and the main parameters of the system (ω_{0x}, Γ, T) can be obtained. This approach will be used in the experimental part of Section 2.6. By integrating the area under $S_x(\omega)$ over angular frequency from $-\infty$ to ∞, we can obtain the variance $\langle x^2\rangle$ of the particle motion

$$\langle x^2\rangle = \frac{1}{2\pi}\int_{-\infty}^{\infty} S_x(\omega)d\omega = \frac{k_\mathrm{B}T}{m\omega_{0x}^2}. \tag{2.22}$$

This result is identical to the value predicted by the equipartition theorem for a harmonic oscillator with the resonant eigenfrequency ω_{0x} and mass m that is in thermodynamic equilibrium with the ambient thermal bath at temperature T.

Equation (2.22) can be formally adopted also for the case of an oscillating particle subjected to an external dissipative force that cools the motion of the particle. Specifically, in the steady state when the variance $\langle x^2\rangle$ of the particle position $x(t)$ is known, Eq. (2.22) can be rearranged to define the *effective* kinetic temperature T_eff as

$$T_\mathrm{eff} = \frac{m\omega_{0x}^2\langle x^2\rangle}{k_\mathrm{B}}. \tag{2.23}$$

2.2.3. Probability distribution of the particle position

The probability distribution of the particle position can be reconstructed from the *position histogram* (see Fig. 2.6 for illustration). Histogram is a graphical representation of the recorded trajectory that sorts all observed positions into bins of a specific width dx, located at discrete positions x_i. The height $H(x_i)$ of each histogram bin represents the number of times the particle trajectory crossed the position interval $\langle x_i; x_i+dx\rangle$ associated with the given bin. Specifically, the probability $P(x_i)$ of finding the particle in interval $\langle x_i; x_i+dx\rangle$ can be determined from $H(x_i)$ as

$$P(x_i) = \frac{H(x_i)}{\sum_i H(x_i)} = \int_{x_i}^{x_i+dx} p(x)dx, \tag{2.24}$$

where the summation runs over all histogram bins and $p(x)$ denotes the probability density. In order to apply Eq. (2.24), one must ensure that the recorded trajectory is sufficiently long and consists of data points that are mutually uncorrelated (i.e. statistically independent) [25]. The probability distributions $P(x_i)$ and $p(x)$, defined by (2.24), are properly normalized

$$\int_{-\infty}^{\infty} p(x)dx = \sum_i P(x_i) = 1. \tag{2.25}$$

For an optically trapped particle that can be modeled as a harmonic oscillator, the probability distribution of the particle position is Gaussian,

$$p(x) = \frac{1}{\sqrt{2\pi\langle x^2\rangle}}\mathrm{e}^{-\frac{(\mathrm{x}-\mathrm{x}_0)^2}{2\langle \mathrm{x}^2\rangle}}, \tag{2.26}$$

where $\langle x^2\rangle$ is the position variance and x_0 is the mean position of the particle. Thus, if we fit $p(x)$ with the Gaussian distribution in Eq. (2.26), we can determine the variance and the mean value of the particle position. The main advantage of this method is that it is independent of the particle dynamics if the system is in thermodynamic equilibrium; the distribution of the particle position is not influenced by changes in the viscous damping rate, which in turn depends on the ambient pressure. Hence, using the position variance extracted from the histogram, it is possible to employ Eq. (2.23) to calculate the effective kinetic temperature T_{eff} of the particle in a harmonic potential more precisely than from integration of the position PSD Eq. (2.22).

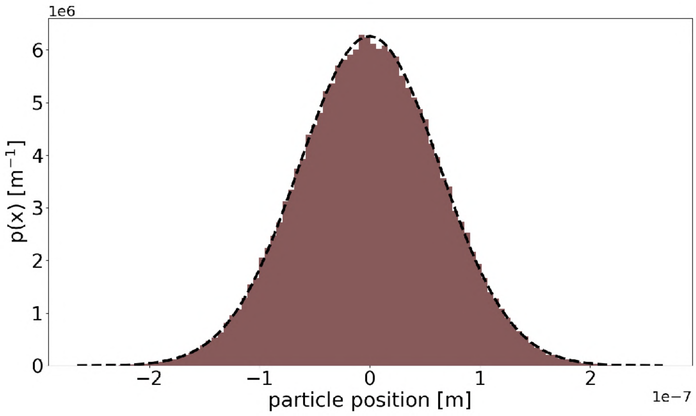

Figure 2.6: Characterization of particle spatial localization using probability density function of particle positions $p(x)$. The horizontal axis shows discrete locations x_i that define the boundaries of position bins with the width dx, and the vertical axis shows the frequency of the particle visits to the particular bin $\langle x_i; x_i + dx\rangle$. The solid brown bars indicate the actual histogram of an experimentally measured trajectory of the particle (for more graphs see Section 3.14), and the dashed black line then represents the theoretical fit of the histogram with the Gaussian probability distribution (2.26) with parameters $\langle x^2\rangle = 4.1 \cdot 10^{-15}$ m^2 and $x_0 = -2.1 \cdot 10^{-10}$ m.

2.3. Experimental parts common for all presented experiments

In this section, experimental parts and subsystems that were the same for all experiments with one or two optically levitated particles reported in this thesis will be described. These include the trapping and vacuum part of the set-up, a digital micromirror device (DMD), and detection of the levitating particle positions by a high-speed camera or by a quadrant photodiode.

2.3.1. Trapping part of the experimental set-up

The schema of the common trapping part of both experimental set-ups used in experiments reported in this thesis is shown in Fig. 2.7.

For optical trapping, a fiber laser system operating at the wavelength 1550 nm was used (Koheras ADJUSTIK seed laser + Koheras BOOSTIK high-power laser module; NKT Photonics). Collimated laser beam exiting from the fiber output equipped with a collimating lens passed through a system of a half-wave plate ($\lambda/2$) and a polarized beam splitter (PBS), with the help of which it was possible to change the total power entering the trapping set-up. The beam expander formed by lenses L_6 and L_7 doubled the diameter of the incident laser beam to cover the entire DMD area. Using the DMD,

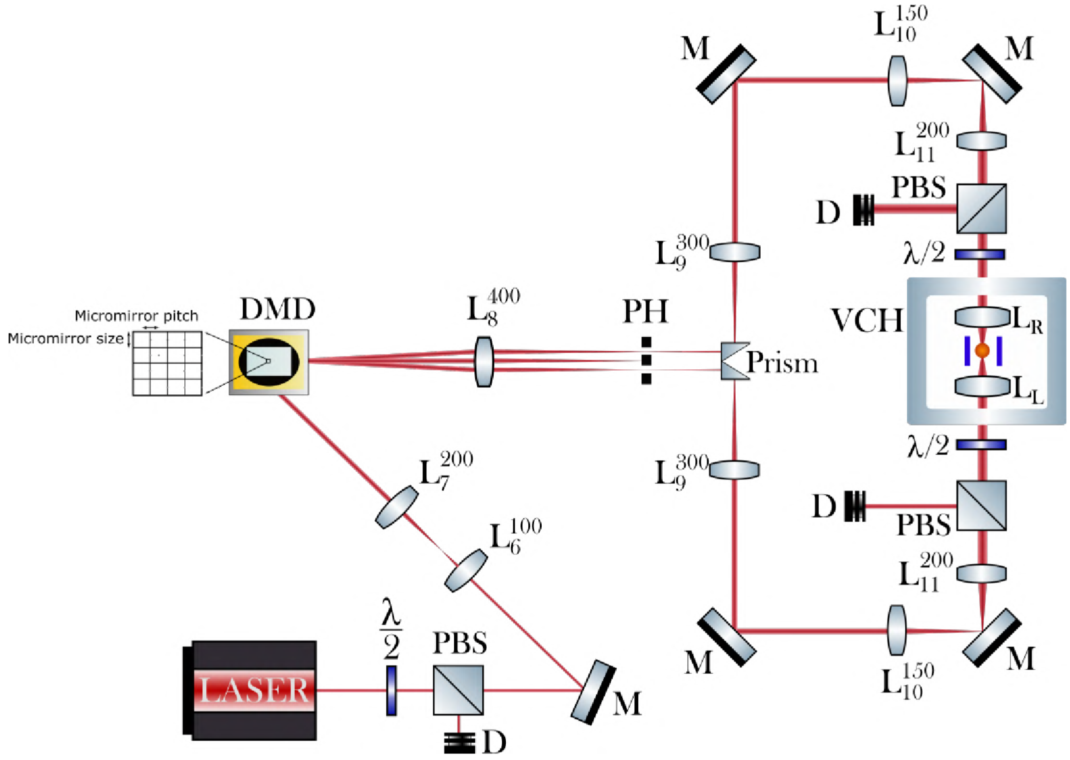

Figure 2.7: Schema of the common trapping part of both experimental set-ups used in experiments reported in this thesis. Explanation of used abbreviations: L – lens, M – mirror, D – beam dump, $\lambda/2$ – half-wave plate, VCH – vacuum chamber, PBS – polarized beam splitter, PH – pinhole. Superscripts in all lens symbols indicate the focal length of each lens in millimeters and subscripts characterize the order of lenses.

diffraction orders propagating in different directions were created and subsequently focused into distinct locations in the Fourier plane using the L_8 lens. Out of all diffraction orders, $\pm 1^{\mathrm{st}}$ orders were selected in the Fourier plane using a pinhole (PH) and subsequently, they were directed by a prism into two separate optical arms to form the two counter-propagating trapping beams in the vacuum chamber (VCH). Both arms had identical optical components to ensure beam uniformity and maximal elimination of possible wavefront distortions. Lenses L_9, L_{10} and L_{11} further adjusted the diameter of the collimated trapping beams to achieve the required size of the beam spots in the trapping region inside the vacuum chamber (VCH). With the help of mirrors located between the prism and the VCH, the two focused counter-propagating beams could be precisely overlapped in the trapping region. Furthermore, polarizations of the trapping beams were controlled by the half-wave plates placed in front of the VCH. Therefore, it was possible to create both a standing wave trap using identical polarization of the beams and a cross-polarized trap with perpendicular polarizations that prevented beam interference.

2.3.2. Digital micromirror device

A digital micromirror device (DMD) is a microelectromechanical device that consists of hundreds of thousands to millions of micrometric mirrors arranged on a rectangular grid. Each micromirror can be independently switched between two positions: the *off* position and the *on* position, which are most often characterized by tilt angles of ±12° relative to the surface normal. If the mirror is in the *on* position, it contributes to the reflected light that reaches the collection optical system, while the mirrors in the *off* position reflect the light towards an absorber (see Fig. 2.8(a) for illustration). Thus, DMD effectively acts as a spatially resolved binary modulator of the amplitude of the incident light beam [26, 27]. Considering the light propagation, an array of individually switchable micromirrors can be formally thought of as an addressable diffraction grating. By selectively switching the individual mirrors on and off, the amplitude and phase profiles of the diffracted light can be virtually arbitrarily shaped. There exist several strategies for achieving the desired modulation of the diffracted wavefront. Usually, the DMD serves to produce a hologram representing the target intensity distribution, which is subsequently reconstructed in the conjugated Fourier plane of the imaging optical system that collects the light diffracted from the DMD [26]. The appropriate binary amplitude hologram can be numerically calculated using the method of Lee, which exploits the interference between the target light beam and an off-axis reference plane wave to encode the required complex modulation of the diffracted wavefront using a binary amplitude-only mask [28].

The DMD consists of several layers located between the mirrors and the supporting substrate, which contain torsional hinges on which the mirrors can pivot, landing springs for slowing down the mirror motion during switching, electrodes that serve for the mirror actuation, and CMOS (Complementary Metal-Oxide-Semiconductor) memory cells that independently encode the desired “on/off”state of individual mirrors [26, 29]. The actual mirrors are typically fabricated from aluminum, which is lightweight and displays very good reflectivity over a broad spectral range. Due to their high maximal refresh rates of $\sim 32\,\mathrm{kHz}$ and very good spatial resolution (typical mirror size is $\sim 8-14\,\mu\mathrm{m}$), DMDs can be used very effectively to dynamically modulate the wavefront of light in applications including laser beam shaping, wavefront correction after passing through a scattering medium, phase mask optimization technique, quantum information encoding, and wavefront shaping in high-resolution optical microscopy [26, 29, 30].

In comparison to the modulation of the laser beam wavefront with phase-only spatial light modulators (SLM) based on oriented films of liquid crystals, DMD is potentially better in switching speed, provides a broader operating spectral range, handles higher powers and enables polarization modulation [26, 29]. Another big advantage of the DMD is the higher stability of the imposed holographic masks in contrast to SLMs. In particular, after sending the mask to the SLM, the liquid crystal film that serves as the actual phase modulator slowly relaxes to its original configuration. Thus, it is needed to periodically apply another voltage pulse which drives the liquid crystals back to the desired orientation. This effect is known as flicker noise and causes intensity fluctuation of the reflected laser beam, i.e. the optical trap, with a frequency of $200\,\mathrm{Hz}-6\,\mathrm{kHz}$. On the other hand, the DMD has also a disadvantage in the low diffraction efficiency, which is only $\sim 8\,\%$ of the incident light, compared to the SLM, which reaches $\sim 42\,\%$ [29]. If it is possible in the given application, this could be compensated by higher incident laser power.

As a result of the passage of the trapping beam (or beams) through the optical components or due to the non-planarity of the DMD, various aberrations can be introduced into the system and the beam wavefront can be distorted. However, the creation of a stable optical trap with a well-defined, symmetric force profile requires high regularity of the beam wavefront. Therefore, it is necessary to make corrections and calibrate the DMD in order to get rid of these defects and obtain the final intensity distribution as close as possible to the desired profile. The necessary correction can be done by introducing a suitable phase function $\varphi(x, y)$ (where x, y are the pixel coordinates in the DMD plane) to the computer-generated hologram that compensates for the net distortions introduced by the optical system. If the DMD area is divided into several smaller parts, the interference patterns between the waves diffracted from two different parts can be observed. In the case of aberrations present in the optical system, the maximum of the zeroth interference order will be shifted away from the axial direction. The observed fringe shift is then proportional to the required correction phase $\varphi(x, y)$. If the entire DMD is scanned in this way, a phase map can be obtained that can be superimposed upon the generated hologram and, thus, correct the system aberrations [27].

After calculating the hologram for the desired intensity distribution (see Fig. 2.8(c)) in the control computer and performing the necessary wavefront corrections (see Fig. 2.8(d)), the result is sent to the DMD. There, corresponding mirrors are turned on and off (see Figs. 2.8(e),(f)) so that the subsequent illumination of the DMD with a laser beam creates the desired intensity distribution in the Fourier plane of the optical system that collects the light diffracted from the DMD (see Figs. 2.8(g),(h)) [26]. If we want to create one dual-beam optical trap from two counter-propagating trapping beams, we can calculate the necessary phase mask from the argument of the following function $A_1 \mathrm{e}^{\mathrm{i}(x_1 X + y_1 Y + \mathrm{corrections}_1)}$, where A_1 is a wave amplitude, x_1, y_1 are the coordinates for the desired optical trap and X, Y are the spatial frequencies at the Fourier plane. The phase mask then encodes information about the mirror switching layout to the *off* and *on* position. In case we want to create two pairs of parallel counter-propagating trapping beams, we can sum the corresponding phase functions for both traps in the phase space. We express the function for the second trap analogically as for the case of one trap $A_2 \mathrm{e}^{\mathrm{i}(x_2 X + y_2 Y + \mathrm{corrections}_2)}$. After summing these two functions and calculating the argument of the sum we get the phase mask like in the case of one trap. Consequently, a diffraction image for zero and higher diffraction orders is created in the Fourier plane (shown by simulation in Fig. 2.8). Information about the creation of traps is then encoded in the plus-first diffraction order.

In our experiments, we used the DMD (model Vialux V-650LNIR) to create a dual-beam optical trap for the cold damping (CD) experiments and two independent dual-beam traps for the optical binding experiments (see Fig. 2.8(b) for illustration). The DMD had a size of the pixel pitch of 10.8 µm, resolution of 1280×800 px and was able to switch between two positions with a frequency of 10.5 kHz. The overall switching time of the DMD was 93 µs, out of which 10.2 µs corresponded to the dead time between changing two subsequent holograms, during which the light wavefront was not fully defined. We blocked the 0^{th} diffraction order and allowed only the $+1^{\mathrm{st}}$ diffraction order to pass to create two or four independent beams that were then sent against each other (for details, see the pictures of the experimental set-up for the CD experiments in Fig. 3.7 and for the optical binding experiments in Fig. 4.5). In our experiments, we had full control over the parameters of the traps including the optical power in one or both traps and the separation distance and phase difference between the two simultaneously created traps. The computer code for calculating the holograms that had to be sent to the DMD to get counter-propagating beams with suppressed aberration was created in LabView by my colleague Ing. Petr Jákl, Ph.D. at the Institute of Scientific Instruments of the Czech Academy of Sciences.

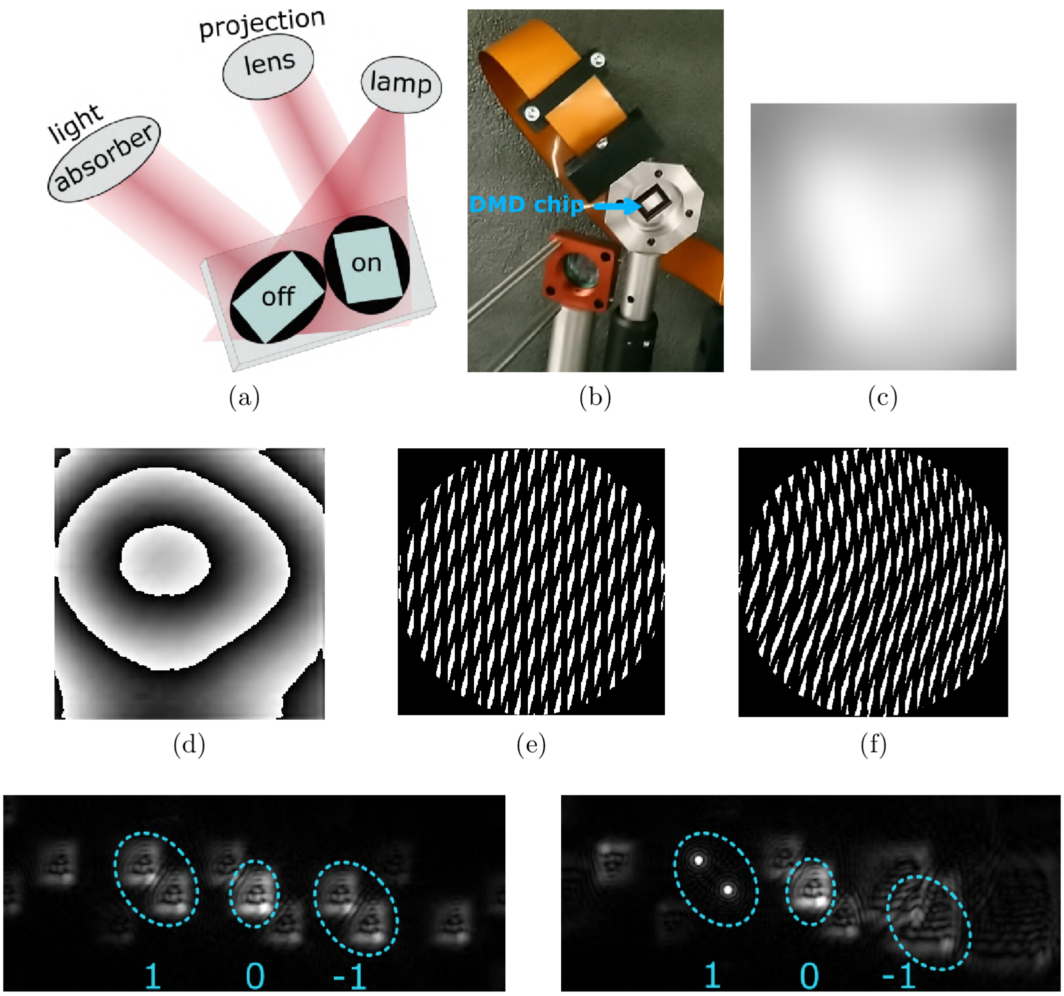

(a) (b) (c)

(d) (e) (f)

(g) (h)

Figure 2.8: (a) Graphical illustration of the incidence of light on two mirrors on the DMD chip with different positions (*on* and *off*). The mirror in the *on* position reflects light into the projection lens. This light subsequently enters the imaging system. However, the mirror in the *off* position reflects the light into the light absorberand, thus, this light does not contribute to the formation of the image. (b) Actual DMD used in our experimental set-up. (c) Simulation of the field intensity profile. In the lightest spots there is the biggest intensity. (d) Simulation of the phase mask (from $-\pi$ (white part) to $+\pi$ (black part)) for correcting optical aberrations introduced by the DMD chip and by the imaging optical system. (e) Hologram on the DMD for the creation of dual-beam optical trap without aberration correction. The black part corresponds to the mirrors in *off* position and white for the mirrors in *on* position. (f) Hologram on the DMD for the creation of dual-beam optical trap with aberration correction. Compared to the hologram in (e), it can now be seen that the image is slightly convex and the mirrors are no longer arranged in strictly parallel rows. (g) Simulated image in the Fourier plane behind the first lens without applying the aberration corrections with the 0 and ±1 order marked. It can be seen that all the orders are blurred. (h) Simulated image in the Fourier plane behind the first lens using the aberration corrections, with the 0 and ±1 order marked. It can be seen that the +1 diffraction order is now clearly focused, it is divided into two points that will subsequently form a dual-beam trap. The image is rotated by 45^o, however, in the real setup (see (b)) the DMD itself is rotated by 45^o so that the points are next to each other in reality.

2.3.3. Detection of the particle position by high-speed camera

The optical path for the position detection of optically levitated NPs by a high-speed CMOS camera (Phantom V611; Vision Research), identical for all types of experiments presented in this thesis, is schematically shown in Fig. 2.9.

A green laser beam with a wavelength of 532 nm (second harmonic of Nd:YAG laser Prometheus; Coherent) was used to illuminate the levitated NPs. The slightly divergent laser beam was first collimated by lens L_1 and subsequently passed through a $\lambda/2$ plate and a PBS. Using this pair of optical components, it was possible to regulate the amount of illumination power that entered the set-up. The diameter of the beam was then enlarged via a telescope formed by lenses L_2 and L_3 to fill the back aperture of the coupler lens C_1 that focused the beam into the core of a single-mode optical fiber. The beam emitted from the fiber output was collimated again via the collimator lens C_2 and subsequently focused onto the trapping region in the vacuum chamber by lens L_4. The green light scattered by the optically levitated NPs was collected by an infinity-corrected objective lens L_{ob} (Mitutuo, magnification: 80×, NA $= 0.5$) and then projected on the chip of the high-speed camera with a tube lens L_5.

In experiments with a single levitated particle, the camera usually served for monitoring the particle confinement in the trap or for correct adjustment of the set-up. In the case of two simultaneously levitated particles, we also used the camera for the calibration of particle trajectories recorded with a quadrant photodiode (more information in Sections 2.3.4 and 2.6.2). During experiments with two particles, the frame rate was set to 200 kHz and typically, we recorded at least 100 000 frames to obtain a sufficiently long trajectory for analysis. From the video record, we were able to determine the particle motion along the x-axis (perpendicular to the polarization direction) and z-axis (beam propagation direction). Tracking of the particle position in individual recorded frames was based on evaluating the symmetries in the particle image (see Section 4.2.5 for more information).

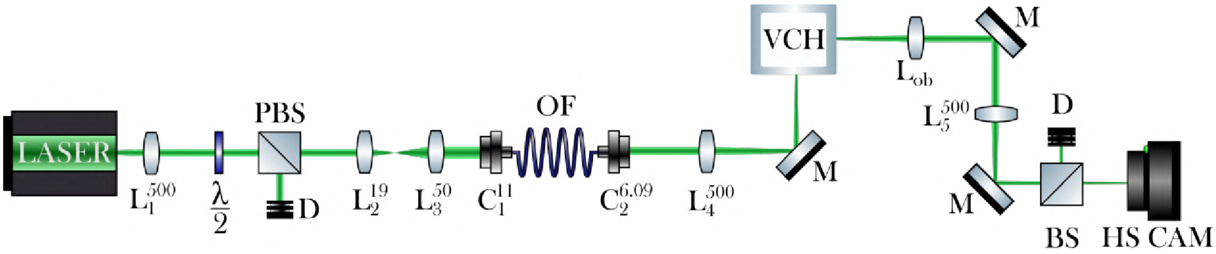

Figure 2.9: Schema of the detection of the particle position by a high-speed CMOS camera. Explanation of used abbreviations: C – coupler/collimator lens, BS – beam splitter, HS CAM – high-speed camera, OF – optical fiber and D, PBS and $\lambda/2$ have the same meaning as in Fig. 2.7. Superscripts in all lens symbols indicate the focal length of each lens in millimeters and subscripts characterize the order of lenses.

2.3.4. Principles of detection of the particle position by quadrant photodiode

The second method used to detect the position of levitated NPs was based on monitoring the intensity distribution in the interference pattern between the trapping light and the light scattered by the NP using a quadrant photodiode (QPD).

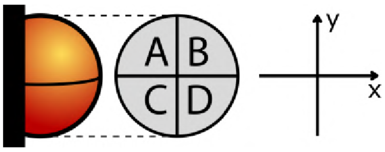

Figure 2.10: Schema of QPD with four photodiodes arranged in quadrants.

As shown in Fig. 2.10, the QPD is divided into four parts acting as independent photodiodes that can be individually read. Using the QPD, the NP position signals can be derived from the sums and differences of signals Q_A, Q_B, Q_C, Q_D registered by the individual quadrants. In particular, a displacement of the NP along the x-axis can be determined using the formula $x = (Q_B + Q_D) - (Q_A + Q_C)$, a displacement along the y-axis is given by $y = (Q_A + Q_B) - (Q_C + Q_D)$, and z-displacements are proportional to the total intensity incident on all four quadrants, $z = Q_A + Q_B + Q_B + Q_D$. If the levitated NP is located on the axis of the trapping beam, the interference pattern between the scattered and trapping light has a full rotational symmetry and, thus, all four QPD segments detect the same incident intensity. Consequently, the x and y position signals are both zero. However, if the NP is displaced along one of the directions x or y, the symmetry of the interference pattern is broken and non-zero signals are recorded.

The main advantages of QPD-based position detection are the speed of detection (sampling rates in the MHz range can be routinely achieved) and the absence of a data post-processing step, which in principle allows real-time monitoring of the NP's position. On the other hand, the position signals from the QPD are measured in arbitrary units and proper calibration to the SI units is required before quantitative analysis of the recorded data. This calibration will be described in more detail in Section 2.6.1.

2.3.5. Vacuum part of the experimental set-up

Vacuum part of the experimental set-up enabled reaching lower pressures of the ambient atmosphere surrounding the trapped NP. As the damping coefficient γ in Stoke's law (Eq. (2.10)) decreases with decreasing ambient pressure, reducing the pressure brings the particle motion into the underdamped regime, where the regular oscillations of the trapped particle are clearly visible.

The schema of the vacuum section of the experimental set-up is shown in Fig. 2.11. The most important parts of the vacuum assembly were the vacuum pumps: the *diaphragm pump*, which served as the pre-pumping stage for the *turbo-molecular pump*. Both pumps were integrated into a single commercially available device (HiCube; Pfeiffer). The approximate value of the pressure inside the vacuum chamber was measured using a Penning gauge. The pumping speed could be regulated using two valves: a *needle valve* for gentler manipulation (mostly used at the beginning of pumping, so that there was no sudden pressure change in the vacuum chamber that would kick the trapped particle out of the trap) and a *plate valve* for larger pressure changes (mostly used after the initial pre-pumping through the needle valve to reach lower pressures more quickly). Another part of the vacuum assembly was the *bellows*, which dampened the mechanical vibrations transmitted from the pumps to the vacuum chamber and optical table and, consequently, also to the trapped particle.

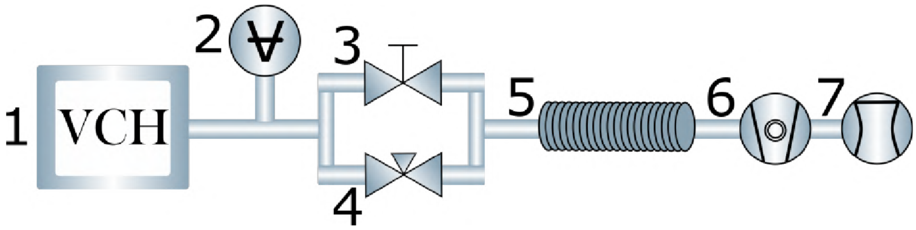

Figure 2.11: Schema of the vacuum part of the experimental set-up. 1 – vacuum chamber, 2 – Penning gauge with a cold cathode, 3 – manual needle valve, 4 – manual plate valve, 5 – bellows, 6 – turbo molecular vacuum pump, 7 – diaphragm vacuum pump.

2.4. Preparation of particles for optical levitation experiments

Insertion of NPs into optical traps was done at atmospheric pressure using a nebulizer filled with a suspension of SiO_2 (silica) NPs in a mixture of water and filtered ethanol. Preparation of the suspension and the actual method of particle loading will be described in more detail in Sections 2.4.1 and 2.4.2.

2.4.1. Suspension preparation

Experiments with a single levitated particle:

The suspension of NPs consisted of 1.5 ml of ethanol filtered through a membrane filter with 0.2 µm pores and 10 µl of an aqueous solution of silica NPs with a diameter of 600 nm (Bangs Laboratories, Inc.; USA; solids = 10.2 % in the stock bottle). The mixture was first shaken in Vortex Ika Genius 3 device to homogenize the suspension. Subsequently, Eppendorf test tube with the suspension was placed for approximately 15 minutes into an ultrasonic bath device (Elmasonic S 15; Elma) to break the clusters of NPs.

Experiments with two levitated, optically bound particles:

The suspension of NPs consisted of 1.5 ml of ethanol filtered through a membrane filter with 0.2 µm pores and 40 µl of an aqueous solution of silica NPs with a diameter of 611 nm (microParticles GmbH; Germany, solids = 5 % in the stock bottle). The mixture was first shaken in Vortex Ika Genius 3 device to homogenize the suspension. Subsequently, the Eppendorf test tube with the suspension was placed for approximately 1 hour into an ultrasonic bath device (Elmasonic S 15; Elma) to break the clusters of NPs.

2.4.2. Nebulizer

Nebulizer is a medical device that helps asthmatic people with breathing difficulties; it turns liquid medicines into aerosols that can be easily inhaled. In the optical levitation community, nebulizers serve as one of the most common tools for particle loading into optical traps. The schema of an ultrasonic nebulizer is shown in Fig. 2.12. The solution to be turned into aerosol is contained in a small vessel with a hole in one of the side walls, covered by a membrane to which a piezoelectric crystal is connected. After bringing AC voltage to the piezoelectric crystal, the crystal periodically expands and contracts and the attached membrane starts vibrating. The solution then passes through the vibrating membrane that creates aerosol droplets. A fraction of these droplets contains an NP/multiple NPs inside. Upon capturing a droplet with a NP inside in an optical trap and evaporation of the droplet liquid, one obtains an optical trap loaded with the NP. In general, NPs loaded by this method will also be charged by triboelectric effects which occur when the solution passes through the membrane.

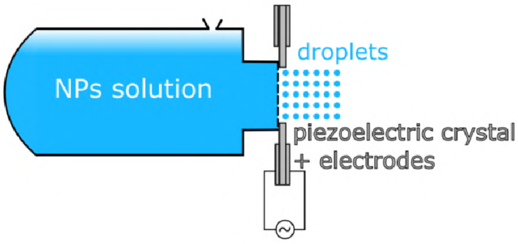

Figure 2.12: Schema of an ultrasonic nebulizer with a vibrating membrane (indicated by the dashed line in the right side wall of the nebulizer body). Blue filling represents the working solution with NPs inside the nebulizer body, gray rectangles represent a piezoelectric crystal with attached electrodes to which alternating voltage is applied. Periodic expansions/contractions of the electrically driven crystal then excite the vibrations of the membrane. Blue circles on the right side of the membrane symbolize the formed aerosol droplets.

In our experiments, we used a modified nebulizer shown in Fig. 2.13. In order to have better control over loading NPs into the optical trap, we printed an extension nozzle using a 3D printer and attached it to the nebulizer outlet. This flow-focusing nozzle helped us to direct the NPs more precisely to the trap, instead of spraying the droplets to the whole chamber. Similar to the standard procedure, we placed the working solution inside the nebulizer and created the droplets that were subsequently directed to the nozzle by a gentle stream of air produced by a syringe connected to the nozzle via flexible plastic tubing (see Fig. 2.13 for illustration).

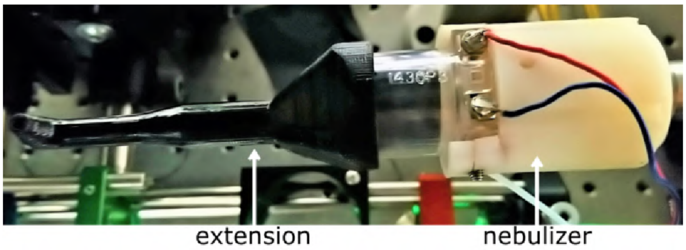

Figure 2.13: Modified version of the nebulizer (white part) with attached extension nozzle for controlled loading of NPs into the optical trap (black part). The red and blue cables supply voltage to the piezoelectric crystal with the help of which droplets of working solution are produced at a vibrating membrane. To push the droplets containing the NPs into the optical trap, the airflow generated by a syringe is fed into the nozzle through a piece of translucent flexible tubing.

2.5. Alignment of the experimental set-up for stable optical trapping

In this section, the experimental alignment of the whole optical trapping set-up will be explained, followed by a detailed description of our approach to stable confinement of one and two particles in dual-beam optical traps.

2.5.1. Alignment of dual-beam optical trap

If we wanted to confine a particle in a dual-beam optical trap, we had to correctly align the optical paths for the two trapping beams. In particular, it was necessary to perfectly overlap the foci of both trapping beams in the transverse plane (using translational and angular adjustments of the beams along the x and y axes), correctly set the polarization states of the beams (using half-wave plates), and adjust the distance of the two trapping lenses in the vacuum chamber along the z-axis. If the experimental setup was not correctly aligned, it would not be possible to trap silica particles because we would not have sufficient gradient force for stable confinement. Therefore, for the initial alignment, we only used isopropyl alcohol (IPA) droplets (for the drops themselves, IPA was better for trapping than ethanol), which were lighter and smaller than the particles. In addition, we could be sure that they have a precisely spherical shape and, thus, the alignment was not negatively affected by the shape asymmetry of the trapped object.

Coarse adjustment of the two beam foci was possible using a camera that detected the position of the foci on the mirror behind the vacuum chamber (see Fig. 2.7). For a more precise alignment, it was already necessary to trap a droplet. Using the DMD, we first turned on only one trapping beam, creating an optical tweezers trap into which we trapped a droplet. Using the camera, we marked the position of the trapped droplet in the field of view at atmospheric pressure and also at a lower pressure (approximately 60 mbar). Subsequently, we switched the confinement to the other trapping beam (second optical tweezers trap) and observed the behavior of the trapped droplet. The droplet either jumped to the stable trapping position in the second optical trap or we lost it and had to trap it again. In either case, we marked the position of the second optical trap in the field of view and compared it with the position of the first trap. In order to achieve the correct overlap of both traps, we attempted to move the droplet to the same trapping location in the field of view for both trapping beams, either with the mirrors (x and y axis) or with the trapping lens that was placed on a precision positioning stage (z axis).

After adjusting the overlap of the beams, we turned on both beams simultaneously to form a SW trap and tried rotating the polarization to see if the droplet could withstand this adjustment at a lower pressure. If the droplet did not remain confined, we needed to continue aligning the trapping beams more precisely, mostly along the z-axis. If the droplet remained confined in the trap, we could try to trap a silica particle. Further adjustments of the trapping beams with a confined silica particle were carried out only in the dual-beam arrangement (SW trap), because the silica particles used in our experiments were too large to be trapped in the single-beam optical tweezers.

The detailed procedure for stable trapping and optical levitation is described in Section 2.5.2 for a single particle and in Section 2.5.3 for two particles.

2.5.2. Stable trapping of a single particle

In the beginning of the experiment, we loaded the particles into the dual-beam optical trap formed in the vacuum chamber using the modified nebulizer with an attachment nozzle (see Fig. 2.13). As the attachment nozzle covered a part of the green illumination beam used for imaging the trapped particles on the camera (see Section 2.3.3 for details), it was not possible to observe the capture of the particle by direct imaging. Instead, the capture was visualized indirectly, using the signal from the QPD and a script in the LabView control program, which converted the recorded QPD voltages into the PSD of the particle position in real-time. Thus, an immediate response to a particle entering the trap could be observed. Specifically, the almost flat PSD of the background signal would change to a resonant peak if a particle was trapped. Depending on the intensity of the PSD peak, it could also be verified whether the trapped object was really the desired silica particle or just a droplet composed of ethanol or water. After the nebulizer was retracted from the vacuum chamber, the trapped object could be directly visualized on the camera. An example of an individual trapped particle could be seen in Fig. 2.14(a); in the case of trapping a liquid droplet, the intensity of the image was much lower and it was very difficult to distinguish the image of the object from the background. Sometimes, it was also possible to trap a cluster of multiple particles, which was an unwanted object that usually appeared as a slightly asymmetrical sphere on the camera. It was more difficult to distinguish between trapped clusters and individual particles at the atmospheric pressure where the PSD peak was wider than at lower pressures.

After verifying the capture of the particle in the PSD calculated from the QPD trajectories and in the camera image, we wanted to ensure that the particle was confined in the most stable axial equilibrium position. Sometimes, the particle could be trapped in a less stable position and could jump between two adjacent standing wave traps, which complicated the experiments with particle cooling. For this step, we rotated one of the half-wave plates in front of the vacuum chamber to switch from the confinement in the standing wave with multiple equilibrium positions to CP dual-beam trapping, with only one equilibrium position. This forced the particle to jump to the most stable position located symmetrically with respect to the focal planes of the two trapping beams. We then returned the beam polarization to the original configuration in which the standing wave was created. If the trapped particle began to oscillate a lot while slowly rotating the polarization, it was possible to prevent it from escaping the trap by changing the beam's polarization. By reducing the beam waist radius in the trapping region, we could achieve greater lateral stiffness of the trap and the particle would be more stably localized on the beam axis. Subsequently, we could gradually align the beams and more precisely overlap their focal spots until the particle could again be stably confined with a wider beam waist radius. When transitioning to the CP trap arrangement, the amount of light that was reflected from the PBS to the position detection branch increases. Therefore, before rotating the polarization of the trapping beam, it was necessary to protect the QPD with a neutral density filter or a beam dump in order not to damage it. After moving the particle to the desired axial trapping location, the filter/beam dump could be removed again.

When it was verified that the particle could be stably trapped with the given configuration of the trapping beams, we retracted the nebulizer, closed the vacuum chamber, and started pumping. Initially, only the diaphragm pump was used until reaching the pressure of approximately 10 mbar. Subsequently, we started the turbo pump as well and went down to the pressure required for the experiments. The transverse profile of the optical trap created in the focal region by focusing a linearly polarized trapping beam was generally slightly elliptical. Consequently, the trapping stiffness was different along the two characteristic directions oriented along the main axes of the ellipse. At lower ambient pressures, it was necessary to minimize the cross-talk between these trapping directions by means of a more precise tuning of the overlap of the trapping beams (changing the position of the mirror in the optical path for one of the beams and the position of the lens inside the vacuum chamber) and by rotating the QPD so that the main axes of the elliptical trap coincided with the QPD axes. The ideal QPD setting could be recognized by observing two isolated spectral peaks at slightly different frequencies in the PSDs calculated from the QPD trajectories along the x- and y-axis. Sometimes, however, even with the best possible settings, the cross-talk from one axis to another could not be completely eliminated.

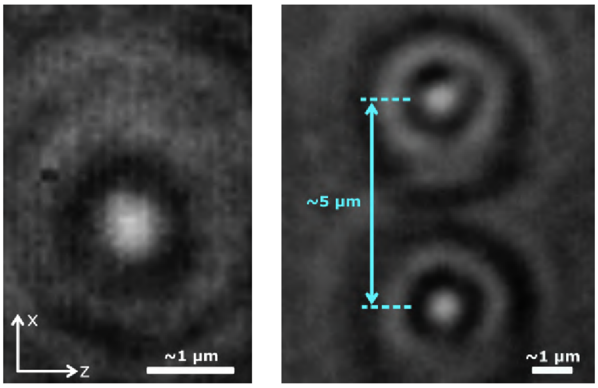

(a) (b)

Figure 2.14: Images of stably trapped silica nanoparticles. (a) One silica nanoparticle with a diameter of 600 nm confined in a single SW trap. (b) Two silica nanoparticles with diameters of 611 nm confined in two parallel SW traps. The trapping beams propagated along the z-axis, oriented horizontally in the images.

2.5.3. Stable trapping of two particles

In the case of simultaneous trapping and cooling of two particles in optical binding experiments, there is a greater risk that one of the particles will be lost, or that a collision will occur and both particles will join into a cluster. Therefore, the trapping procedure described in Section 2.5.2 was slightly modified. As before, we loaded the particles into two independent optical traps with a nebulizer and verified the capture of two particles using the QPD traces and the camera. However, we now carried out the polarization rotation required for the transition between the SW and CP configurations and for the transfer of both particles to the most stable axial trapping location at a lower pressure in the range of 100–50 mbar. In the optical binding experiments, we needed the two particles to be located in exactly the same interference fringe in the two dual-beam traps (aligned along the vertical direction in the camera image shown in Fig. 2.14(b)). The main reason for carrying out the adjustment of the axial position of the two particles at a lower pressure was that the set-up was more stable and better aligned at lower pressures.

After stable trapping of two particles and successful evacuation of the vacuum chamber to a lower pressure, we fine-tuned the overlap of the foci of both beams, the detection path, and the QPD settings. Subsequently, a calibration measurement was performed to convert the positions of the particles recorded in arbitrary units with the QPDs to the SI units. This was achieved by simultaneously recording the position traces of both particles with two independent QPDs and with the camera (see Section 2.6.2 for details).

2.6. Calibration of position acquired by quadrant photodiode

In this section, algorithms for data calibration and processing for the cases of one and two optically levitated nanoparticles will be described. The scripts for the analysis of experimental data obtained with one particle were written in Python programming language and the script for the analysis of experimental data obtained with two particles was written in Julia programming language. I wrote the script in Python by myself and the script in Julia was prepared by my colleague Mgr. Oto Brzobohatý, Ph.D. at the Institute of Scientific Instruments of the Czech Academy of Sciences. In the case of two particles, I only graphically processed the already evaluated data from Julia in Python.

2.6.1. One-particle experiments

The output position signals obtained from the QPD were in the units of volts and therefore proper calibration procedure [31, 32] must be used to convert these signals to the basic SI units of length, i.e., meters.

First, we determined the spectrum P_x of the uncalibrated position of the particle in the units of V^2/Hz from the data recorded without turning on the feedback cooling. In general, the position PSD calculated from experimental trajectories is affected by the measurement noise that manifests itself as a constant noise floor P_x^∞ at high frequencies. To assess the level of this noise floor, we analyzed P_x at frequencies

$$f_{\mathrm{noise}} \geq 0.75 f_{\mathrm{Nyq}}, \tag{2.27}$$

where f_{Nyq} is the Nyquist frequency that is equal to half of the sampling frequency of the data. Since our sampling rate was sufficiently higher than the typical oscillation eigenfrequency of the levitated particle, we could safely assume that the contribution to P_x at frequencies f_{noise} resulted entirely from the detection noise. Thus, the noise floor P_x^∞ could be determined by averaging the values of P_x over the frequency range f_{noise}. After that, we calculated the PSD of the uncalibrated velocity of the particle, from which we determined the final calibration constant. The velocity PSD was determined from the position PSD as [32]

$$P_v = (P_x - P_x^\infty)\omega^2. \tag{2.28}$$

The main advantage of using the velocity PSD P_v for the calibration is the fact that the equipartition theorem for the kinetic energy holds even in the case of particles optically levitated in anharmonic trapping potentials, for which the mean potential energy does not have a simple relationship to the value of $k_\mathrm{B}T$. Specifically, in thermodynamic equilibrium, the mean kinetic energy follows

$$\frac{1}{2}k_\mathrm{B}T = \frac{1}{2}m\langle v^2\rangle, \tag{2.29}$$

where T is the ambient temperature, m is the mass of the particle and $\langle v^2\rangle$ is the variance of the particle velocity that can be determined by numerical integration of P_v: $\langle v^2\rangle = 1/\pi \int_0^\infty P_v d\omega$. In addition, the multiplication of the position spectrum $(P_x - P_x^\infty)$ by ω^2 contributes to the elimination of the effects of low-frequency mechanical noises and drifts.

Using (2.29) together with the definition of $\langle v^2\rangle$, the calibration constant $c_{\mathrm{V}\to\mathrm{m}}$ for conversion of measured trajectories from volts to meters can be calculated as

$$c_{\mathrm{V}\to\mathrm{m}} = \sqrt{\frac{\pi k_\mathrm{B}T}{m\int_0^\infty P_v d\omega}}. \tag{2.30}$$

The final calibration constants for experiments with one particle were $c_{x,V\to m} = 8.8 \cdot 10^{-7}\,\mathrm{m/V}$ and $c_{y,V\to m} = 9.5 \cdot 10^{-7}\,\mathrm{m/V}$ for x- and y-axis in 1D CD experiments, $c_{x,V\to m} = 1.4 \cdot 10^{-6}\,\mathrm{m/V}$ and $c_{y,V\to m} = 2.1 \cdot 10^{-6}\,\mathrm{m/V}$ for x- and y-axis for cooling only x-axis and $c_{x,V\to m} = 1.4 \cdot 10^{-6}\,\mathrm{m/V}$ and $c_{y,V\to m} = 2.1 \cdot 10^{-6}\,\mathrm{m/V}$ for x- and y-axis for cooling both axes in 2D CD experiments.

2.6.2. Two-particles experiments

In the case of two-particle experiments, the calibration was performed by simultaneous measurement of the particles' position on the camera and on two independent QPDs (one for each particle) without applied feedback cooling. To use the particle trajectories obtained from the camera for QPD calibration, the camera (Phantom V611; Vision Research) first had to be calibrated from pixels to meters. This was done with the help of a calibration grid with precisely given line spacing (in our case 1 µm). The camera calibration constant determines what distance in the object plane of the imaging system is projected onto a single pixel of the camera chip after passing through the imaging system. During the calibration, the grid was placed in the object plane of the system and displayed on the camera. The camera manufacturer states the size of 1 pixel as 20 µm. From the observed number of camera pixels per known line separation of the calibration grid, the final calibration constant was determined to be 148 nm/pixel.

The QPD calibration itself then consisted of processing the recorded images from the camera and determining the displacement of the particles in meters. Since the images on the camera were recorded at the same times as the QPD position signals, both trajectories could be directly compared to each other. More precisely, high-pass filtering was applied to the trajectories obtained from the camera to eliminate the effect of low-frequency vibrations of the camera and subsequently, the variance of the particle position from the camera trajectory was compared to the variance of the particle position observed on the QPD. From the comparison, the resulting calibration constant was calculated, which determined the conversion of the QPD signal measured in volts into the SI units of meters. The final calibration constants for both modes were $c_{\Sigma,V\to m} = 1.9 \cdot 10^{-6}\,\mathrm{m/V}$ for CoM mode and $c_{\Delta,V\to m} = 2.0 \cdot 10^{-6}\,\mathrm{m/V}$ for Br mode.

2.7. Real experimental set-up

Figures. 2.15 and 2.16 show the real appearance of the used experimental set-up which is discussed and described in the thesis. I participated in the commissioning and running of this experimental apparatus and made measurements on it.

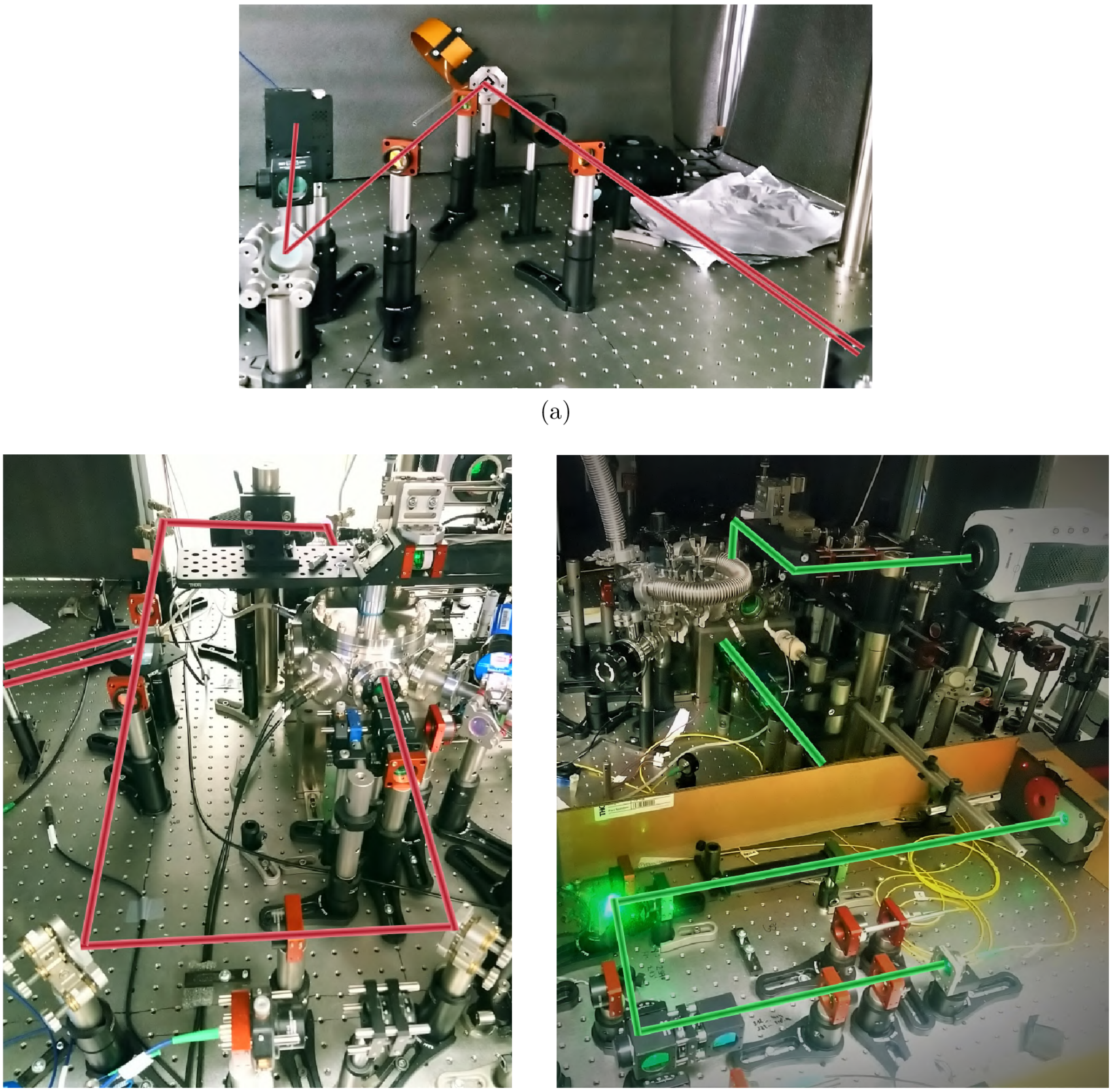

(a)

(b)

(c)

Figure 2.15: Real views of the experimental set-up. (a) The trapping laser beam (red lines) diffracts on the DMD and passes through two pinholes to form two counter-propagating beams. (b) Two trapping beams form the dual beam trap in the vacuum chamber. (c) The detection part with the high-speed camera (the schema is shown in Fig. 2.9). Green lines show the direction of the laser beam from the laser to the camera via the detection optics.

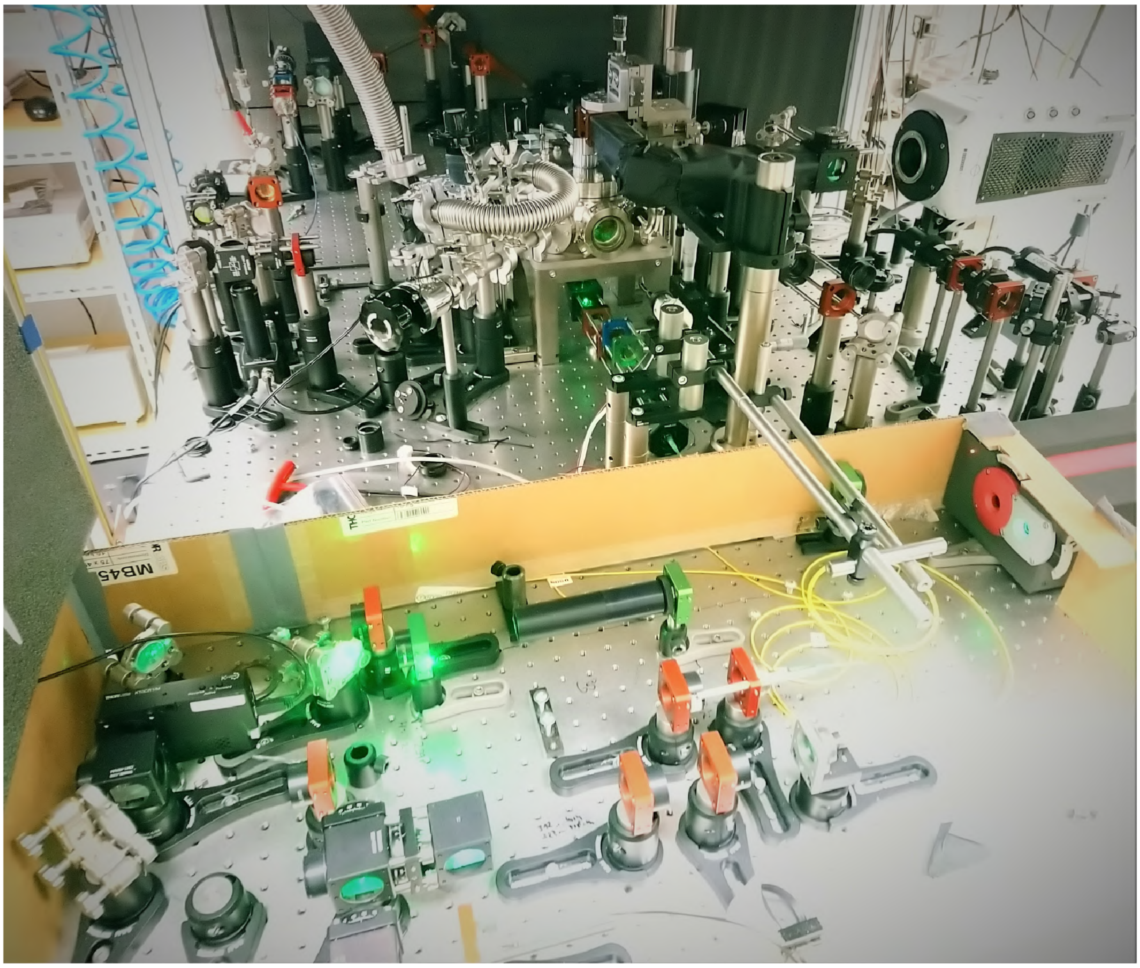

Figure 2.16: A real view of the entire experimental set-up used for experiments with two particles (schema in Figs. 2.7 and 4.5).

3. Cooling of thermal motion of optically levitated particle

3.1. Parametric feedback cooling

To date, the most successful cooling method in the field of levitated optomechanics has been parametric feedback cooling in a single-beam optical trap. This cooling technique is based on the implementation of a feedback loop that modulates the stiffness of the trapping potential well at twice the particle oscillation frequency ω_{0x} with an appropriate phase shift [12, 33]. The stiffness modulation principle is shown in Fig. 3.1. When the particle moves away from the trap center, the feedback loop increases the stiffness of the potential well and, thus, makes it more difficult for the particle to move. However, when the particle displaced from the trap center moves towards it, the potential well stiffness is reduced to decrease the effective pulling force. The average energy $\bar{E}$ of the particle oscillating in a harmonic potential can be characterized in terms of the mean occupation number $\bar{n}$ of oscillation quanta (phonons) as $\bar{n} = \frac{\bar{E}}{\hbar\omega_{0x}}$, where $\hbar$ is the reduced Planck constant [34]. Parametric feedback cooling allows reaching mean occupation numbers of the center-of-mass motion below 100 phonons.

The principal advantage of parametric feedback cooling is in the simplicity of implementation in a real experimental set-up – a modulator of the trapping laser power is enough. In the case of simultaneous cooling of multiple axes, it is only necessary to alter the control program, no physical change is needed. The main drawback of this method is its lower cooling efficiency compared to cold damping and cavity cooling techniques [33, 35].

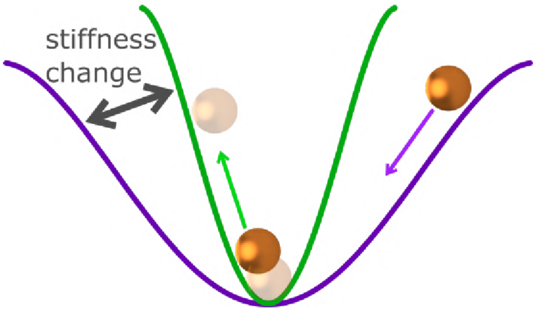

Figure 3.1: Basic principle of parametric feedback cooling. With the implementation of a feedback loop, the trapping potential well can be shaped according to the position and velocity of the trapped particle. Solid lines indicate different profiles of the trapping potential: the green trapping potential with a higher stiffness acts on the particle moving away from the trap center, whereas the violet trapping potential with a lower stiffness acts on the particle that returns back to the trap center. The arrows of corresponding colors show the respective directions of the particle motion.

3.2. Cavity cooling

Cavity cooling techniques use optical resonators to cool the thermal motion of an optically trapped particle without the need to actively measure the particle position. These techniques can be implemented in two alternative ways.

The first method illustrated in Fig. 3.2(a) is older and uses two independent lasers - one for trapping the particle inside a resonator (green vertical beam) and another one as a pump laser for the particle cooling (red horizontal beam). If there was no trapped particle inside the resonator, optical transmission along the horizontal direction would be sharply localized near the resonant frequency of the cavity (blue dashed line in Fig. 3.2(b)). However, if we use a second laser with a different frequency to trap a particle behaving as a harmonic oscillator, the oscillations of the particle will modulate the frequency of the pump laser transmitted through the cavity. Consequently, two sidebands will be created with frequencies of $\omega_\mathrm{L} \pm \omega_\mathrm{m}$, where ω_L is the frequency of the pump laser photons and ω_m is the frequency of mechanical oscillations (phonons) of the trapped particle. The red-shifted (Stokes) sideband with the frequency of $(\omega_\mathrm{L} - \omega_\mathrm{m})$ is created by transferring the energy of laser (photons) to the phonons of the thermal oscillation of the particle; this process heats the particle. The blue-shifted (anti-Stokes) sideband with the frequency of $(\omega_\mathrm{L} + \omega_\mathrm{m})$ is then formed by the transfer of phonon energy to the photons, which results in the extinction of the phonons and, thus, cooling of the particle motion. If we slightly detune the resonant frequency of the cavity and set it equal to one of the sidebands, the corresponding process will be amplified and, thus, we can either heat or cool the thermal motion of the particle. In the case of cooling, it is necessary to have the pump laser red-detuned with respect to the cavity resonance (smaller frequency than before) so that the resonance coincides with the anti-Stokes sideband at $(\omega_\mathrm{L} + \omega_\mathrm{m})$ (Fig. 3.2(b)) [36, 37, 38].

The second method – cavity cooling by coherent scattering – uses just one laser for both trapping and cooling of the particle; there is no separate pump laser (Fig. 3.2(c)). The trapped particle scatters light that is coherent with the trapping laser into an empty cavity, which is then driven by this scattered light. Since the trapped particle harmonically oscillates, it modulates the frequency of the scattered light that is reflected from the mirrors of the cavity. Similar to the previous configuration, both Stokes and anti-Stokes scattered photons are generated. If we detune the cavity to be in resonance with the anti-Stokes scattered photons, we will increase the probability of this particular scattering process which channels energy away from the particle, thereby cooling its thermal motion. In comparison with the first method, a photon can enter the cavity only due to the scattering of the trapping light from the particle, which itself takes away the particle energy. It is also sufficient to use a smaller beam power in the cavity to achieve efficient cooling [39].

The principal advantages of cavity cooling techniques are the high efficiency of cooling, which translates into very low effective kinetic temperatures of the trapped particle that can be achieved, and autonomous operation that does not require the measurement of the particle position. The main limitation is the necessity of implementing the cavity in the experimental setup, which can be space-demanding and increases the complexity of the experimental setup. Correct locking of the scattered light to the cavity frequency for cooling to occur is also more challenging than other methods. In addition, cavity cooling is very susceptible to various disturbances from the environment that can easily interrupt the cavity lock.

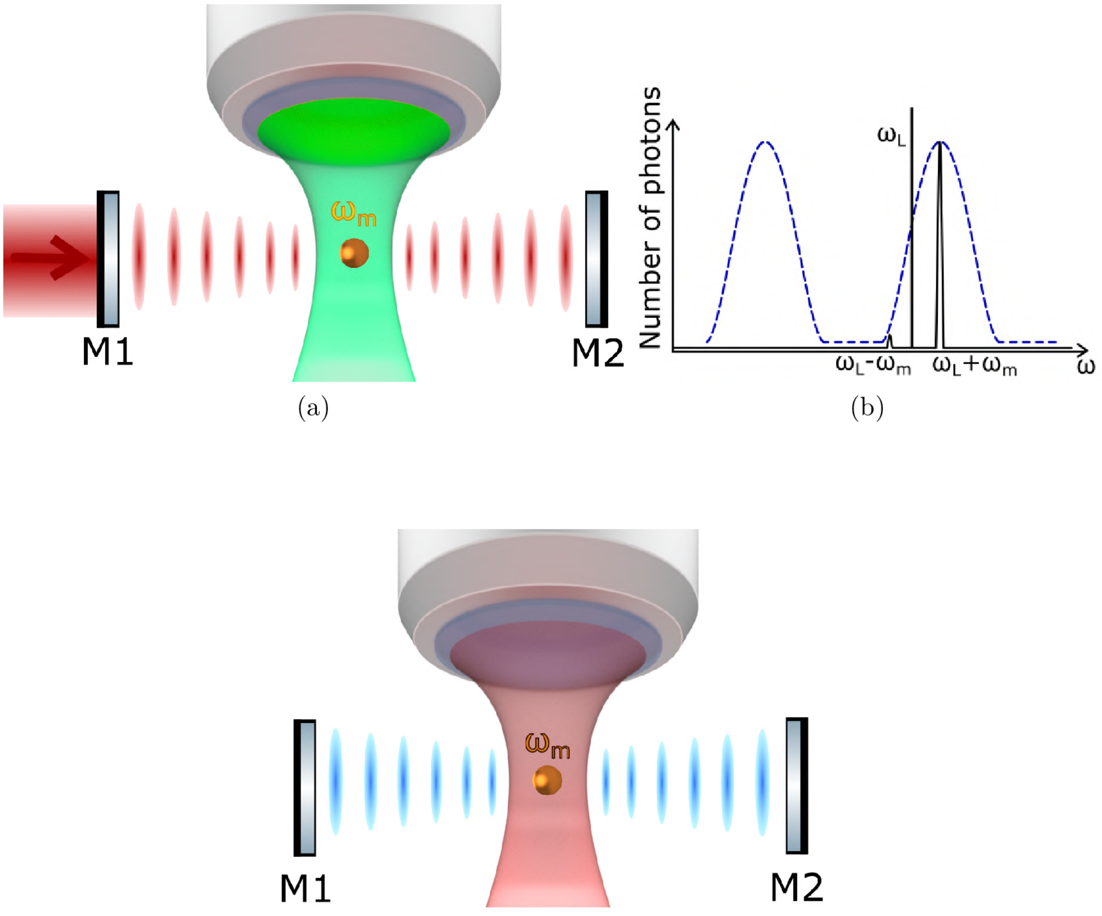

(a) (b)

(c)

Figure 3.2: Schematic representation of the cavity cooling principles. (a) Cavity cooling with the use of an external pump laser (red horizontal beam). The frequency ω_{L} of the pump laser is red-detuned from the cavity resonance, whereas its sideband at $(\omega_{\mathrm{L}}+\omega_{\mathrm{m}})$ is resonant with the cavity; here, ω_{m} is the frequency of mechanical oscillations of the particle trapped in optical tweezers (green vertical beam). The resonance of the cavity with anti-Stokes photons causes enhanced annihilation of phonons from the particle motion, thereby cooling this motion down. (b) Graph showing the principle of cavity cooling. The blue dashed line is the cavity transmission spectrum and the solid black line indicates the spectral profile of the total power transmitted through the cavity. Due to the particle harmonic motion, there are two sidebands with frequencies $(\omega_{\mathrm{L}} \pm \omega_{\mathrm{m}})$. The central pump laser peak at the frequency of ω_{L} is out of resonance with the cavity, whereas the anti-Stokes peak at the frequency of $(\omega_{\mathrm{L}}+\omega_{\mathrm{m}})$ is in resonance. (c) Cavity cooling by coherent scattering from the particle optically trapped in optical tweezers (red vertical beam) into an empty cavity. As the trapped particle oscillates, the scattered light traveling in the cavity (blue horizontal wave) is modulated by these oscillations, featuring both Stokes and anti-Stokes bands. When the cavity is tuned to be in resonance with the anti-Stokes scattered light, the particle motion can be cooled by increased transfer of energy from the particle phonons to the light photons

.

3.3. Cold damping

The last particle cooling method described in this section is cold damping (CD). This method was first developed for cooling trapped ions and mechanically tethered oscillators [40, 41, 42, 43, 44] and it is relatively new in the optical levitation community. The CD is based on the application of a controlled external force via an active feedback loop that acts against the instantaneous direction of the particle velocity vector and whose magnitude is proportional to the particle speed. This increases the effective damping rate experienced by the particle and slows down its motion. The external damping force dissipates the energy of the particle through an effective friction coefficient. However, in contrast to the viscous damping, this additional friction does not act as a coupling element between the particle and the surrounding heat bath, so it is not bound by the fluctuation-dissipation theorem. The particle can then be efficiently cooled without being reheated due to collisions with the molecules of the surrounding atmosphere [45]. This evasion of the fluctuation-dissipation theorem led to the introduction of the name of the method: “cold damping”.

In order to apply this cooling method to an optically levitated particle, it is most convenient to work with charged particles and use the Coulomb force acting on them in an external electric field [46, 47] (see Fig. 3.3). With a suitable configuration of the field-generating electrodes and of the optical system for detecting the position of the levitated particle, a uniform electric field with controlled amplitude can be used to cool the motion of the particle along multiple spatial directions. To achieve this, it must be guaranteed that the resonant frequencies of the particle oscillations along these directions are sufficiently different from each other.

Any realistic measurement of the particle position, which serves as an input for the feedback loop to determine the correct cold damping force, is subject to imprecision. The measurement noise is amplified by the control loop and, subsequently, acts as an additional stochastic driving source. Thus, the feedback loop simultaneously cools and heats the motion of the particle and the balance between the two effects depends on the level of the measurement noise.

The main difficulty associated with the use of cold damping is the need to physically implement the electrodes in the experimental set-up, which can be challenging in terms of designing a suitable electrode layout compatible with spatial constraints, especially when cooling multiple axes. In addition, simultaneous cooling of multiple axes using a uniform electric field requires careful shaping of the laser beam that allows the separation of the resonant eigenfrequencies along different directions. Our team came up with successful solutions to these issues that will be described in Section 3.4. The main advantage of cold damping is the possibility of more efficient cooling and, consequently, achieving lower effective kinetic temperatures of the center-of-mass motion than attainable with parametric feedback cooling [33, 35].

In the following two subsections, the modified Langevin equation that includes the cold damping force and the effects of the position detection noise will be introduced and its solution in the form of the position PSD will be derived.

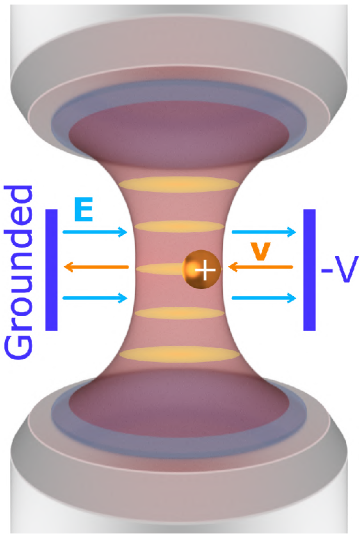

Figure 3.3: Schematic of the cold damping cooling method. A positively charged particle is optically trapped in a dual-beam trap and its position is continuously monitored by a suitable detector (not shown). Electrodes (blue rectangles) create an electric field **E** (light blue arrows) controlled by the potential V of the right electrode, which acts against the particle velocity vector **v** (orange arrows) and dissipates the kinetic energy through effective friction decoupled from the surrounding viscous environment.

3.3.1. Langevin equation for levitated particle and cold damping

Similar to Section 2.2.1, let us assume a charged particle is trapped in a harmonic potential in a low-vacuum atmosphere. The motion of the particle will be again described using the Langevin equation. Compared to Eq. (2.9), the particle is now also affected by the electric force whose amplitude is controlled by the cold damping feedback loop. Other forces including the harmonic confinement force, viscous drag due to the ambient atmosphere, and thermal stochastic Langevin force remain the same as in Eq. (2.9). Following [35, 40, 42, 46], the equation of motion with the cold damping terms can be written as

$$m\ddot{x}(t) + \gamma\dot{x}(t) + m\omega_{0x}^2 x(t) = F_{\mathrm{th}}(t) - g\gamma[\dot{x}(t-\tau) + \dot{x}_{\mathrm{n}}(t-\tau)], \tag{3.1}$$

where g represents the gain of the feedback loop implementing the cold damping (the effective friction coefficient for cold damping is then $g\gamma$) and $x_{\mathrm{n}}(t)$ is the position measurement noise, which adds to the actual particle position as $x(t)+x_{\mathrm{n}}(t)$. The noise of the feedback loop that leads to random fluctuations of the cold damping force was considered to be small compared to $g\gamma x_n$; thus, it was omitted in Eq. (3.1). In contrast with the mentioned references [35, 40, 42, 46], we consider that the feedback loop does not respond infinitely fast and has an overall delay of τ compared to the instantaneous particle velocity $\dot{x}(t)$. Therefore, the feedback loop applies the net force

$$-g\gamma[\dot{x}(t-\tau) + \dot{x}_{\mathrm{n}}(t-\tau)] \tag{3.2}$$

to the particle. The first term in Eq. (3.2) is the actual cold damping force connected to the delayed particle velocity that causes the cooling of the particle thermal motion. The second term in Eq. (3.2) then describes stochastic driving caused by the measurement noise of the position detector that is amplified by the control loop and fed back to the particle.

Upon the Fourier transform and substitution $\gamma = m\Gamma$, Eq. (3.1) can be expressed in the frequency domain as

$$-m\omega^2\hat{x}(\omega) + \mathrm{i}m\omega\Gamma\hat{x}(\omega) + m\omega_{0x}^2\hat{x}(\omega) = \hat{F}_{\mathrm{th}}(\omega) - \mathrm{i}m\omega g\Gamma\hat{x}(\omega)e^{-\mathrm{i}\omega\tau} - \mathrm{i}m\omega g\Gamma\hat{x}_{\mathrm{n}}(\omega)e^{-\mathrm{i}\omega\tau}, \tag{3.3}$$

where the factor $e^{-\mathrm{i}\omega\tau}$ reflects the delay of the feedback loop. Equation (3.3) can be solved for the particle position $\hat{x}(\omega)$ as

$$\hat{x}(\omega) = \frac{\frac{1}{m}\hat{F}_{\mathrm{th}}(\omega) - \mathrm{i}\omega g\Gamma e^{-\mathrm{i}\omega\tau}\hat{x}_{\mathrm{n}}(\omega)}{\omega_{0x}^2 - \omega^2 + \mathrm{i}\omega\Gamma(1 + ge^{-\mathrm{i}\omega\tau})}. \tag{3.4}$$

The position of the particle $\hat{x}(\omega)$ is thus influenced by the measurement noise entering the feedback loop.

External detection of the particle position, expressed in Eq. (3.4), adds the measurement noise $x_{\mathrm{n}}(t)$ and the particle position $x(t) + x_{\mathrm{n}}(t)$ is detected. In the Fourier domain, this leads to the frequency response of the form

$$\hat{x}(\omega) + \hat{x}_{\mathrm{n}}(\omega) = \frac{\frac{1}{m}\hat{F}_{\mathrm{th}}(\omega) + [\omega_{0x}^2 - \omega^2 + \mathrm{i}\omega\Gamma]\hat{x}_{\mathrm{n}}(\omega)}{\omega_{0x}^2 - \omega^2 + \mathrm{i}\omega\Gamma(1 + ge^{-\mathrm{i}\omega\tau})}. \tag{3.5}$$

Let us now roughly estimate the behavior of the particle in limiting conditions. Let us assume that the gain g at the resonance frequency $\omega = \omega_{0x}$ is large enough so that the first term $\hat{F}_{\mathrm{th}}/m$ in the nominator of Eq. (3.4) can be neglected and $\omega_{0x}\tau \to 0$. We then obtain

$$\hat{x}(\omega_{0x}) = -\frac{ge^{-\mathrm{i}\omega_{0x}\tau}\hat{x}_{\mathrm{n}}(\omega_{0x})}{1 + ge^{-\mathrm{i}\omega_{0x}\tau}} \to -\hat{x}_{\mathrm{n}}(\omega_{0x}). \tag{3.6}$$

where the amplitude of the particle resonant frequency response is approximately equal to the amplitude of the driving detector noise and the two quantities are in opposite phases. Under similar conditions, the on-resonance measurement of the particle position, $\hat{x}(\omega_{0x}) + \hat{x}_{\mathrm{n}}(\omega_{0x})$, drops well below the high-frequency noise floor of the detection system and supports the detection of low amplitudes of the particle motion.

In contrast, for negligible measurement noise $\hat{x}_{\mathrm{n}}(\omega)$ and low feedback gain g, the feedback loop contributes to the damping Γ in a complex way depending on the delay τ of the feedback loop:

$$\hat{x}(\omega) = \frac{\frac{1}{m}\hat{F}_{\mathrm{th}}(\omega)}{\omega_{0x}^2 - \omega^2 + \mathrm{i}\omega\Gamma(1 + ge^{-\mathrm{i}\omega\tau})}. \tag{3.7}$$

3.3.2. PSD of the trapped particle position in the presence of cold damping

In the following, we will assume that the thermal Langevin force $F_{\mathrm{th}}(t)$ and the measurement noise $x_{\mathrm{n}}(t)$ are uncorrelated at all times, i.e. $\langle F_{\mathrm{th}}(t)x_{\mathrm{n}}(t')\rangle = 0$, or, in the frequency domain, at all frequencies: $\langle \hat{F}_{\mathrm{th}}(\omega)\hat{x}_{\mathrm{n}}(\omega')\rangle = 0$.

In calculating the position PSD, we need to distinguish between a position of the particle $x(t)$ (in frequency domain $\hat{x}(\omega)$ given by Eq. (3.4)) and the position of the particle, which is measured on the detector $x(t) + x_{\mathrm{n}}(t)$ (in frequency domain $\hat{x}(\omega) + \hat{x}_{\mathrm{n}}(\omega)$ given by Eq. (3.5)).

Using the same definition as in Eq. (2.20), the PSD of the actual particle displacement $x(t)$ can be expressed as

$$\begin{aligned} S_{x,\mathrm{CD}}(\omega) &= \lim_{T_\mathrm{m}\to\infty} \frac{1}{T_\mathrm{m}} |\hat{x}(\omega)|^2 \\ &= \frac{\frac{1}{m^2} S_{F_\mathrm{th}}(\omega) + \omega^2 g^2 \Gamma^2 S_{x_\mathrm{n}}(\omega)}{(\omega_{0x}^2 - \omega^2)^2 + \omega^2\Gamma^2[1 + g^2 + 2g\cos(\omega\tau)] + 2(\omega_{0x}^2 - \omega^2)\omega g \Gamma \sin(\omega\tau)}, \end{aligned} \tag{3.8}$$

where $S_{F_\mathrm{th}}(\omega)$ is the PSD of the stochastic Langevin force F_th and $S_{x_\mathrm{n}}(\omega)$ is the PSD of the measurement noise x_n. In the following, we will assume that both $S_{F_\mathrm{th}}(\omega)$ and $S_{x_\mathrm{n}}(\omega)$ are constant across the spectrum, i.e., they represent uncorrelated white noises. The PSD of the measured noisy particle position $x(t) + x_\mathrm{n}(t)$ can then be calculated as follows

$$\begin{aligned} S_{x+x_\mathrm{n},\mathrm{CD}}(\omega) &= \lim_{T_\mathrm{m}\to\infty} \frac{1}{T_\mathrm{m}} |\hat{x}(\omega) + \hat{x}_n(\omega)|^2 \\ &= \frac{\frac{1}{m^2} S_{F_\mathrm{th}}(\omega) + [(\omega_{0x}^2 - \omega^2)^2 + \omega^2\Gamma^2] S_{x_\mathrm{n}}(\omega)}{(\omega_{0x}^2 - \omega^2)^2 + \omega^2\Gamma^2[1 + g^2 + 2g\cos(\omega\tau)] + 2(\omega_{0x}^2 - \omega^2)\omega g \Gamma \sin(\omega\tau)}. \end{aligned} \tag{3.9}$$

From the PSD (3.8), it can be seen that the motion of the particle is driven by two terms. The first term proportional to $S_{F_\mathrm{th}}(\omega)$ represents the thermal Langevin force as in the case without feedback and the second term, proportional to $S_{x_\mathrm{n}}(\omega)$, represents the contribution due to the measurement noise entering the feedback loop detector and it is magnified by the feedback loop gain g. Therefore, it is necessary to find an optimal value of the gain to achieve the best cooling performance [42, 46]. Figure 3.4 shows the simulation based on Eq. (3.8) presenting the effect of increasing gain g. In the simulation, it can be seen that increasing gain decreases rapidly the amplitude of the resonance peak and the PSD becomes broader and the particle motion is cooled down. However, when the optimal gain is exceeded (value $g = 2.1$ in the simulated parameters), the opposite effect will occur and the particle will increase its position variance, i.e. it will be heated. The dashed curves correspond to a nonzero feedback loop delay ($\tau = 10^{-5}$ s). In this case, the main peak is shifted towards higher frequencies with increasing g.

Figure 3.5 shows the simulation based on Eq. (3.8) presenting the effect of the feedback time delay τ. Here we fixed the value $g = 0.5$ and monitored the behavior of the system for the case of different τ. Under studied conditions, the peak shifts in frequency in both directions and its amplitude increases or decreases. Therefore, cooling and also heating at various frequencies can occur depending on values of τ.

If the measurement noise term (proportional to S_{x_n} and gain g) is much smaller than the term giving the thermal excitations (proportional to S_{F_th}), i.e.

$$\omega_{0x}^2 g^2 \Gamma^2 S_{x_\mathrm{n}} \ll \frac{S_{F_\mathrm{th}}}{m^2} \implies S_{x_\mathrm{n}} \ll \frac{S_{F_\mathrm{th}}}{m^2 \omega_{0x}^2 g^2 \Gamma^2}, \tag{3.10}$$

Eqs. (3.8) and (3.9) reduce to

$$S_{x,\mathrm{CD}}(\omega) \approx \frac{\frac{1}{m^2} S_{F_\mathrm{th}}}{(\omega_{0x}^2 - \omega^2)^2 + \omega^2\Gamma^2[1 + g^2 + 2g\cos(\omega\tau)] + 2(\omega_{0x}^2 - \omega^2)\omega g \Gamma \sin(\omega\tau)}, \tag{3.11}$$

$$S_{x+x_\mathrm{n},\mathrm{CD}}(\omega) \approx \frac{\frac{1}{m^2} S_{F_\mathrm{th}}}{(\omega_{0x}^2 - \omega^2)^2 + \omega^2\Gamma^2[1 + g^2 + 2g\cos(\omega\tau)] + 2(\omega_{0x}^2 - \omega^2)\omega g \Gamma \sin(\omega\tau)} + S_{x_\mathrm{n}}. \tag{3.12}$$

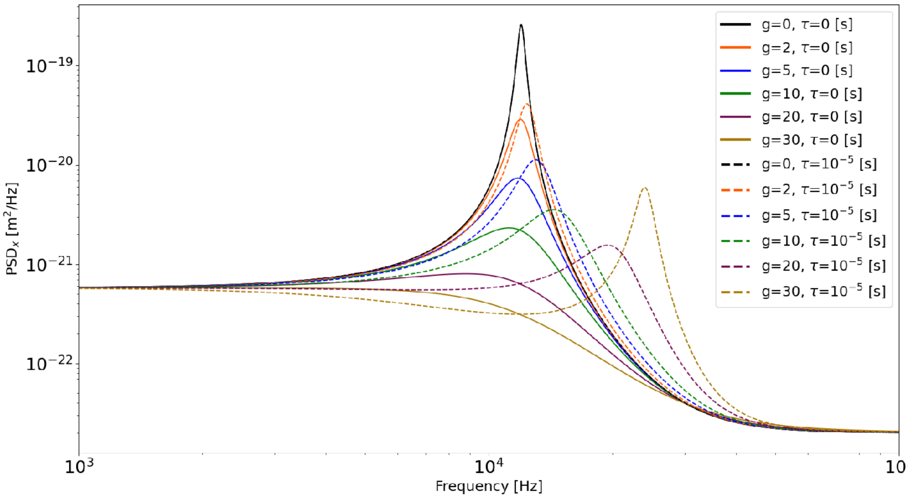

Figure 3.4: Simulation of the effect of finding the optimal gain for cooling of the system of the levitated nanoparticle in harmonic trap based on Eq. (3.8). The solid lines represent the case with zero delay of the feedback loop $\tau = 0$ and the dashed lines with the time delay $\tau = 10^{-5}\,$s, to visualize its influence better. Parameters of the system were close to experimental ones $T_{\text{eff}} = 300\,\text{K}$, $\omega_{0x}/2\pi = 12\,\text{kHz}$, $\Gamma/2\pi = 557\,\text{Hz}$, $S_{x_\text{n}} = 2 \cdot 10^{-23}\,\text{m}^2/\text{Hz}$.

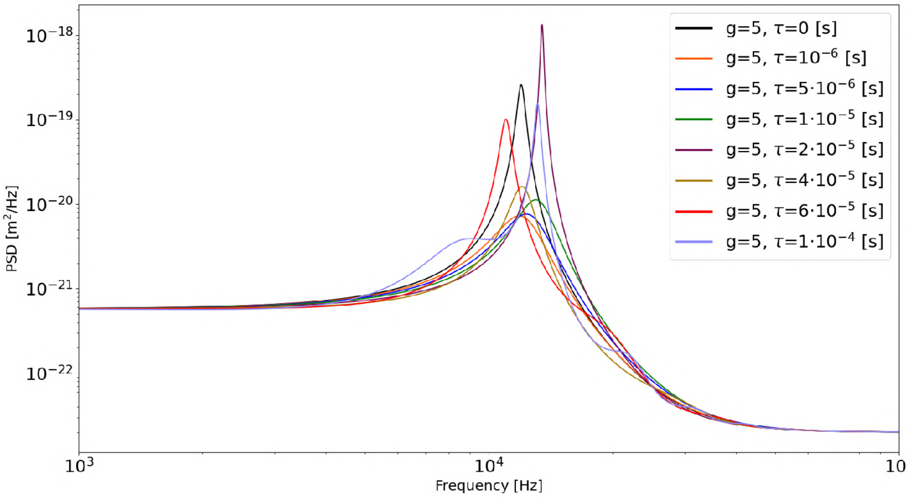

Figure 3.5: Simulation of the effect of time delay τ on the PSD of a levitated nanoparticle in the harmonic trap based on Eq. (3.8). Parameters of the system were the same as in Fig. 3.4 and the gain was fixed at $g = 5$.

According to Eqs. (3.11) and (3.12), the power spectrum $S_{x,\text{CD}}(\omega)$ of the actual particle displacement can be calculated by subtracting the constant PSD S_{x_n} of the measurement noise from the measured power spectrum: $S_{x,\text{CD}}(\omega) = S_{x+x_\text{n},\text{CD}}(\omega) - S_{x_\text{n}}$ [42]. This formula can also be derived upon neglecting the term proportional to $\hat{x}_\text{n}(\omega)$ in Eq. (3.4) and then reevaluating the PSD equal to $|\hat{x}(\omega)|^2$ as before.

3.4. 2D cold damping in uniform electric field

In this subsection, the theory of 2D cold damping of a charged particle optically trapped in a uniform external electric field will be presented. The geometry for implementing this cooling protocol is schematically illustrated in Fig. 3.6. The particle is confined in a laser beam with an elliptical cross-section, which ensures different oscillation eigenfrequencies along the two perpendicular trapping directions aligned with the major and minor axis of the ellipse; these characteristic directions define the x- and y-axis of the coordinate system. Cold damping force is then produced by a uniform electric field E applied in a direction rotated by an angle α with respect to the x-axis. Because the components of the cold damping force along the x- and y-axis derive from a single electric field, the equations of motion along the two coordinate axes will be mutually coupled. The solution of the coupled equations of motion will be carried out in the frequency domain, using the formalism of the power spectral density of particle positions along the x- and y-axis.

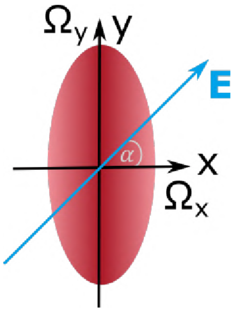

Figure 3.6: Schematic illustration of the cold damping geometry for simultaneous 2D cooling of the motion of an optically trapped charged particle in a single uniform electric field. The particle is confined in a laser beam with an elliptical cross-section (intensity distribution in the beam is represented by different shades of red color – darker color corresponds to higher intensity) and the x- and y-axis of the coordinate system are oriented along the main axes of the ellipse. Because of the elliptical shape of the beam, oscillation eigenfrequencies Ω_x along the x-axis and Ω_y along the y-axis are different. Cold damping force is then represented by the electric force created by the uniform electric field $\mathbf{E}$ is applied at an angle α with respect to the x-axis.

For the configuration shown in Fig. 3.6, the magnitude of the electric field E acting on the positively charged particle is linked to the particle velocities $\dot{x}$ and $\dot{y}$ along the x- and y-axis as

$$E(t) = -gc_x\dot{x}(t-\tau) - gc_y\dot{y}(t-\tau), \tag{3.13}$$

where τ is the time delay of the feedback loop, assumed the same for the x and y signals [i.e., the electric field at time t depends on the past velocities at the time $(t-\tau)$], g is the scalar gain of the feedback loop, and $c_x > 0$ and $c_y > 0$ are the weight coefficients for the x- and y-axis, respectively. By setting the values of c_x and c_y, it is possible to set the ratio of cooling for the two axes. In the case of cooling only one axis, the coefficient of the respective axis is set to one and the other coefficient for the uncooled axis is set to zero; the electric field $\mathbf{E}$ always remains in the same direction. Negative signs in front of both terms of Eq. (3.13) indicate the fact that the cold damping force acts against the direction of motion of the particle. The components of the electric force along the x- and y-axis can then be expressed in the form

$$\begin{aligned} F_{\mathrm{el}x} &= qE\cos(\alpha) = qg[-c_x\dot{x}(t-\tau) - c_y\dot{y}(t-\tau)]\cos(\alpha), &(3.14)\\ F_{\mathrm{el}y} &= qE\sin(\alpha) = qg[-c_x\dot{x}(t-\tau) - c_y\dot{y}(t-\tau)]\sin(\alpha). &(3.15)\end{aligned}$$

The equations of motion along the x- and y-axis can be expressed in the following form

$$\begin{aligned} \ddot{x} &= -\Gamma_x\dot{x} - \frac{\kappa_x}{m}x + \frac{F_{\mathrm{el}x}}{m} + \frac{F_{\mathrm{th}x}}{m}, &(3.16)\\ \ddot{y} &= -\Gamma_y\dot{y} - \frac{\kappa_y}{m}y + \frac{F_{\mathrm{el}y}}{m} + \frac{F_{\mathrm{th}y}}{m}, &(3.17)\end{aligned}$$

where m is the particle mass, $\Gamma_{x(y)}$ are the damping rates due to the ambient atmosphere, $\kappa_{x(y)}$ are the trap stiffnesses, and $F_{\mathrm{th}x(\mathrm{th}y)}$ are the stochastic Langevin forces that are uncorrelated along the two axes. The oscillation eigenfrequencies along the two trapping directions are then given by $\Omega_{x(y)} = \sqrt{\kappa_{x(y)}/m}$.

For the sake of clarity, the above equations of motion can be expressed using a single matrix equation. Therefore, a column vector $\mathbf{r} = \begin{bmatrix} x \\ y \end{bmatrix}$ will be introduced to represent both axes. In the time domain, the resulting equation of motion in the matrix form can be written as

$$\ddot{\mathbf{r}}(t) = -\mathbf{Z}\dot{\mathbf{r}}(t) - \mathbf{K}\mathbf{r}(t) - \mathbf{G}\dot{\mathbf{r}}(t-\tau) + \frac{\mathbf{F}_{\mathrm{th}}}{m}, \tag{3.18}$$

where $\mathbf{F}_{\mathrm{th}} = \begin{bmatrix} F_{\mathrm{th}x} \\ F_{\mathrm{th}y} \end{bmatrix}$ is the column vector of stochastic Langevin forces and $\mathbf{K}$, $\mathbf{Z}$, and $\mathbf{G}$ are matrices with the following forms

$$\begin{aligned} \mathbf{K} &= \begin{bmatrix} \Omega_x^2 & 0 \\ 0 & \Omega_y^2 \end{bmatrix}, &(3.19)\\ \mathbf{Z} &\approx \begin{bmatrix} \Gamma_x & 0 \\ 0 & \Gamma_y \end{bmatrix}, &(3.20)\\ \mathbf{G} &= \frac{qg}{m}\begin{bmatrix} c_x\cos(\alpha) & c_y\cos(\alpha) \\ c_x\sin(\alpha) & c_y\sin(\alpha) \end{bmatrix} = \begin{bmatrix} G_{xx} & G_{xy} \\ G_{yx} & G_{yy} \end{bmatrix}. &(3.21)\end{aligned}$$

Here, $\mathbf{K}$ is the stiffness matrix that represents the trapping force acting on the particle for the given displacement (expressed using the eigenfrequencies of the system), $\mathbf{Z}$ matrix represents the viscous damping of the system, and the gain matrix $\mathbf{G}$ represents the influence of the external electric force applied to the charged particle through the feedback loop. From Eqs. (3.19)–(3.21), it is obvious that the only term responsible for coupling between the x- and y-axis is the gain matrix $\mathbf{G}$ associated with the feedback loop, which contains off-diagonal terms G_{xy} and G_{yx}.

By applying the Fourier transform to Eq. (3.18), it is possible to express the equation of motion in the frequency domain as

$$-\omega^2\hat{\mathbf{r}}(\omega) = -\mathrm{i}\omega\mathbf{Z}\hat{\mathbf{r}}(\omega) - \mathbf{K}\hat{\mathbf{r}}(\omega) - \mathrm{i}\omega\mathbf{G}\hat{\mathbf{r}}(\omega)\mathrm{e}^{-\mathrm{i}\omega\tau} + \frac{\hat{\mathbf{F}}_{\mathrm{th}}}{m}, \tag{3.22}$$

where $\hat{\mathbf{r}}(\omega)$ is the position vector in the frequency domain. From Eq. (3.22), $\hat{\mathbf{r}}(\omega)$ can be expressed in the following form

$$\begin{aligned}\hat{\mathbf{r}}(\omega) &= \begin{pmatrix} -\omega^2 + \mathrm{i}\omega\Gamma_x + \Omega_x^2 + \mathrm{i}\omega \mathrm{e}^{-\mathrm{i}\omega\tau} G_{xx} & \mathrm{i}\omega \mathrm{e}^{-\mathrm{i}\omega\tau} G_{xy} \\ \mathrm{i}\omega \mathrm{e}^{-\mathrm{i}\omega\tau} G_{yx} & -\omega^2 + \mathrm{i}\omega\Gamma_y + \Omega_y^2 + \mathrm{i}\omega \mathrm{e}^{-\mathrm{i}\omega\tau} G_{yy} \end{pmatrix}^{-1} \frac{\hat{\mathbf{F}}_{\mathrm{th}}}{m} \\ &\equiv \begin{pmatrix} P_{Ixx} & \mathrm{i}\omega \mathrm{e}^{-\mathrm{i}\omega\tau} G_{xy} \\ \mathrm{i}\omega \mathrm{e}^{-\mathrm{i}\omega\tau} G_{yx} & P_{Iyy} \end{pmatrix}^{-1} \frac{\hat{\mathbf{F}}_{\mathrm{th}}}{m} \\ &= \frac{1}{D} \begin{pmatrix} P_{Iyy} & -\mathrm{i}\omega \mathrm{e}^{-\mathrm{i}\omega\tau} G_{xy} \\ -\mathrm{i}\omega \mathrm{e}^{-\mathrm{i}\omega\tau} G_{yx} & P_{Ixx} \end{pmatrix} \frac{\hat{\mathbf{F}}_{\mathrm{th}}}{m},\end{aligned} \tag{3.23}$$

where

$$\frac{1}{D} = \frac{1}{P_{Ixx}P_{Iyy} + \omega^2 \mathrm{e}^{-2i\omega\tau} G_{xy} G_{yx}}. \tag{3.24}$$

Neglecting the measurement noise, the final PSD characterizing the particle position in 2D cold damping geometry can be expressed in the following matrix form

$$\begin{aligned}\mathbf{S} &= \lim_{T_{\mathrm{m}}\to\infty} \frac{1}{T_{\mathrm{m}}} \hat{\mathbf{r}}(\omega) \cdot \hat{\mathbf{r}}^{T*}(\omega) = \\ &= \frac{S_{F_{\mathrm{th}}}}{m^2|D|^2} \begin{pmatrix} |P_{Iyy}|^2 + \omega^2 |G_{xy}|^2 & \mathrm{i}\omega \mathrm{e}^{\mathrm{i}\omega\tau} G_{yx}^* P_{Iyy} - \mathrm{i}\omega \mathrm{e}^{-\mathrm{i}\omega\tau} G_{xy} P_{Ixx}^* \\ -\mathrm{i}\omega \mathrm{e}^{-\mathrm{i}\omega\tau} G_{yx} P_{Iyy}^* + \mathrm{i}\omega \mathrm{e}^{\mathrm{i}\omega\tau} G_{xy}^* P_{Ixx} & |P_{Ixx}|^2 + \omega^2 |G_{yx}|^2 \end{pmatrix},\end{aligned} \tag{3.25}$$

where * denotes complex conjugation, ^{T} denotes matrix transposition, and $||$ denotes the absolute value. Non-zero cross-terms that lie off the diagonal of the matrix $\mathbf{S}$ indicate a correlation between motion along the x- and y-axis.

3.5. Cold damping experiments with one particle

In this section, the details of the experimental set-up for cold damping (CD) of one particle will be described (detection part, feedback loops for 1D and 2D CD). It will then be explained how to properly align the detection path to minimize crosstalks between the trapping axes. After that, the core of the course of experiments with a single particle will be presented, and at the end, the data evaluation procedures and used theoretical models will be introduced.

3.5.1. Experimental set-up for cold damping experiments with one particle

The schema of the experimental set-up for CD experiments with one particle is shown in Fig. 3.7. Using the DMD, a single optical trap was created in the VCH, in which a particle was stably confined. The trapping part was already described in detail in Section 2.3.1, so I will focus more on the detection part here.

To detect the position of the levitated particle, the polarization of the trapping beam propagating from the bottom to the top in Fig. 3.7 was rotated by ~ 5 degrees using

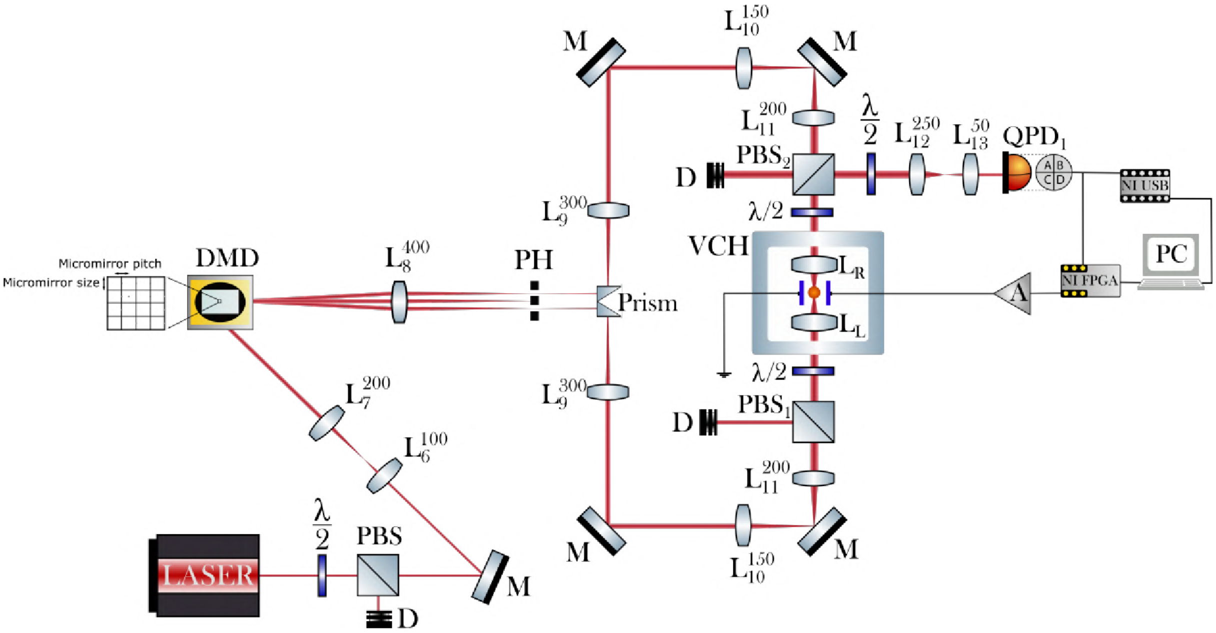

Figure 3.7: Schema of the experimental set-up for cold damping experiments with one particle. The used abbreviations were previously defined in Fig. 2.7.

the half-wave plate placed in front of the VCH. Due to this small polarization change, a part of the trapping beam could be diverted towards QPD_1 by PBS_2. Using a pair of lenses L_{12} and L_{13}, the beam size was adjusted to precisely cover the QPD_1 chip. Voltage signals from QPD_1 were fed to the NI FPGA board (NI 5781), which provided a feedback signal for CD, and also to the NI USB card (NI USB 6346 BNC), which was used for the data acquisition. Details of the implementation of the feedback loop are described in Section 3.5.2 for 1D CD and in Section 3.5.3 for 2D CD. The sampled data was saved to the control PC, which also allowed changing the gain values for the CD feedback loop and sending the user settings to the FPGA. To perform larger cooling interventions, an amplifier A was connected to the output of the FPGA board, which amplified the signal 15 times. The output signal from the amplifier was then brought to one electrode in the VCH, while the second electrode was grounded. Using this arrangement, we had full control over the magnitude of the applied voltage controlling the particle motion via the CD process.

3.5.2. Feedback loop for 1D cold damping

The electronic feedback loop served as the main experimental part for the creation of the cold damping force. Figure 3.8 schematically illustrates the control process implemented in the FPGA card. The position signal from QPD_1 was fed into the FPGA card, where it was digitized. This digitized signal is then passed through a low-pass filter with a cut-off frequency at 300 kHz. In this process, we filtered out higher frequencies above the cut-off frequency, which could introduce additional noise into the feedback loop and, thus, cause poor cooling. The next step implemented in the FPGA card was the conversion of the positional signal into the velocity one. This was done by the numerical derivative calculated from the difference of two consecutive position samples divided by the sampling time step. The last step of the feedback process was multiplying the velocity signal with an appropriate constant, which represented the net electronic gain g of the feedback loop (in Fig. 3.8, this step is labeled as $\times c_x$). All parameters of the FPGA algorithm (settings of the low-pass filter and electronic gain) were controlled via the computer.

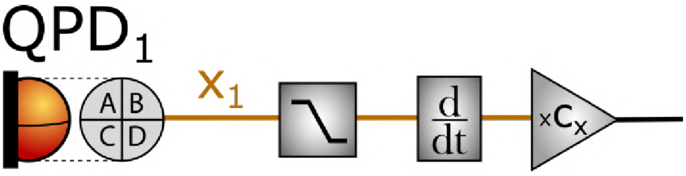

Figure 3.8: Control process for 1D CD implemented in FPGA board.

3.5.3. Feedback loop for 2D cold damping

The main difference between 1D and 2D CD lies in changing the transverse intensity profile of the trapping laser beam and cooling both x- and y-axis simultaneously. In the previous case of 1D CD, we used a trapping beam with a circular Gaussian intensity profile. Hence, the trapping frequencies along the x and y axes were separated from each other only very little (ideally not at all). In contrast, for 2D CD, we used the DMD to create an elliptical beam profile, as shown in Fig. 3.4, thus ensuring that the trapping frequencies along both axes were further apart. The overall flow of the FPGA algorithm in 2D CD, illustrated in Fig. 3.9, was similar to the 1D case described in the previous section. First, the x and y position signals from QPD$_1$ were fed into the FPGA card and digitized. Both digitized signals are then passed through separate signal processing paths identical to the 1D case. Specifically, both position signals were separately low-pass filtered, converted to the corresponding velocity signals (but now two positions were subtracted in the loop and the sampling time step division was hidden into gain g, outside the loop), and multiplied by independent electronic gains ($\times c_x$ for the x-axis and $\times c_y$ for the y-axis). Finally, both signals were summed together and it was also possible to apply an additional electronic gain identical for both axes. Usually, I first found the desired ratio between cooling along the x- and y-axis, which I set using the individual gains $\times c_x$ and $\times c_y$ for each axis. With the help of the common gain g, I then adjusted the overall cooling gain. In the final output signal, which was brought to the electrode, the cooling forces for both axes were encoded.

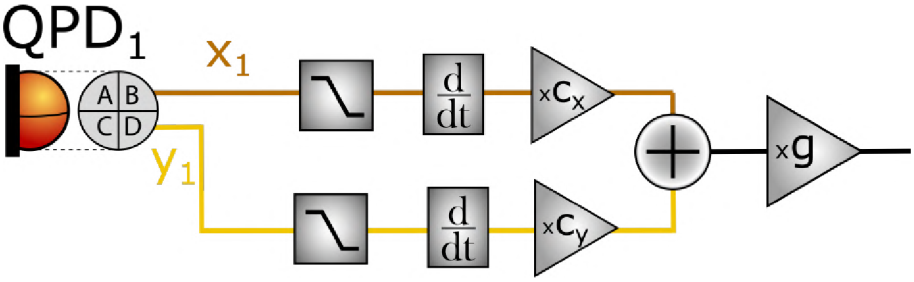

Figure 3.9: Control process for 2D CD implemented in FPGA board.

3.5.4. Alignment of the position detection path for one particle

After successful stable confinement of the particle in the optical trap and evacuation of the vacuum chamber to the required pressure (2 mbar for 1D cooling, 0.5 mbar for 2D cooling), it was necessary to fine-tune the position detection path, minimize the crosstalks between the trapping axes, and maximize the frequency of the particle oscillation.

First, the QPD detector was centered on the detection beam so that the DC-coupled output signal of the QPD oscillated around zero voltage. The position of incidence of the detection beam on the QPD could be controlled either by moving the relay lens placed in front of the QPD or by shifting the QPD itself.

In the case of 2D cooling, when the trapping/detection beam was elliptical, it was also necessary to minimize the crosstalks between the x- and y-axis due to the elliptical shape of the beam by the correct alignment of the major axes of the ellipse with the QPD axes. These crosstalks were minimized by rotating the QPD to the appropriate correct orientation. During the alignment process, the crosstalks were observed in real-time using the position PSDs of all axes calculated by the LabView program running in the control PC.

Subsequently, the frequencies of particle oscillations were maximized by adjusting the mirrors in the trapping beam paths (located between the prism creating the two independent trapping paths and the vacuum chamber) along the x- and y-axis. The high oscillation frequency is generally an indicator of a good alignment of the dual-beam trap. In addition, position detection tends to be less noisy at higher frequencies. Finally, at higher frequencies, it is possible to achieve smaller occupation numbers (indirectly proportional to the oscillation frequency, see Section 3.1 in the theoretical part) at the given effective temperature of the particle and, thus, get closer to the ground state of the particle center-of-mass motion.

3.5.5. The course of the experiment for one particle

After stable trapping of the particle (see Section 2.5.2) and the correct setting of the detection path (see Section 3.5.4), everything was prepared for the experiment itself. I had already implemented the electrodes in the vacuum chamber as a part of my bachelor's thesis; therefore, everything was ready for the cooling experiments. Using a signal generator, I first applied a sinusoidal voltage to the electrodes and observed the particle response to verify that the particle was charged. When the particle reacted to the applied electric field, the feedback loop was turned on and the charge polarity was tested to ensure proper setting of the feedback gain to achieve cooling (not heating) of the particle motion. Subsequently, I tried several different feedback loop gains and approximately mapped the region where the cooling of the particle motion occurred and to which values of the feedback gain it was approximately safe to cool. After that, I applied feedback voltages with different gains to the electrodes and gradually recorded the resulting positional trajectory of the particle using the QPD. Typically, I recorded 200 000 positions in 1 second-long recording.

3.5.6. Data evaluation for one optically levitated and cooled particle

All single-particle cooling data were processed in the Python programming language, using my own code. After loading the experimental data, calibration was first performed, which was described in detail in Section 2.6.1. After determining the calibration constant $c_{\mathrm{V,m}}$, which converts the raw data in volts to meters, and multiplying the measured trajectories with $c_{\mathrm{V,m}}$, the calibrated variances of positions for both axes x and y could be calculated.

The level of detection noise was determined from the calibrated particle trajectories recorded without cooling (feedback gain $g = 0$). Under these conditions, the trapped particle is in thermodynamic equilibrium with the ambient atmosphere and the variance of its position $\langle x^2 \rangle$ follows the equipartition theorem. Since the random detection noise is uncorrelated with the actual position of the particle, the total variance $\langle x^2_{\mathrm{meas}} \rangle$ of the measured noisy trajectories is given by the sum of $\langle x^2 \rangle$ and the net variance due to the measurement noise $\langle x^2_{\mathrm{noise}} \rangle$: $\langle x^2_{\mathrm{meas}} \rangle = \langle x^2 \rangle + \langle x^2_{\mathrm{noise}} \rangle$. As argued in Section 2.6.1, at sufficiently high frequencies $f_{\mathrm{noise}} \geq 0.75 f_{\mathrm{Nyq}}$, the position PSD P_x of the experimental data only contains the contribution from the detection noise. Assuming this noise adds a constant background P_x^{∞} to the experimental PSD, the net variance of the noise over the accessible spectral range $\langle 0; f_{\mathrm{Nyq}} \rangle$ can be calculated as $\langle x^2_{\mathrm{noise}} \rangle = P_x^{\infty} f_{\mathrm{Nyq}}$. Alternatively, $\langle x^2_{\mathrm{noise}} \rangle$ can also be determined from fitting the theoretical model for the position PSD of a harmonic oscillator (Eq. (2.20) in the theoretical part) to the experimental position PSD. For a known particle mass m, the oscillation eigenfrequency ω_0 obtained from the fit gives the stiffness of the trap $\kappa = m\omega_0^2$. The expected variance of the particle position at the ambient temperature T is then given by the equipartition theorem as $\langle x^2 \rangle = \frac{k_{\mathrm{B}}T}{\kappa}$. Thus, $\langle x^2_{\mathrm{noise}} \rangle$ can be determined as $\langle x^2_{\mathrm{meas}} \rangle - \langle x^2 \rangle$, where $\langle x^2_{\mathrm{meas}} \rangle$ is directly calculated from the experimental data. $\langle x^2_{\mathrm{noise}} \rangle$ came out nearly identical from both calculation methods. Assuming that the detection noise is not affected by the activation of the feedback loop, the value of $\langle x^2_{\mathrm{noise}} \rangle$ determined for $g = 0$ also holds for the trajectories of cooled particles.

Position PSDs of experimental trajectories were calculated using Welch windowing [48] and the resulting spectra were fitted using model equations from the theoretical part (Eq. (2.20) for the uncooled case with the gain $g = 0$ and Eq. (3.9) for the cooled case with active feedback). Fitting of the position PSDs was divided into two steps. In the first step, I fitted only the data recorded without cooling and found the values of the resonant frequency ω_0, the viscous damping rate Γ, and the peak amplitude, which I labeled as A_{eff} (in the graph labeled as A_{eff} optimal). A_{eff} is connected to the theoretical model in the following form: $A_{\mathrm{eff}} = S_{F_{\mathrm{th}}}/m^2$. Quantities ω_0, Γ, and A_{eff} were considered fixed even when the cooling was switched on because the electric field should not affect them. For the case of cooling turned on, I only fitted the values of the delay of the feedback loop τ and of the net gain g. These parameters are directly affected by the feedback loop, cause different shapes of the PSDs spectra and histograms, and change the effective kinetic temperature of the particle.

The same procedure was also used for evaluating the data from 2D cooling of a single particle. The only difference was in the theoretical model used for the experimental data fitting. In the case of 2D cooling, I used for fitting Eq. (3.12), with specific terms set according to the target cooled axis. Specifically, when cooling just one axis, the other coefficient in the $\mathbf{G}$ matrix (either G_{xx} or G_{yy}) was set to zero.

3.6. 1D cold damping of one particle – results

In this section, all experimental results related to 1D cold damping of the motion of one optically levitated particle will be presented. In the reported experiments, the particle was confined in a dual-beam trap with a symmetric circular transverse profile of the optical intensity and its motion was cooled only along the x-axis oriented in the direction of the electric field.

Figures 3.10 and 3.11 show the experimental PSDs of the particle position along the cooled x- and uncooled y-axis obtained with an increased gain of the feedback loop fitted by the theoretical model based on Eq. (3.9).

In Fig. 3.10, there is a significant decrease in the amplitude and broadening of the PSD peaks with increasing feedback loop gain. Because the decrease of the amplitude is much quicker than the broadening of the peak, it corresponds to the smaller variance of the particle trajectory for higher gains, i.e., cooling of the particle motion, and increase of the damping of the system due to the cold damping term. The maximum of all peaks gradually shifts to larger frequencies with the increasing gain of the feedback loop due to the time delay τ_x of the loop.

In Fig. 3.11, due to the absence of active cooling along this axis, all PSD peaks have identical amplitudes and widths. From the comparison of Figs. 3.10 and 3.11, it is evident that the cooling took place only along the x-axis (Fig. 3.10) and in the y-axis the PSD remain constant with varying feedback gain (see Fig. 3.11). According to Eq. (2.22) from the theoretical part, the integral of the PSD corresponds to the variance of the particle motion. Therefore, if the amplitude of the peak decreases quicker than the peak's broadening, the variance of the motion decreases, exactly as we would expect from the effect of cooling. At the same time, the peak broadens, which also agrees with the theory, since the width of the peak is directly proportional to the damping of the system. Because the effect of cold damping can be imagined as additional damping of the system, with increasing the gain of the cooling feedback loop, the damping of the system must increase and, thus, the peak broadens.

As was said in the previous paragraph, the experimental spectra were fitted by the theoretical model based on Eq. (3.9), as described in Section 3.5.6. By fitting the experimental data I obtained these parameters: resonant frequency $\omega_{0x,y}$, damping due to the ambient atmosphere $\Gamma_{x,y}$, time delay of the feedback loop $\tau_{x,y}$, gain of the feedback loop g, amplitude of the peak $A_{x,y}$. The resonant frequencies of the particle oscillations $\omega_{0x,y}$ in both axes were calculated by fitting the data without cooling (gain $= 0$). The final values are $\omega_{0x}/2\pi = 1.8 \cdot 10^4\,\mathrm{Hz}$ and $\omega_{0y}/2\pi = 1.6 \cdot 10^4\,\mathrm{Hz}$. The damping of the system Γ due to the ambient atmosphere in the vacuum chamber for both axis was calculated by fitting the data without cooling (gain $= 0$) and was assumed to be constant for all cases also with cooling as viscous damping is independent of the applied electric field. The final values are $\Gamma_x/2\pi = 5.6 \cdot 10^2\,\mathrm{Hz}$ and $\Gamma_y/2\pi = 5.7 \cdot 10^2\,\mathrm{Hz}$. The peak amplitude $A_{x,y}$ was also fitted just for data without cooling (gain $= 0$) and was assumed to be constant for all gain cases. This amplitude is associated with the stochastic Langevin force, i.e. with the molecules from the ambient atmosphere which form the thermal bath in which the particle is. Because the ambient atmosphere is not influenced by an electric field, this value also needs to be constant for all cases. The final values are $A_x = 1.2 \cdot 10^3\ \mathrm{m^2s^{-3}}$ and $A_y = 1.2 \cdot 10^3\ \mathrm{m^2s^{-3}}$.

Figure 3.12(a) shows the values of the fitted feedback loop delay τ_x. This parameter was fitted for all cooling cases. For x-axis, the value of τ_x at zero gain is zero (the feedback loop was not active) and the fitted values of τ_x for non-zero gain are close to the independently experimentally measured value of 5.6 µs. After averaging over all non-zero gain values, we obtain $\tau_x = 3.7 \pm 0.9$ µs. For the y-axis we also fitted the values of τ_y and g, but we reached only negligible improvements in the value of the minimized nonlinear function. Because the fitted values of g for the y-axis are close to zero, fitted values of τ_y are of limited physical significance and were not displayed in Fig. 3.12(a).

Figure 3.12(b) shows values of the fitted gain g for both axes and for all cooling cases. For both directions, the values of g at zero gain setting are zero (the feedback loop was not active). For the actively cooled x-axis, the fitted values of g increase linearly with the increasing gain setting. In contrast, for the uncooled y-axis, the fitted values of g are nearly constant and remain near zero.

Figure 3.13 presents calculated values of the final effective temperature for both axes. T_{eff} was calculated using Eq. (2.23) from calibrated variances of the particle motion from which was subtracted the variance of measurement noise was subtracted. The values of $T_{\text{eff},x,y}$ at zero gain setting are equal to the ambient thermodynamic temperature T (the feedback loop was not active). For the actively cooled x-axis, the values of $T_{\text{eff},x}$ decrease with the increasing gain setting, reaching the minimal effective kinetic temperature of ~ 11.6 K at the gain setting of ~ 700. In contrast, for the uncooled y-axis, the values of $T_{\text{eff},y}$ are nearly constant and remain near the ambient thermodynamic temperature T.

The second method for evaluating the effect of the cooling on the particle motion relies on the inspection of the particle position histograms. As explained in the theoretical Section 3.14, we can visualize the probability distribution of the particle positions by the cumulative frequency of the particle occurrence at the given spatial location. Histograms of particle trajectories along the x- and y-axis for a varying gain of the feedback loop are shown in Fig. 3.14. To represent the true probability distributions, both sets of histograms are normalized to unity. Comparison of the x- and y-axis histograms clearly reveals that the motion of the particle along the x-axis becomes more confined with the increasing feedback gain; the histograms get narrower and the height of the histogram peaks increases. In contrast, the overall shape of the y-axis histogram is practically unaffected by the value of the feedback gain. Thus, we succeeded in implementing the 1D CD feedback loop.

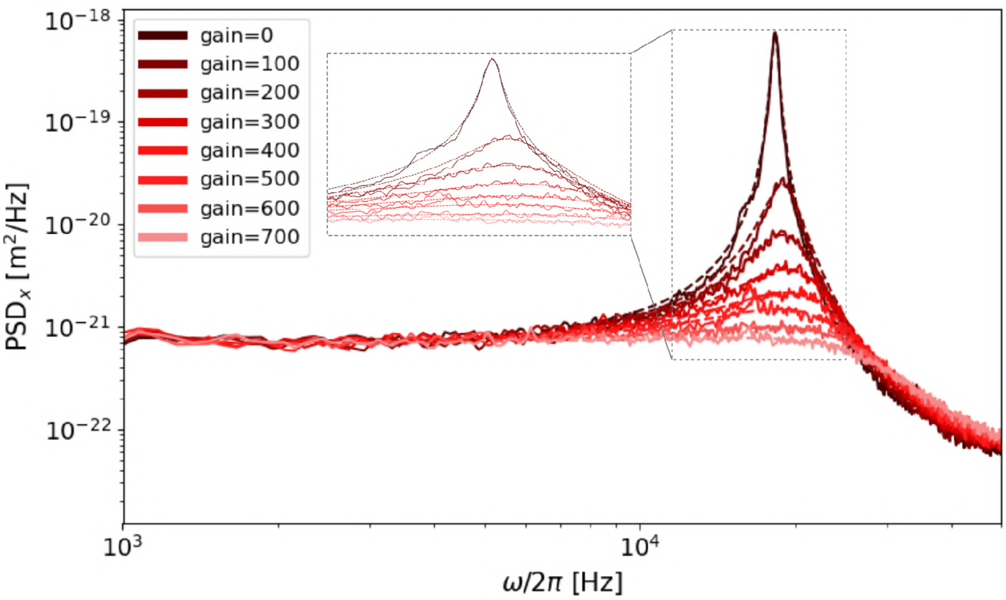

Figure 3.10: Calculated experimental PSDs of the particle position along the actively cooled x-axis (solid lines) for varying settings of the feedback loop gain in the control program (lighter color for higher gains). The experimental spectra were fitted by the theoretical model based on Eq. (3.9) (dashed lines) and the following values were found $\omega_{0x}/2\pi = 1.8 \cdot 10^4$ Hz, $\Gamma_x/2\pi = 5.6 \cdot 10^2$ Hz, $A_x = 1.2 \cdot 10^3\,\mathrm{m^2 s^{-3}}$.

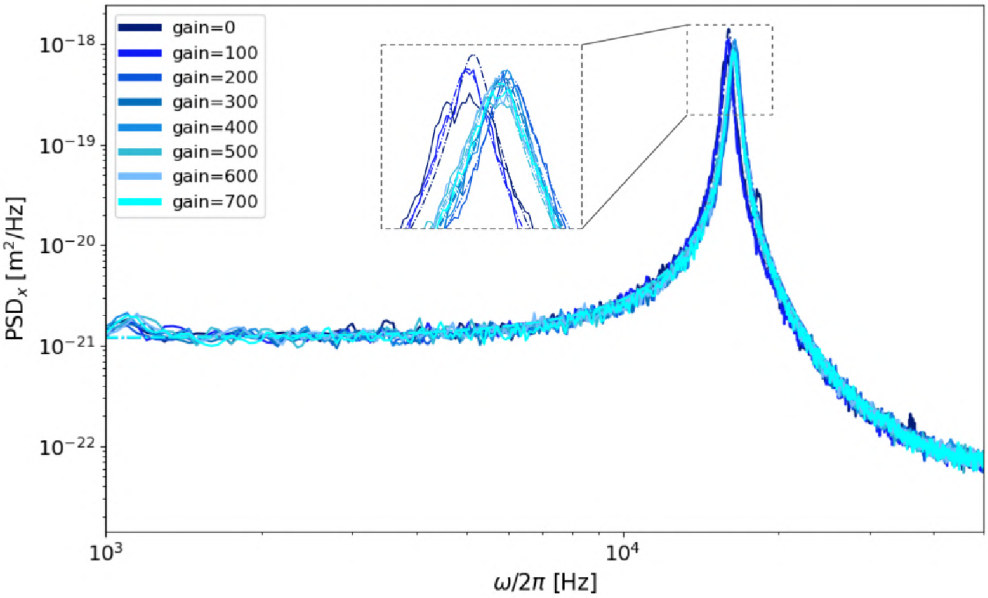

Figure 3.11: Calculated experimental PSDs of the particle position along the uncooled y-axis (solid lines) for varying settings of the feedback loop gain in the control program. The experimental spectra were fitted by the theoretical model based on Eq. (3.9) (dashed lines) and the following values were found $\omega_{0y}/2\pi = 1.6 \cdot 10^4$ Hz, $\Gamma_y/2\pi = 5.7 \cdot 10^2$ Hz, $A_y = 1.2 \cdot 10^3\ \mathrm{m^2 s^{-3}}$.

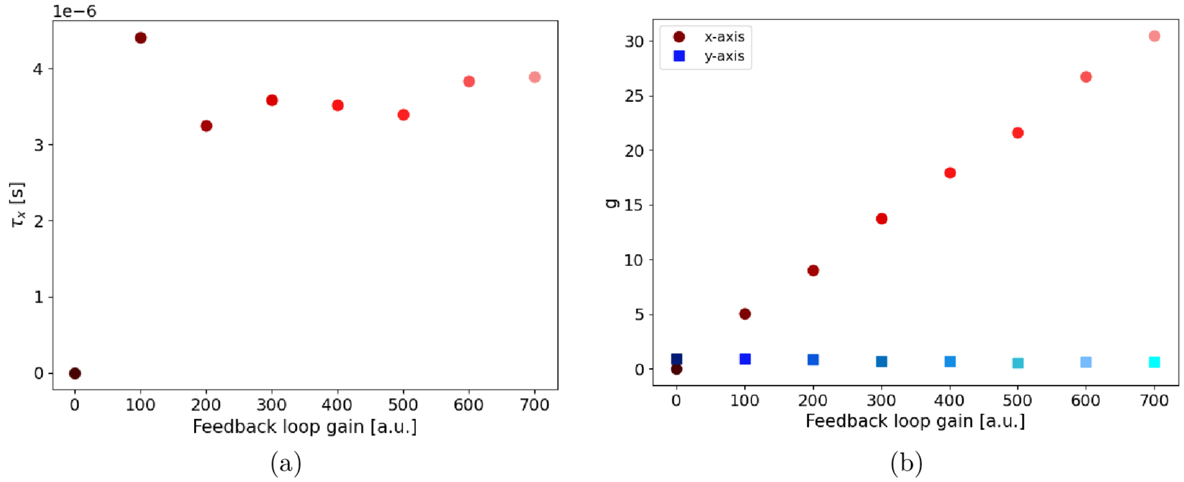

(a) (b)

Figure 3.12: Values of (a) the feedback loop delay τ_x and (b) the actual feedback loop gain g determined from fitting the theoretical model based on Eq. (3.9) to the experimental PSDs of the particle position along the cooled x-axis (red dots) and uncooled y-axis (blue squares, only for (b)) for varying setting of the feedback loop gain in the control program. The x-axis denotes values of the setting of the experimental feedback loop gain in the control program in arbitrary experimental units, which does not have any direct physical meaning.

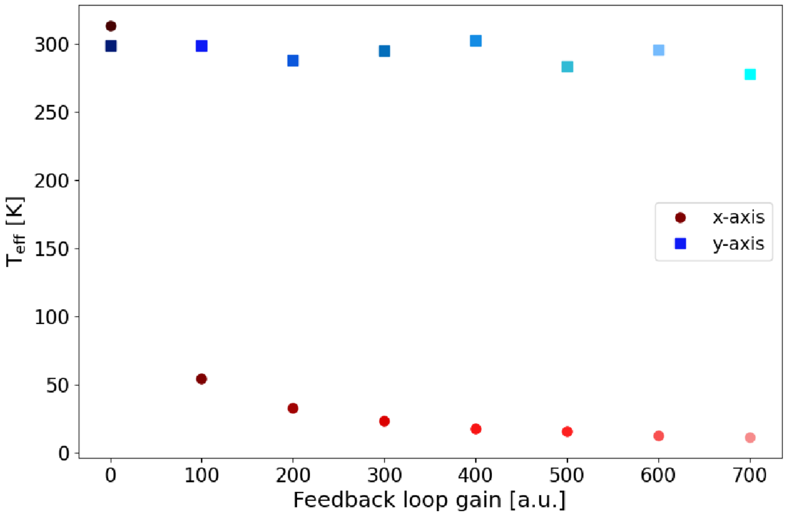

Figure 3.13: Values of the effective kinetic temperature $T_{\mathrm{eff},x,y}$ along the cooled x-axis (red dots) and the uncooled y-axis (blue squares) determined from the true variances of the particle position (see Section 3.5.6 for details) using Eq. (3.9) for varying setting of the feedback loop gain in the control program.

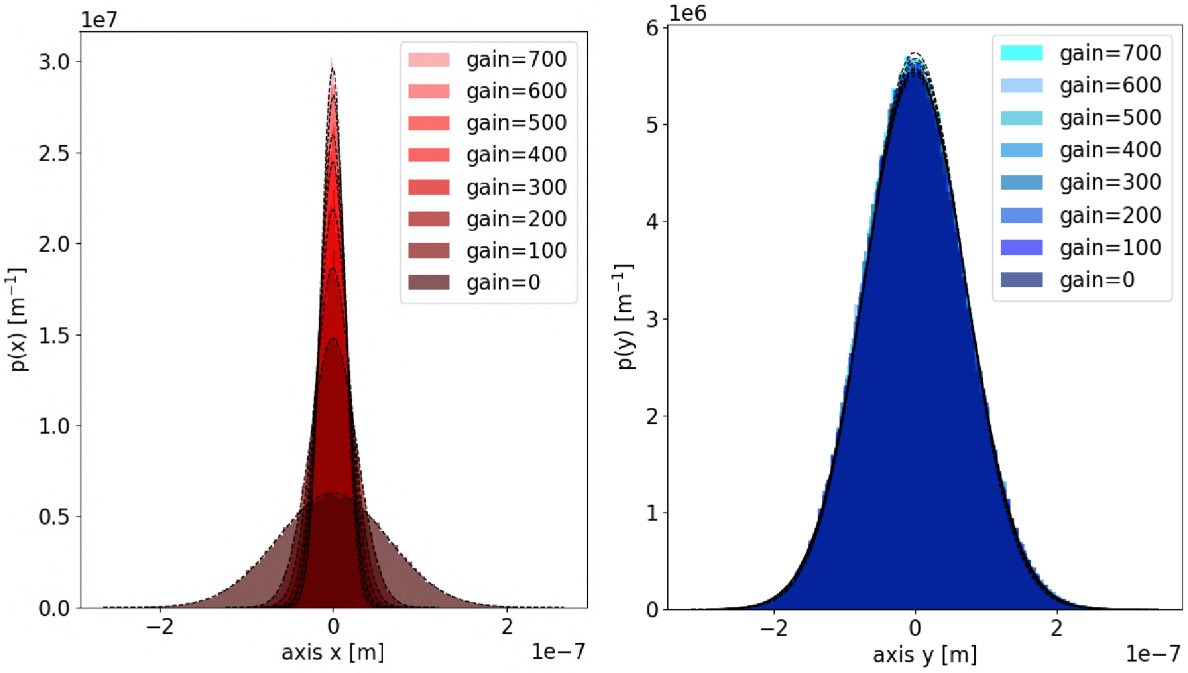

(a) (b)

Figure 3.14: Probability density $p(x)$, $p(y)$ of the particle position along (a) the cooled x-axis and (b) the uncooled y-axis for varying settings of the feedback loop gain in the control program. To represent the true probability distributions, both sets are normalized to unity.

3.7. 2D cold damping cooling by a pair of electrodes – results

In this section, the results of 2D cold damping of one particle will be presented for the ambient pressure 0.5 mbar. In this geometry the elliptical trapping Gaussian beam was created by DMD and the electric field was applied at an angle α (in our experiment $\alpha = 45^\circ$) to the x-axis as shown in Fig. 3.6 in theory part. Therefore, both axes will be influenced by the electrical field and the particle oscillation frequencies along x- and y-axis will be better separated. First of all the data for cooling of one of the axes in this geometry will be presented, i.e. cooling just x-axis (see Subsection 3.7.1). subsequently, data for simultaneous cooling of both x- and y-axis will be presented in Subsection 3.7.2.

3.7.1. Cooling of x-axis only in this geometry

In this subsection, the results of the cooling of x-axis in the geometry of the elliptical beam for 2D cold damping are presented. This means that the cooling coefficient for y-axis was set to zero ($c_y = 0$). This case is analogous to Section 3.6, i.e. the cooling of only one axis in a circular beam profile. Therefore I will only present here the proof that we are able to use this configuration also for the 1D CD case in the form of a PSD, a histogram and the resulting effective kinetic temperature for both axes.

Figure 3.15 shows the resulting experimental PSDs for both axes fitted by a theoretical model based on Eq. (3.25). The PSD for the cooled x-axis shown in part (a) demonstrates a significant decrease in the peak amplitude, which is more significant than the broadening of the peak due to the increase of the cold damping term. This behavior corresponds to the cooling of the particle motion in this axis. The maximum of all peaks gradually shifts to larger frequencies with the increased gain of the feedback loop due to the time delay τ_x of the loop. Due to the absence of active cooling along the uncooled y-axis, all PSD peaks shown in part (b) have identical amplitudes and widths. From the comparison of both graphs, it is evident that the cooling took place just in the x-axis, in which there is a significant decrease and broadening of the peak with increasing feedback loop gain.

The fitting of the theoretical parameters was based on the description in Section 3.5.6. The final values of resonant frequencies for both axes, which were fitted only for the uncooled data and then remained constant for other gains were $\omega_{0x}/2\pi = 2.0 \cdot 10^4$ Hz, $\omega_{0y}/2\pi = 1.3 \cdot 10^4$ Hz. The final value of the damping due to the ambient atmosphere, which was also fitted just for the uncooled case were $\Gamma_x/2\pi = 1.1{\cdot}10^2$ Hz and $\Gamma_y/2\pi = 1.0{\cdot}10^2$ Hz.

In Fig. 3.16 are values of the final effective kinetic temperature for both axes. The kinetic temperature was calculated based on theoretical Eq. (2.23) from calibrated variances of the particle motion from which the variance of measurement noise was subtracted. The values of $T_{\mathrm{eff},x,y}$ at zero gain setting are equal to the ambient thermodynamic temperature T (the feedback loop was not active) for both axes. The values $T_{\mathrm{eff},y}$ for the uncooled y-axis remained approximately constant with ambient temperature. However, for the actively cooled x-axis, the values of $T_{\mathrm{eff},x}$ decrease with an increasing gain setting, reaching the minimal effective kinetic temperature of 13.4 K at the gain setting of 300. This value is comparable to the minimal T_{eff} reached for 1D CD.

Figure 3.17 shows the second method of evaluation of the cooling effect for both axes based on the histograms of particle trajectories along the x- and y-axis for a varying gain of the feedback loop. To represent the true probability distributions, both sets of histograms are normalized to unity. Comparison of the x- and y-axis histograms reveals that the motion of the particle along the x-axis becomes more confined with the increasing feedback gain; the histograms get narrower and the height of the histogram peaks increases. In contrast, the overall shape of the y-axis histogram is practically unaffected by the value of the feedback gain.

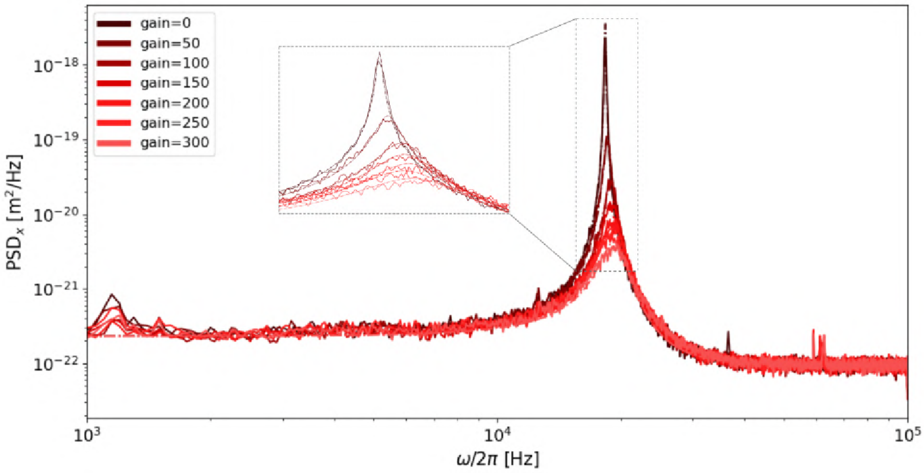

(a)

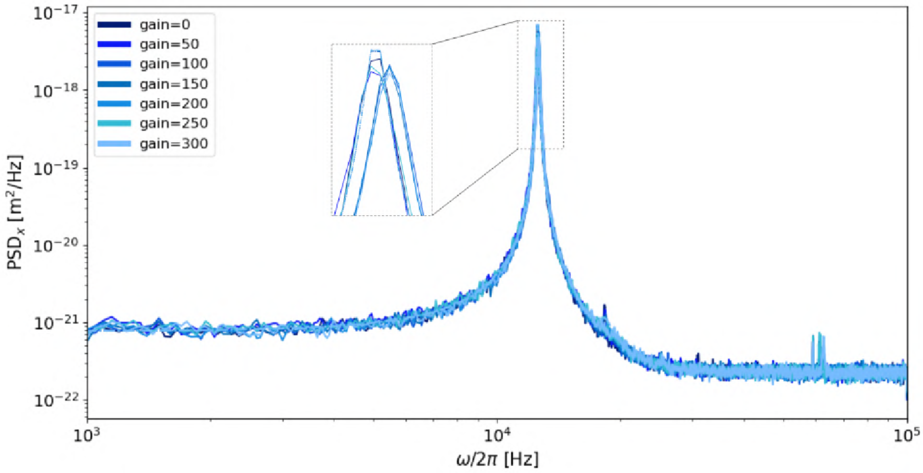

(b)

Figure 3.15: Calculated experimental PSDs of the particle position along the (a) actively cooled x-axis and (b) uncooled y-axis for varying settings of the feedback loop gain in the control program (lighter color for higher gains). The experimental spectra (solid lines) were fitted by the theoretical model based on Eq. (3.25) (dashed lines). The area of the graph is zoomed in on the detail of the peak and the area near it, which carries the most important information for evaluation.

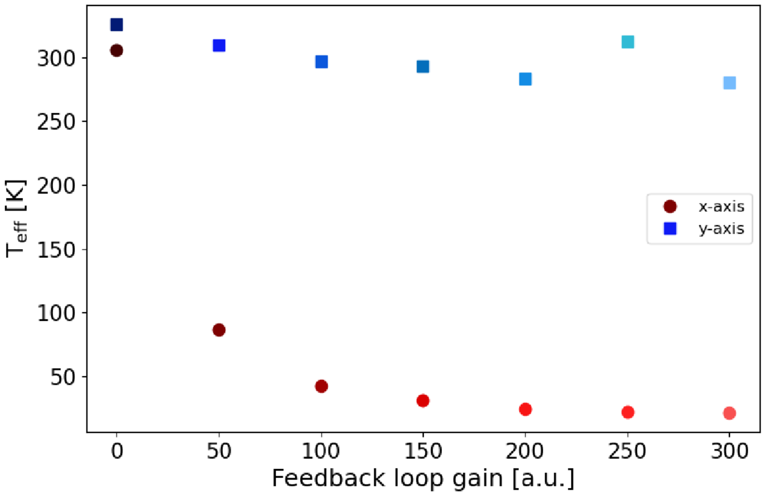

Figure 3.16: Values of the effective kinetic temperature $T_{\mathrm{eff},x,y}$ along the cooled x-axis (red dots) and the uncooled y-axis (blue squares) determined from the true variances of the particle position (see Section 3.5.6 for details) using Eq. (3.25) for varying setting of the feedback loop gain in the control program.

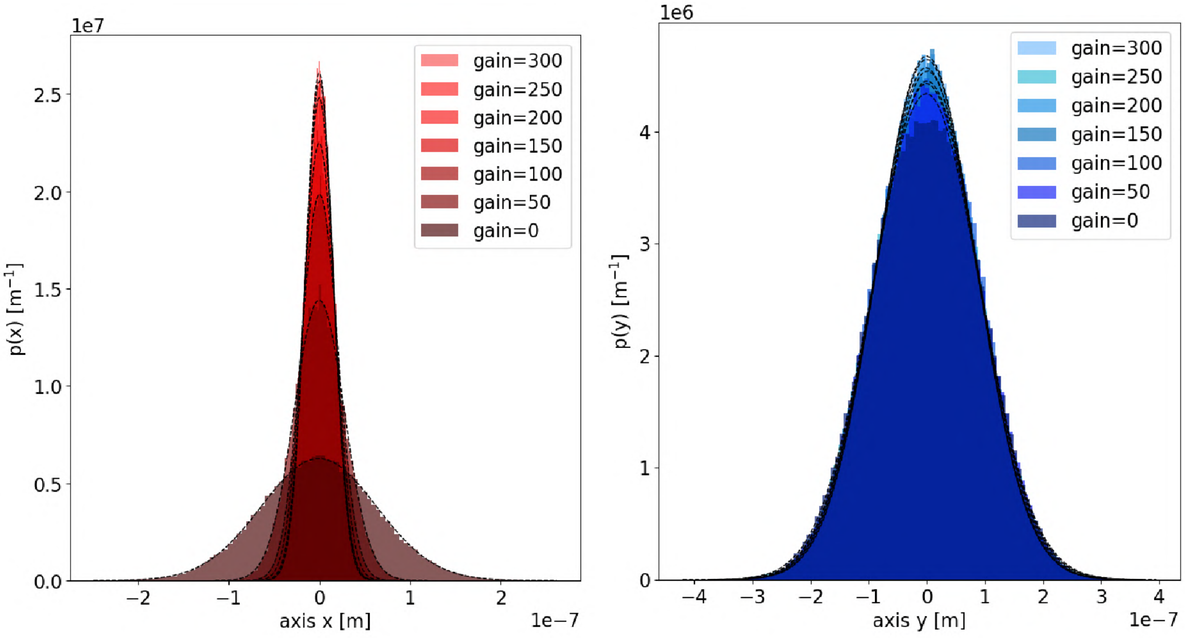

(a) (b)

Figure 3.17: Probability density $p(x)$, $p(y)$ of the particle position along (a) the cooled x-axis and (b) the uncooled y-axis for varying settings of the feedback loop gain in the control program. To represent the true probability distributions, both sets are normalized to unity.

3.7.2. Cooling of both axes x and y simultaneously

In this subsection results of 2D cold damping cooling with elliptical beams are presented in Figs. 3.18–3.22. It can be seen from the plots that the cooling took place in both axes. The final kinetic effective temperature was $T_{\mathrm{eff},x} = 14.0\,\mathrm{K}$ for x-axis and $T_{\mathrm{eff},y} = 13.0\,\mathrm{K}$ for y-axis.

The resulting experimental PSDs for both cooled axes fitted by a theoretical model based on Eq. (3.25) are shown in Fig. 3.18. There is a significant decrease in the peak amplitudes in both cases, therefore particle motion is cooled in both axes. At the same time, however, there is an increase in crosstalk between both axes (from x-axis to y-axis and also from y- to x-axis), as a result of coupling both axes with a single external electric field. Namely, if one axis is cooled, the second is heated at some frequency band. The maximum of all peaks gradually shifts to larger frequencies with the increasing gain of the feedback loop due to the time delay $\tau_{x,y}$ of the loop.

The fitting of the theoretical parameters was based on the description in Section 3.5.6. The final values of resonant frequencies for both axes, which were fitted only for the uncooled data and then remained constant for other gains were $\omega_{0x}/2\pi = 2.0 \cdot 10^4\,\mathrm{Hz}$, $\omega_{0y}/2\pi = 1.3 \cdot 10^4\,\mathrm{Hz}$. The final value of the damping due to the ambient atmosphere, which was also fitted just for the uncooled case were $\Gamma_x/2\pi = 1.1 \cdot 10^2\,\mathrm{Hz}$ and $\Gamma_y/2\pi = 1.0 \cdot 10^2\,\mathrm{Hz}$. The final values of the peak amplitudes were $A_x = 236.6\,\mathrm{m^2s^{-3}}$ and $A_y = 378.0\,\mathrm{m^2s^{-3}}$. The last two fitted values – feedback loop delay $\tau_{x,y}$ and real gain g of the system were calculated for all values of gains. In Fig. 3.19 there are values for feedback loop delay $\tau_{x,y}$ for both axes. For both axes, the values are by order of magnitude different from the value $\tau = 5.6\,\mathrm{\mu s}$ obtained by independent measurement. By averaging the values for all gains, we obtain the resulting values $\tau_x = 28.6\,\mathrm{\mu s}$ and $\tau_y = 37.1\,\mathrm{\mu s}$. In Fig. 3.20 there are values of the real gains of the system for x- and y-axis. For both axes value of gain is zero for the uncooled case. Since both axes are cooled, the value of the real gain in the system also increases as the increasing of setting gain.

Figure 3.21 shows values of the final effective kinetic temperature for both axes. The kinetic temperature was calculated based on theoretical Eq. (2.23) from calibrated variances of the particle motion from which the variance of measurement noise was subtracted. The values of $T_{\mathrm{eff},x,y}$ at zero gain setting are equal to the ambient thermodynamic temperature T for both axes. Because both axes were cooled, there is a significant decrease in effective kinetic temperature for both axes, reaching the minimal effective kinetic temperature $T_{\mathrm{eff},x}$ 14.0 K for x-axis and $T_{\mathrm{eff},y}$ 13.0 K for y-axis at the gain setting of 300.

Figure 3.22 shows the histograms of particle trajectories along the x- and y-axis for varying gain of the feedback loop. To represent the true probability distributions, both sets of histograms are normalized to unity. Comparison of the x- and y-axis histograms clearly reveals that for the 2D case, the motion of the particle along both axes becomes more confined with the increasing feedback gain; the histograms get narrower and the height of the histogram peaks increases.

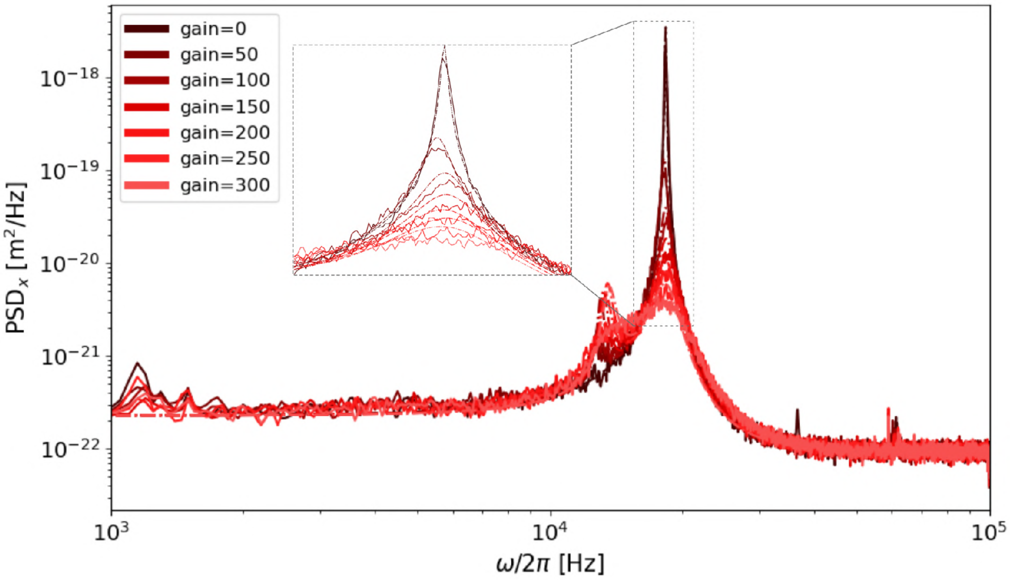

(a)

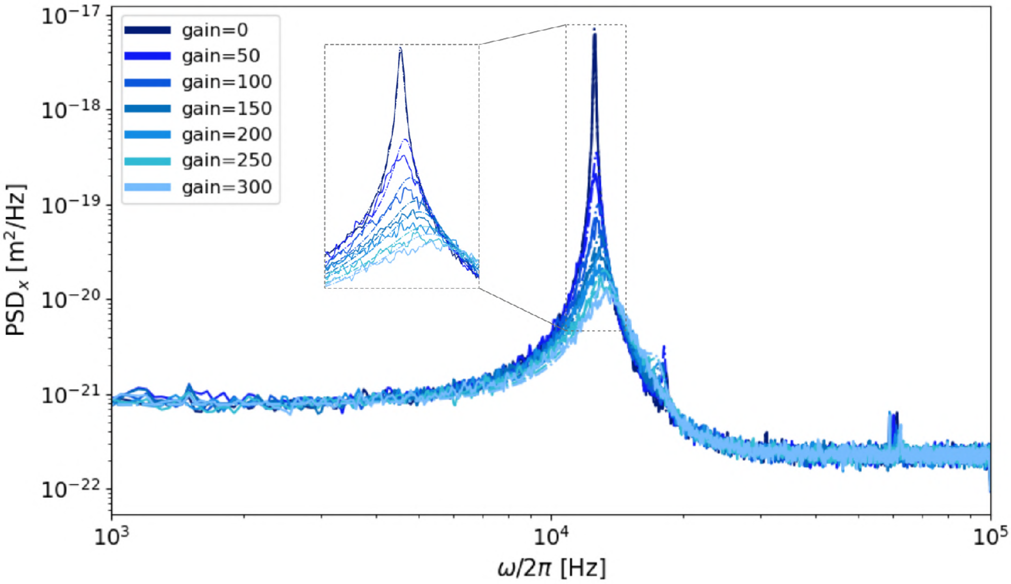

(b)

Figure 3.18: Calculated experimental PSDs of the particle position along the actively cooled (a) x-axis and (b) y-axis for the varying setting of the feedback loop gain in the control program (lighter color for higher gains). The experimental spectra (solid lines) were fitted by the theoretical model based on Eq. (3.25) (dashed lines). The following fitting values were found $\omega_{0x}/2\pi = 2 \cdot 10^4\,\text{Hz}$, $\omega_{0y}/2\pi = 1.3 \cdot 10^4\,\text{Hz}$, $\Gamma_x/2\pi = 1.1 \cdot 10^2\,\text{Hz}$, $\Gamma_y/2\pi = 1.0 \cdot 10^2\,\text{Hz}$, $A_x = 236.6\,\text{m}^2\text{s}^{-3}$ and $A_y = 378.0\,\text{m}^2\text{s}^{-3}$. In both series of spectral plots for the x- and y-axis the heating near the resonant frequency of the other axis is caused by the coupling of both axes with a single electric field.

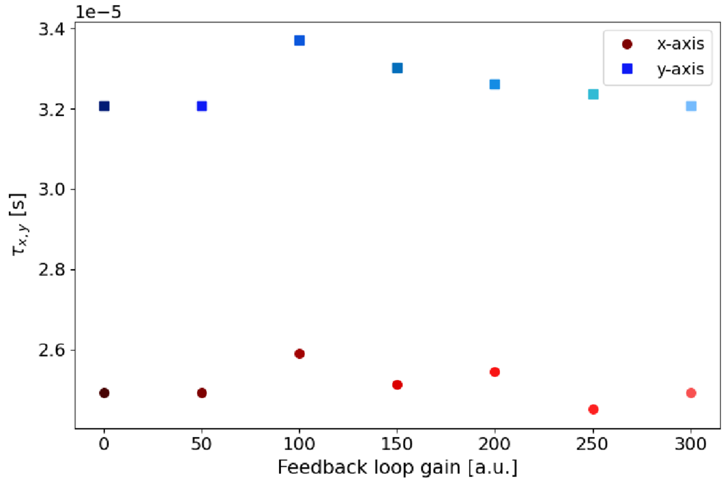

Figure 3.19: Values of the feedback loop delay $\tau_{x,y}$ determined from fitting the theoretical model based on Eq. (2.23) to the experimental PSDs of the particle position along the cooled x-axis (red dots) and y-axis (blue squares) for varying settings of the feedback loop gain.

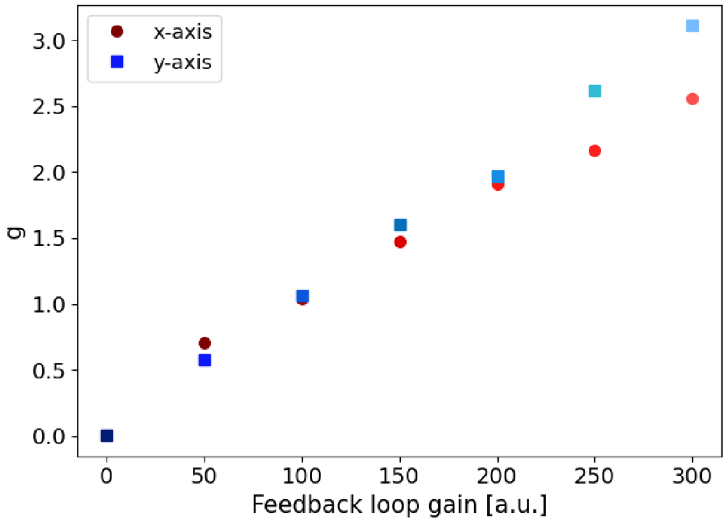

Figure 3.20: Values of the actual feedback loop gain g determined from fitting the theoretical model based on Eq. (3.25) to the experimental PSDs of the particle position along the cooled x-axis (red dots) and the uncooled y-axis (blue squares) for varying setting of the feedback loop gain in the control program.

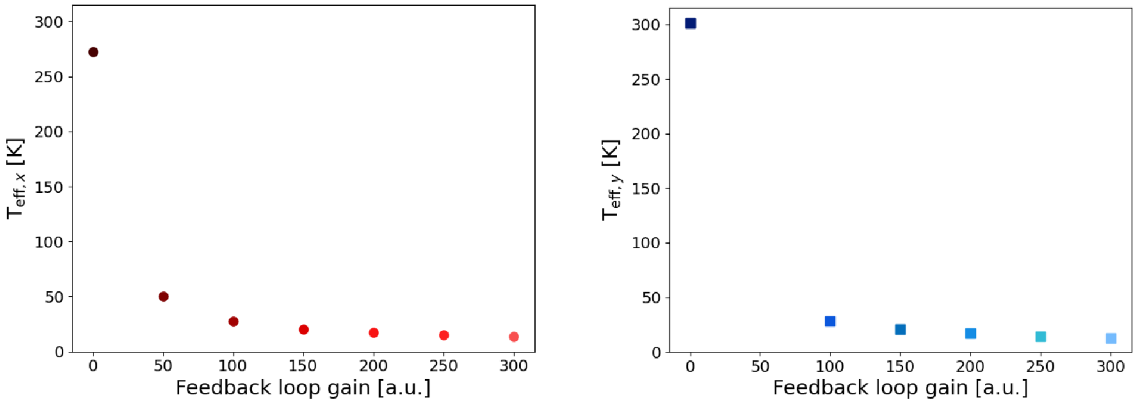

(a) (b)

Figure 3.21: Values of the effective kinetic temperature along (a) the cooled x-axis $T_{\text{eff},x}$ and (b) the cooled y-axis $T_{\text{eff},y}$ determined from the true variances of the particle position (see Section 3.5.6 for details) using Eq. (3.25) for varying setting of the feedback loop gain in the control program.

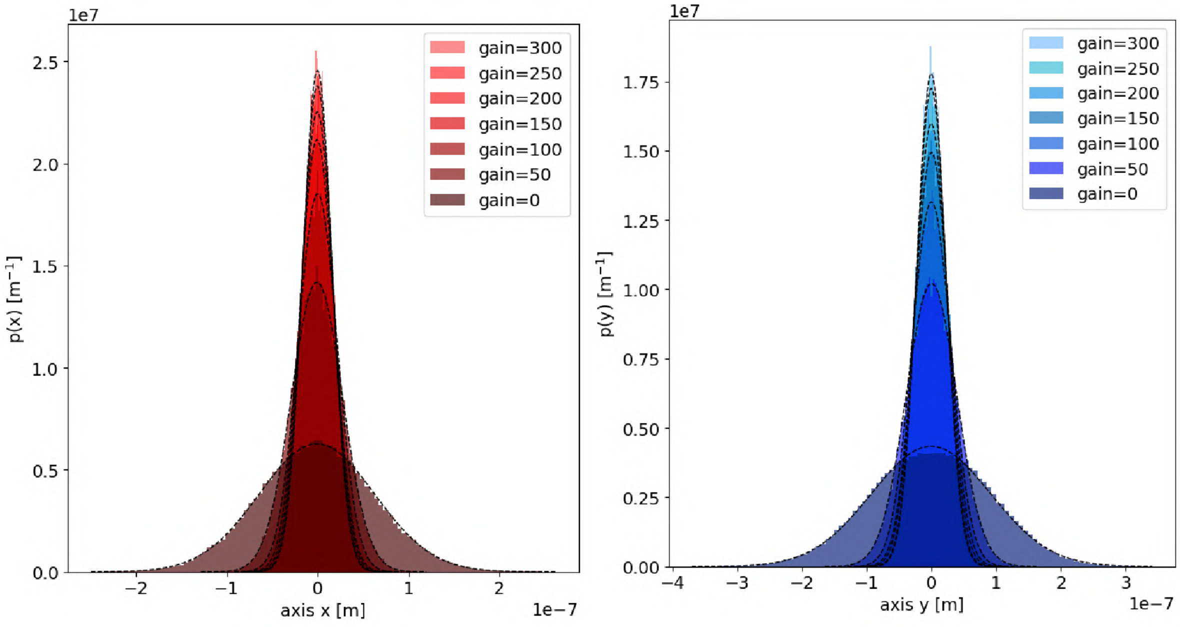

(a) (b)

Figure 3.22: Probability density $p(x)$, $p(y)$ of the particle position along the cooled (a) x-axis and (b) y-axis for varying settings of the feedback loop gain in the control program. To represent the true probability distributions, both sets are normalized to unity.

4. Optical binding and cooling of two levitated particles

4.1. Optical binding of two particles

Optical binding refers to a force interaction between two or more illuminated particles that is mediated by light scattering. As discussed in Section 2.2.1, it is possible to represent a single trapped particle using the harmonic oscillator model. For several optically trapped and bound particles, this model can be extended by considering multiple coupled harmonic oscillators.

In this section, the model of two coupled harmonic oscillators and the concept of their normal modes of oscillation will be explained. Subsequently, basic properties of electric dipole radiation will be presented and the connection between the scattering of light and the optical binding interaction between two levitated nanoparticles will be explored. Next, the theory of the creation of normal modes of oscillation of two optically bound particles will be introduced. Finally, the cooling of normal modes of two optically bound particles confined in separate, coherent optical traps will be described.

4.1.1. Normal modes of oscillation of two coupled harmonic oscillators

Let us consider the case of two particles trapped in mutually separated harmonic optical traps. For the sake of simplicity, let us assume that the particle motion along the three spatial directions is independent and treat the situation as one-dimensional. When a dielectric particle is illuminated by a laser beam, an oscillating electric dipole is induced and begins to emit. If the particles are close enough to each other, the radiated fields from both particles can interact and optical coupling can occur between them. Let us assume that optical binding leads to linear coupling between the two optically trapped particles. Thus, the two particles represent linearly coupled harmonic oscillators. If we assume the configuration shown in Fig. 4.1, the 1D equation of motion for the time-dependent displacements of both particles (without considering losses and driving forces) can be written as [16]

$$m_A\ddot{x}_A + k_A x_A + \kappa(x_A - x_B) = 0, \tag{4.1}$$

$$m_B\ddot{x}_B + k_B x_B - \kappa(x_A - x_B) = 0, \tag{4.2}$$

where $k_{A(B)}$ is the stiffness of confinement of particles A (B) in the corresponding optical potential wells, κ is the coupling stiffness between the two particles, and $x_{A(B)}$ is the displacement of particles A (B) from their respective equilibrium positions.

Let us consider the solution of Eqs. (4.1) and (4.2) in the form $x_{A(B)}(t) = x^{\max}_{A(B)}e^{-\mathrm{i}\omega_\pm t}$, where $x^{\max}_{A(B)}$ are the amplitudes of motion of individual particles and $\omega_\pm$ denotes the newly obtained oscillation eigenfrequencies, and substitute this assumed solution into Eqs. (4.1) and (4.2). We then obtain two coupled linear equations for x_A and x_B

$$x_A(-m_A\omega_\pm^2 + k_A + \kappa) = \kappa x_B, \tag{4.3}$$

$$x_B(-m_B\omega_\pm^2 + k_B + \kappa) = \kappa x_A. \tag{4.4}$$

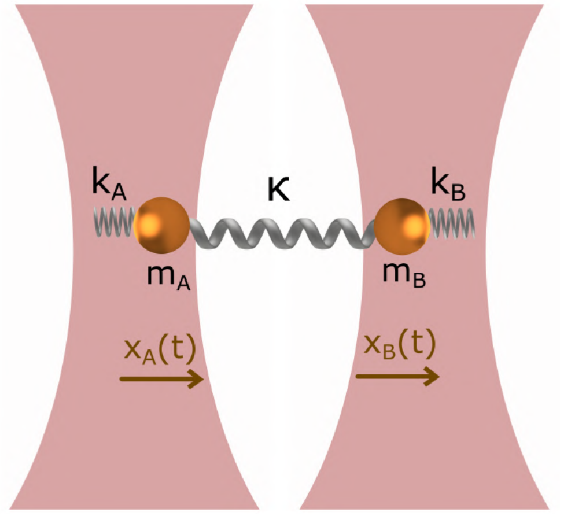

Figure 4.1: Illustration of coupling between two particles confined in two separate optical traps, viewed as two coupled oscillators. Particle A with mass m_A is connected to the optical trap via spring constant k_A, and particle B with mass m_B via spring constant k_B. The coupling term between both particles is represented by the spring constant κ. Time-varying positions $x_A(t)$ and $x_B(t)$ describe particles' displacements from their respective equilibrium positions.

For the sake of compactness, Eqs. (4.3) and (4.4) can be combined into a single equation using the matrix formalism as

$$\begin{bmatrix} -m_A\omega_\pm^2 + k_A + \kappa & -\kappa \\ -\kappa & -m_B\omega_\pm^2 + k_B + \kappa \end{bmatrix} \begin{bmatrix} x_A \\ x_B \end{bmatrix} = 0. \tag{4.5}$$

The first square bracket can be denoted as the matrix $\mathbf{M}$, after which Eq. (4.5) changes to a simplified form:

$$\mathbf{Mx} = 0, \tag{4.6}$$

where $\mathbf{x} = \begin{bmatrix} x_A \\ x_B \end{bmatrix}$ is the column vector of particle positions. Coupled system in Eq. (4.5) can be solved for a nontrivial solution $\mathbf{x}$ only by fulfilling the condition $\det(\mathbf{M}) = 0$. We then obtain the resulting solutions in the form [16]

$$\omega_\pm^2 = \frac{1}{2}\left[\omega_A^2 + \omega_B^2 \mp \sqrt{(\omega_A^2 - \omega_B^2)^2 + 4\Gamma^2\omega_A\omega_B}\right], \tag{4.7}$$

where $\omega_A = \sqrt{\frac{k_A+\kappa}{m_A}}$, $\omega_B = \sqrt{\frac{k_B+\kappa}{m_B}}$, and $\Gamma = \frac{\sqrt{\kappa/m_A}\sqrt{\kappa/m_B}}{\sqrt{\omega_A\omega_B}}$. Equation (4.7) determines the frequencies of the *normal modes*. The first mode with the frequency of ω_+, the so-called "Center-of-mass" motion, is characterized by the movement of the particles in the same direction (both to the right or to the left). The second mode with the frequency of ω_-, the so-called "Breathing" mode, is characterized by the movement of the particles in opposite directions (either towards or away from each other).

If we remove the coupling between both oscillators (i.e., set $\kappa = 0$), we obtain the eigenmode frequencies of the system in the following form: $\omega_{A,0} = \sqrt{k_A/m_A}$ and $\omega_{B,0} = \sqrt{k_B/m_B}$. As expected, these frequencies correspond to the eigenfrequencies of the individual isolated particles.

4.1.2. Radiation of an oscillating electric dipole

An illuminated dielectric sphere can be treated as an oscillating electric dipole if its radius $a \leq \lambda/20$, where λ is the illumination wavelength [17] (i.e., the particle fulfills the Rayleigh approximation, see Section 2.1.3). Such an oscillating dipole emits electromagnetic radiation.

Because of the symmetry of the dipole radiation pattern, it is convenient to express the electric and magnetic intensity vectors in spherical coordinates centered on the dipole (see Fig. 4.2(a)), $\mathbf{E} = (E_r, E_\theta, E_\varphi)$ and $\mathbf{H} = (H_r, H_\theta, H_\varphi)$. Choosing the coordinates so that the induced dipole moment $\mathbf{p}$ is directed along the z-axis, the non-zero electric and magnetic field components have the following form [16]

$$E_r = \frac{|\mathbf{p}|\cos\theta}{4\pi\epsilon_0\epsilon}\frac{e^{\mathrm{i}kr}}{r}k^2\left[\frac{2}{k^2r^2} - \frac{2\mathrm{i}}{kr}\right], \tag{4.8}$$

$$E_\theta = \frac{|\mathbf{p}|\sin\theta}{4\pi\epsilon_0\epsilon}\frac{e^{\mathrm{i}kr}}{r}k^2\left[\frac{1}{k^2r^2} - \frac{\mathrm{i}}{kr} - 1\right], \tag{4.9}$$

$$H_\varphi = \frac{|\mathbf{p}|\sin\theta}{4\pi\epsilon_0\epsilon}\frac{e^{\mathrm{i}kr}}{r}k^2\left[-\frac{\mathrm{i}}{kr} - 1\right]\sqrt{\frac{\epsilon_0\epsilon}{\mu_0\mu}}, \tag{4.10}$$

where $k = 2\pi/\lambda$ is the wavenumber, θ is the angle between the z-axis and the direction of vector $\mathbf{r}$, $\mathbf{r}$ is the position vector from the origin to the place where we measure the field intensity ($r \equiv |\mathbf{r}|$), ϵ is the relative permittivity, ϵ_0 is the permittivity of vacuum, μ is the relative permeability, and μ_0 is the permeability of vacuum.

Depending on the power of term (kr) in the denominator of Eqs. (4.8) - (4.10), we can distinguish three types of dipole radiation - near field, intermediate field and far field. *Near field* is connected to the distance dependence of $(kr)^{-3}$, which means that this field decreases very rapidly with distance and manifests itself primarily for $r \ll \lambda$. This term is present in the electric fields E_r (which does not have any far-field term) and E_θ. Magnetic field H_φ has no near field component. Near field can be observed primarily along the z-axis, as shown in Fig. 4.2(b). *Intermediate field* is associated with the distance dependence of $(kr)^{-2}$ and dominates for cases $r \approx \lambda$. This contribution is present in all three components of the electric and magnetic fields in Eqs. (4.8) - (4.10). Intermediate field radiation represents a transition between the near and far-field radiation. *Far field* is connected to the distance dependence of $(kr)^{-1}$, which means that this field is the most far-reaching of all components and dominates for distances $r \gg \lambda$. It appears just in the field components E_θ and H_φ, electric field E_r does not have any far-field term. Thus, the far field is purely transversal. Because of this, the far-field radiation is zero along the z-axis direction, as shown in Fig. 4.2(c). This directly follows from the $\sin(\theta)$ dependence in Eqs. (4.9) and (4.10).

4.1.3. Optical binding between two optically trapped particles

Optical binding is an interaction between two or more particles illuminated by coherent light and it is mediated by scattered photons. Despite the name “binding”, this interaction can be either repulsive or attractive. Optical binding can be classified into two configurations – longitudinal and lateral binding. In the case of longitudinal binding, the light field propagates in the same direction as is the direction of the binding process. On

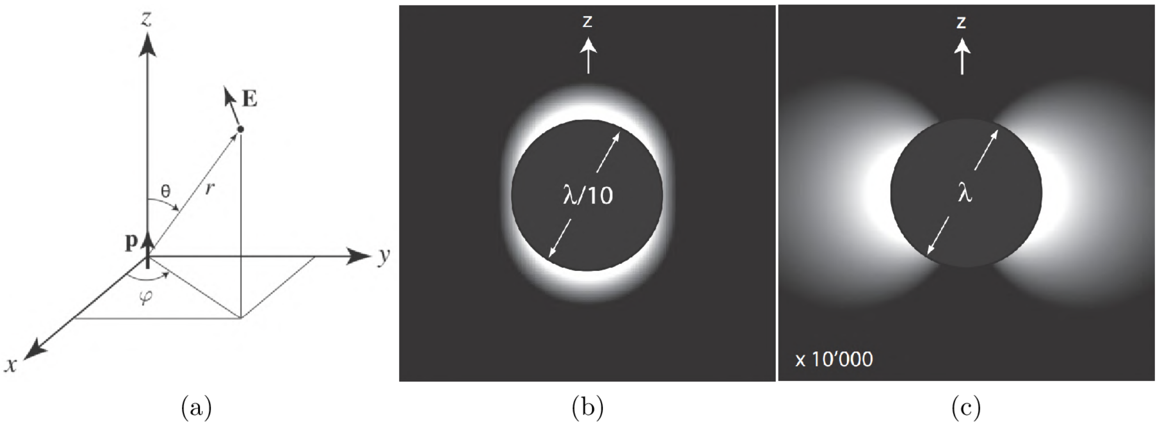

(a) (b) (c)

Figure 4.2: (a) Spherical coordinate system (θ, φ, z) for describing the radiation pattern of an elementary dipole. Directions of the vectors of electric intensity **E** and dipole moment **p** are indicated. (b) Near-field radiation outside an imaginary spherical surface with the diameter of $\lambda/10$ centered on the dipole. Lighter colors represent greater radiation intensity at the given location. In this picture, it can be seen that the near-field radiation is mostly in the z-direction, i.e., the direction of dipole oscillations. (c) Far-field radiation outside an imaginary spherical surface with the diameter of λ centered on the dipole. This radiation is purely transverse and has zero contribution in the direction of dipole oscillations (z-axis). Note that the intensity in part (c) was magnified $10,000\times$ to use the same grayscale map as in part (b). These pictures were taken from [16].

the other hand, in lateral binding, the incident light field propagates in the orthogonal direction to the direction of the binding process [49]. Both cases are schematically shown in Fig. 4.3.

Let us consider the lateral optical binding of two optically trapped Rayleigh particles (dipoles) A and B located at positions $\mathbf{r}_A, \mathbf{r}_B$ in independent coherent trapping beams. This geometry can be seen in Fig. 4.4 and will be considered during the whole binding chapter and experimental parts connected to two particles. Both particles are electrically charged but do not have a permanent electric dipole moment. Induced electric dipole moments of the particles are created upon illumination with the incident trapping beams, which polarizes both particles in phase with the incoming light [49, 50, 51]. The components of the induced electric dipole moments for symmetrically spherical particles can be expressed as $p_i(\mathbf{r}_A) = \alpha^A E_i(\mathbf{r}_A)$ and $p_i(\mathbf{r}_B) = \alpha^B E_i(\mathbf{r}_B)$, where $E_i(\mathbf{r}_A)$ and $E_i(\mathbf{r}_B)$ are the components of the net electric fields at the positions of particles A and B, $\alpha^{A(B)}$ are the polarizabilities of the spherical particles A (B). The net electric field that will act on one of the particles will be the sum of the coherently radiated light scattered from the other particle and the unperturbed incident laser beam $\mathbf{E}^I(\mathbf{r})$. In the component notation, this can be mathematically expressed as [49]

$$E_i(\mathbf{r}_A) = E_i^I(\mathbf{r}_A) + G_{ij}(\mathbf{r}_A, \mathbf{r}_B)\alpha^B E_j(\mathbf{r}_B), \tag{4.11}$$

$$E_i(\mathbf{r}_B) = E_i^I(\mathbf{r}_B) + G_{ij}(\mathbf{r}_B, \mathbf{r}_A)\alpha^A E_j(\mathbf{r}_A), \tag{4.12}$$

where $E_i^I(\mathbf{r}_A), E_i^I(\mathbf{r}_B)$ are the components of the unperturbed electric fields of the incident beam at the particle positions $\mathbf{r}_A, \mathbf{r}_B$, the Einstein summation convention was applied (i.e., the summation sign Σ was omitted when the same index appears twice in the formula)

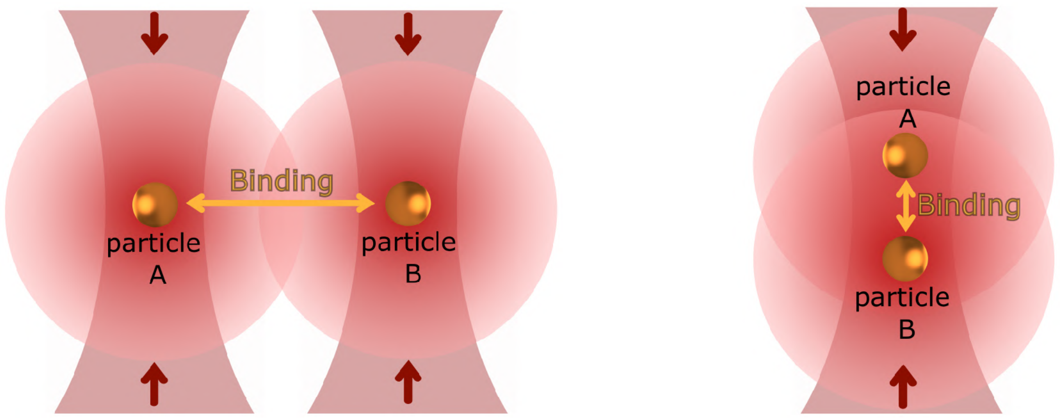

(a) (b)

Figure 4.3: Two basic geometries for the observation of optical binding interaction in counter-propagating laser beams. Yellow arrows show the direction of the binding interaction and red arrows show the light propagation direction for each beam. (a) Lateral optical binding scheme – the incident light propagates in the orthogonal direction to the direction of the binding process between particles A and B. This geometry can also be observed in a single broad beam. (b) The longitudinal optical binding scheme – the incident light propagates in the same direction as is the direction of the binding process. Both particles are now trapped in one pair of counter-propagating laser beams. In case particles are not precisely next to or above each other, the binding interaction becomes a more complex superposition of lateral and longitudinal interaction.

and G_{ij} are the components of the field propagator (dyadic Green's function) between the two dipolar particles

$$G_{mn} = \frac{\exp(\mathrm{i}kR)}{4\pi\epsilon_0\epsilon_1 R^3}\left[(3 - 3\mathrm{i}kR - k^2R^2)\frac{R_m R_n}{R^2} + (k^2R^2 + \mathrm{i}kR - 1)\delta_{mn}\right], \tag{4.13}$$

where $R \equiv |\mathbf{R}| = |\mathbf{r}_B - \mathbf{r}_A|$, ϵ_1 is the relative permittivity of the surrounding medium, and δ_{mn} is the Kronecker delta. In Eq. (4.13), we can again observe 3 terms: near, intermediate, and far fields. In the case of optical binding of optically trapped particles, the far field will have the greatest influence.

Considering that the particles are much smaller than the light wavelength, the total optical force acting on spherical particle B along the coordinate $\xi \in \{x, y, z\}$ can in general be written in the following form [49]

$$F^B_{\mathrm{opt},\xi} = \frac{1}{2}\mathrm{Re}\{\alpha^{B*}E_i^{IB*}\partial_\xi^B E_i^{IB} + \alpha^{B*}G^*_{ij}\alpha^{A*}E_j^{IA*}\partial_\xi^B E_i^{IB} + \alpha^{B*}E_j^{IB*}\partial_\xi^B(G_{jk})\alpha^A E_k^{IA}\}, \tag{4.14}$$

where E_i^{IA}, E_i^{IB} are the x, y, z components of the unperturbed incident electric fields at the locations of particles A and B and ∂_ξ^B denotes the partial derivative of the immediately following quantity with respect to the coordinate ξ, evaluated at the location of particle B. The first term in Eq. (4.14) is the optical force acting on the isolated dipole B without the presence of the dipole A. The second term in Eq. (4.14) corresponds to the interaction between the unperturbed incident field and the part of the dipole B induced by the field scattered from the dipole A located at $\mathbf{r}_A$. The last term in Eq. (4.14) is then the interaction between the part of the dipole B induced by the incident field and the

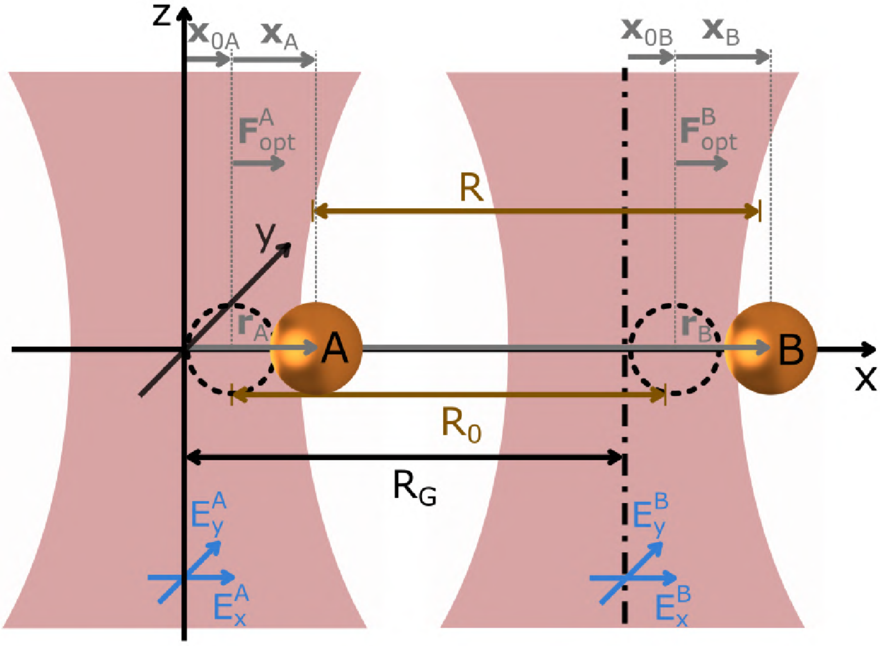

Figure 4.4: Schema of used geometry of two parallel counter-propagating laser beams for experiments with two particles. The z-axis is located at the center of the first volume and x- and y-axis are perpendicular to it. The center of the second beam is marked with a dashed line. The particle (orange circle) oscillates around the equilibrium position (black dashed circle) and is displaced from it by the distance $\mathbf{x}_{A(B)}$ for particle $A(B)$. The gray arrows show the optical forces $F^{A(B)}_{\text{opt}}$ that act on the particles A and B. Blue arrows denote the direction of the intensity of the electric field along the x- and y-axis. The distance R corresponds to the instantaneous distance of particles, the distance R_0 is the distance of the equilibrium positions around which the particle oscillates and R_G is the distance between the beam axes. As can be seen in the figure, the equilibrium positions of particles A and B in the case of binding interaction between them are not on the axis of the beams, but they are slightly deviated from it. Neglecting the binding interaction between both particles, the equilibrium positions will be placed at the beam axis. The $r_{A(B)}$ denotes the position vectors of particle $A(B)$

field scattered from the dipole A placed at $\mathbf{r}_A$. The second and third terms together form the so-called *optical binding force* responsible for coupling between the dipoles A and B mediated by light scattering [49].

In the case of the used lateral geometry (Fig. 4.4), only far-field terms in Eq. (4.14) are considered. Linearly polarized beams have generally x and y components of the electric field $\mathbf{E}^{A(B)} = (E^{A(B)}_x, E^{A(B)}_y)$. It also turned out during calculations that the third term (with a derivative of G_{jk}) in Eq. (4.14) was one order of magnitude smaller than the second one. Under these conditions, optical binding forces acting on dipole A and B have the following form

$$F^A_{\text{bind}}(r_A) = \frac{E^A_y(r_A)E^B_y(r_B)\alpha^A\alpha^B k^3 \sin(\Phi^B - \Phi^A + kR)}{8\pi\varepsilon_1 R}, \tag{4.15}$$

$$F^B_{\text{bind}}(r_B) = \frac{E^A_y(r_A)E^B_y(r_B)\alpha^A\alpha^B k^3 \sin(\Phi^B - \Phi^A - kR)}{8\pi\varepsilon_1 R}. \tag{4.16}$$

Equations can be linearized for small deviations of the particle positions x_A, x_B from the equilibrium positions x_{0A}, x_{0B} giving small deviation $x = x_B - x_A$ of the inter-particle distance $R = R_0 + x$. Using the Taylor series and neglecting terms with x^2/R_0^2 and higher the following linearized equations for the optical binding forces acting on each particle can be obtained

$$F^A_{\text{bind}}(r_A) = \frac{E^A_y(r_A)E^B_y(r_B)\alpha^A\alpha^B k^3}{8\pi\varepsilon_1 R_0}\left[\sin(\Delta\Phi + kR_0) + kx\cos(\Delta\Phi + kR_0)\right], \quad (4.17)$$

$$F^B_{\text{bind}}(r_B) = \frac{E^A_y(r_A)E^B_y(r_B)\alpha^A\alpha^B k^3}{8\pi\varepsilon_1 R_0}\left[\sin(\Delta\Phi - kR_0) - kx\cos(\Delta\Phi - kR_0)\right], \quad (4.18)$$

where $\Delta\Phi = \Phi^B - \Phi^A$. The first terms in square brackets are responsible for the new equilibrium positions of the particle, that are shifted from the beam center if the optical binding force is active. To derive the linearized equations of motions of the particles around such new equilibrium positions, only the second terms play the role. Expanding the sine and cosine terms the following expressions for the binding forces can be obtained

$$\begin{aligned} F^A_{\text{bind2}}(r_A) &= \frac{E^A_y(r_A)E^B_y(r_B)\alpha^A\alpha^B k^3}{8\pi\varepsilon_1 R_0}\left[\cos(\Delta\Phi)\cos(kR_0) - kx\sin(\Delta\Phi)\sin(kR_0)\right] && (4.19)\\ &= k_1(x_B - x_A) + k_2(x_B - x_A), && (4.20)\\ F^B_{\text{bind2}}(r_B) &= \frac{-E^A_y(r_A)E^B_y(r_B)\alpha^A\alpha^B k^3}{8\pi\varepsilon_1 R_0}\left[\cos(\Delta\Phi)\cos(kR_0) + kx\sin(\Delta\Phi)\sin(kR_0)\right], && (4.21)\\ &= -k_1(x_B - x_A) + k_2(x_B - x_A). && (4.22) \end{aligned}$$

The spring constant k_1 is associated with the reciprocal part of the binding force because it acts in opposite directions on particles A and B. On the other hand, the spring constant k_2 describes a non-reciprocal part of the binding force because it acts in the same direction on both particles. Reciprocal forces can be understood as internal forces of the system, which do not affect the motion of the system's center of mass. In contrast, non-reciprocal forces influence the motion of the center of mass of the system. According to Eq. (4.19), the dominant type of interaction, i.e., reciprocal or non-reciprocal, can be adjusted by changing the mean trap distance R_0 or the phase difference $\Delta\Phi$.

In an analogy to the equations of motion (4.1) and (4.2) of two linearly coupled harmonic oscillators presented in Section 4.1.1, linearized expressions for the optical binding forces can be used to formulate the coupled equations of motion for the system of optically bound particles confined in harmonic optical traps. In this system, the coupling stiffness κ physically represents the reciprocal and non-reciprocal binding forces. Specifically, κ can be expressed as the sum or the difference of the spring constants k_1 and k_2 given by Eq. (4.19): $\kappa = k_1 \pm k_2$. Compared to Eqs. (4.1) and (4.2), damping of the particle motion will be included in the equations of motion that have the form [51]

$$\begin{aligned} m\ddot{x}_A + \gamma\dot{x}_A &= -(m\Omega_A^2 + k_1 + k_2)x_A + (k_1 + k_2)x_B, && (4.23)\\ m\ddot{x}_B + \gamma\dot{x}_B &= -(m\Omega_B^2 + k_1 - k_2)x_B + (k_1 - k_2)x_A, && (4.24) \end{aligned}$$

where m is the mass of each particle (both particles are taken to be the same), γ is the viscous drag coefficient, and $\Omega_{A(B)} = \sqrt{k_{A(B)}/m}$ are the mechanical eigenfrequencies of each trap.

Equations of motion (4.23) and (4.24) can be solved in a similar way as discussed in Section 4.1.1 for two coupled harmonic oscillators and we get the eigenfrequencies of the normal modes in the form [51]

$$\Omega_{\pm} \approx \Omega + g \mp \sqrt{g^2 - \overline{g}^2}, \tag{4.25}$$

where Ω is the mechanical eigenfrequency in the case of no interaction between the particles confined in identical optical traps ($k_A = k_B$ giving identical mechanical eigenfrequencies $\Omega = \Omega_A = \Omega_B$), g is the reciprocal coupling rate ($g = k_1/(2m\Omega)$), and $\overline{g}$ is the non-reciprocal coupling rate ($\overline{g} = k_2/(2m\Omega)$). According to the established convention for normal modes, Ω_+ is the center of mass mode and Ω_- is the breathing mode.

4.1.4. Coulomb interaction

Since the trapped particles are generally charged, the electric coupling will also form between them due to the Coulomb interaction, in addition to the optical binding. The magnitude of electrostatic Coulomb force F_{Coulomb} between the particles has the form

$$F_{\text{Coulomb}} = \frac{1}{4\pi\epsilon_0\epsilon_1}\frac{q_A q_B}{R_0^2}, \tag{4.26}$$

where R_0 is the separation distance between the particles, $q_{A(B)}$ are the charges of particle $A(B)$, ϵ_0 is the vacuum permittivity, and ϵ_1 is the relative permittivity of the medium around particles.

The Coulomb force is proportional to R_0^{-2}, and therefore decreases faster than the optical binding force with increasing inter-particle distance R_0. For larger inter-particle distances, corresponding to the far field of the dipole radiation, the Coulomb interaction is typically an order of magnitude smaller than the optical one for typical magnitudes of electric charges (100 e) of the particles. Therefore, the Coulomb interaction can be neglected in the interpretation of our experiments reported in this thesis.

4.1.5. Cooling of normal modes of two particles

In this subsection, the cooling of normal modes of two laterally bound particles confined in separate optical traps (see Fig. 4.3(a) for illustration) will be described based on reference [52]. This case is conceptually similar to the 2D cold damping of a single trapped particle but slightly more challenging. The theoretical treatment will be based on an analogy to the equation of motion (3.18) for 2D cold damping; however, instead of considering the 2D position of a single trapped particle, the position vector $\mathbf{r} = \begin{bmatrix} x_1 \\ x_2 \end{bmatrix}$ will represent the x-coordinates of the two particles confined in separate optical traps. Since the two particles can be generally different, the mass of the system will be described by the matrix $\mathbf{M}$. Thus, the system will be described by the following matrices

$$\mathbf{M} = \begin{bmatrix} m_1 & 0 \\ 0 & m_2 \end{bmatrix}, \tag{4.27}$$

$$\mathbf{K} = \begin{bmatrix} K_1 & b \\ b & K_2 \end{bmatrix}, \tag{4.28}$$

$$\mathbf{Z} \approx \begin{bmatrix} \xi_1 & -\frac{\xi_1\xi_2}{8\pi\mu R_0} \\ -\frac{\xi_1\xi_2}{8\pi\mu R_0} & \xi_2 \end{bmatrix}, \tag{4.29}$$

where $m_{1(2)}$ are the masses of the two particles, $K_{1(2)}$ are the stiffnesses of the corresponding optical traps, b is the stiffness of binding between the two particles, $\xi_{1(2)}$ are the viscous damping coefficients of the two particles given by the Stoke's law (the same as in Section 2.2.1), R_0 is the separation between the equilibrium positions of the two particles, and μ is the dynamic viscosity of the fluid (ambient atmosphere).

When considering the coupling of two particles located in two parallel optical traps, it is most convenient to express the equations of motion in a modal basis. For a perfectly symmetric system with the mentioned geometry, it is possible to decompose the system into a pair of normal modes that can be defined as

$$a_\Sigma(t) = \frac{x_1(t) + x_2(t)}{2}, \tag{4.30}$$

$$a_\Delta(t) = \frac{x_1(t) - x_2(t)}{2}, \tag{4.31}$$

where $a_\Sigma(t)$ is the amplitude of the center of mass mode (CoM mode) and $a_\Delta(t)$ is the amplitude of the breathing mode (Br mode). Despite the fact that our system is not fully symmetrical (the radius of the particles can vary slightly, they do not have to be perfect spheres, etc.), we will further describe the system in the modal basis consisting of these two normal modes.

The electric field magnitude responsible for the feedback loop force of the cold damping will now have the following form

$$E = g(c_\Sigma \dot{a}_\Sigma + c_\Delta \dot{a}_\Delta), \tag{4.32}$$

where g is the scalar gain, c_Σ is the weight coefficient for the CoM mode, and c_Δ is the weight coefficient for the Br mode.

Neglecting the measurement noise, the equation of motion in the normal mode basis will be

$$\mathbf{M}\ddot{\mathbf{a}}(t) = -\mathbf{Z}\dot{\mathbf{a}}(t) - \mathbf{K}\mathbf{a}(t) - \mathbf{G}\dot{\mathbf{a}}(t-\tau) + \mathbf{F}_{\text{th}}, \tag{4.33}$$

In the modal basis, the individual matrices will have the following forms

$$\mathbf{M} = \begin{bmatrix} M & m \\ m & M \end{bmatrix}, \tag{4.34}$$

$$\mathbf{K} = \frac{1}{2}\begin{bmatrix} K_1 + K_2 + 2b & K_1 - K_2 \\ K_1 - K_2 & K_1 + K_2 - 2b \end{bmatrix} \equiv \begin{bmatrix} K_\Sigma & K_X \\ K_X & K_\Delta \end{bmatrix}, \tag{4.35}$$

$$\mathbf{Z} \approx \frac{1}{2}\begin{bmatrix} \xi_1 + \xi_2 - \frac{\xi_1\xi_2}{4\pi\mu R_0} & \xi_1 - \xi_2 \\ \xi_1 - \xi_2 & \xi_1 + \xi_2 + \frac{\xi_1\xi_2}{4\pi\mu R_0} \end{bmatrix} \equiv \begin{bmatrix} \xi_\Sigma & \xi_X \\ \xi_X & \xi_\Delta \end{bmatrix}, \tag{4.36}$$

$$\mathbf{G} = g\begin{bmatrix} c_\Sigma q_\Sigma & c_\Delta q_\Sigma \\ c_\Sigma q_\Delta & c_\Delta q_\Delta \end{bmatrix}, \tag{4.37}$$

where $m = (m_1 - m_2)/2$, $M = (m_1 + m_2)/2$, $K_{\Sigma(\Delta)}$ are the effective stiffness coefficients for both modes, K_X is a coupling term that is non-zero if $K_1 \neq K_2$, $\xi_{\Sigma(\Delta)}$ are the viscous damping coefficients for both modes, ξ_X is weak coupling (if $\xi_1 \neq \xi_2$), $q_\Sigma = (q_1 + q_2)/2$ is the average charge for the CoM mode, and $q_\Delta = (q_1 - q_2)/2$ is the charge difference for the Br mode.

To find the form of the PSD for both modes, Eq. (4.33) must be expressed in the frequency domain

$$-\omega^2\mathbf{M}\mathbf{A}(\omega) = -\mathrm{i}\omega\mathbf{Z}\mathbf{A}(\omega) - \mathbf{K}\mathbf{A}(\omega) - \mathrm{i}\omega\mathrm{e}^{-\mathrm{i}\omega\tau}\mathbf{G}\mathbf{A}(\omega) + \hat{\mathbf{F}}_{\mathrm{th}}, \tag{4.38}$$

where $\mathbf{A}$ is the vector of modal amplitudes in the frequency domain. After rearranging Eq. (4.38), it is possible to express the modal amplitudes in the following form

$$\mathbf{A}(\omega) = \left(\omega^2\mathbf{M} - \mathrm{i}\omega\mathbf{Z} - \mathbf{K} - \mathrm{i}\omega\mathrm{e}^{-i\omega\tau}\mathbf{G}\right)^{-1}(-\hat{\mathbf{F}}_{\mathrm{th}}) \equiv \mathbf{D}(-\hat{\mathbf{F}}_{\mathrm{th}}). \tag{4.39}$$

Using the definitions of individual matrices $\mathbf{M}, \mathbf{Z}, \mathbf{K}, \mathbf{G}$, matrix $\mathbf{D}$ can be obtained in the form

$$\mathbf{D} = \frac{1}{P_{\Sigma\Sigma}P_{\Delta\Delta} - P_{\Sigma\Delta}P_{\Delta\Sigma}}\begin{bmatrix} P_{\Delta\Delta} & -P_{\Sigma\Delta} \\ -P_{\Delta\Sigma} & P_{\Sigma\Sigma} \end{bmatrix}, \tag{4.40}$$

where

$$\begin{aligned}
P_{\Sigma\Sigma}(\omega) &= M\omega^2 - \mathrm{i}\omega(\xi_\Sigma + G_{11}\mathrm{e}^{-\mathrm{i}\omega\tau}) - K_\Sigma, && (4.41)\\
P_{\Delta\Delta}(\omega) &= M\omega^2 - \mathrm{i}\omega(\xi_\Delta + G_{22}\mathrm{e}^{-\mathrm{i}\omega\tau}) - K_\Delta, && (4.42)\\
P_{\Sigma\Delta}(\omega) &= m\omega^2 - \mathrm{i}\omega(\xi_X + G_{12}\mathrm{e}^{-\mathrm{i}\omega\tau}) - K_X, && (4.43)\\
P_{\Delta\Sigma}(\omega) &= m\omega^2 - \mathrm{i}\omega(\xi_X + G_{21}\mathrm{e}^{-\mathrm{i}\omega\tau}) - K_X. && (4.44)
\end{aligned}$$

For further calculations, only a perfectly symmetric system will be considered for simplification. This means that it holds $K_X = \xi_X = m = 0$. However, it is still allowed to have different charges for both particles. For the perfectly symmetric system, the matrix $\mathbf{D}$ will have following form

$$\mathbf{D} = \frac{1}{P_{\Sigma\Sigma}P_{\Delta\Delta} + \omega^2 G_{12}G_{21}\mathrm{e}^{-2\mathrm{i}\omega\tau}}\begin{bmatrix} P_{\Delta\Delta} & \mathrm{i}\omega G_{12}\mathrm{e}^{-\mathrm{i}\omega\tau} \\ \mathrm{i}\omega G_{21}\mathrm{e}^{-\mathrm{i}\omega\tau} & P_{\Sigma\Sigma} \end{bmatrix}. \tag{4.45}$$

The final PSD for the perfectly symmetric system will then be in the following form

$$\begin{aligned}
\mathbf{S} = \lim_{T_{\mathrm{m}}\to\infty}\frac{1}{T_{\mathrm{m}}}\mathbf{A}(\omega)\mathbf{A}^{T*}(\omega) &= \frac{S_{F_{\mathrm{th}}}}{|P_{\Sigma\Sigma}P_{\Delta\Delta} + \omega^2 G_{12}G_{21}\mathrm{e}^{-2\mathrm{i}\omega\tau}|^2} \\
\times \begin{bmatrix} |P_{\Delta\Delta}|^2 + \omega^2 G_{12}^2 + S_\Sigma^{\mathrm{fb}}(S_{\mathrm{nn}}) + S_{\mathrm{nn}} & \mathrm{i}\omega(G_{12}P_{\Sigma\Sigma}^*\mathrm{e}^{-\mathrm{i}\omega\tau} - G_{21}P_{\Delta\Delta}\mathrm{e}^{\mathrm{i}\omega\tau}) \\ \mathrm{i}\omega(G_{21}P_{\Delta\Delta}^*\mathrm{e}^{-\mathrm{i}\omega\tau} - G_{12}P_{\Sigma\Sigma}\mathrm{e}^{\mathrm{i}\omega\tau}) & |P_{\Sigma\Sigma}|^2 + \omega^2 G_{21}^2 + S_\Delta^{\mathrm{fb}}(S_{\mathrm{nn}}) + S_{\mathrm{nn}} \end{bmatrix}&,
\end{aligned} \tag{4.46}$$

where $S^{fb}_{\Sigma(\Delta)}(S_{nn})$ are the contributions from the noise-induced heating in the form

$$S_\Sigma^{\mathrm{fb}}(S_{\mathrm{nn}}) = \left(\frac{|P_{\Delta\Delta}|^2 + 2r\omega G_{12}\Im(P_{\Delta\Delta}\mathrm{e}^{\mathrm{i}\omega\tau}) + r^2\omega^2 G_{12}^2}{|P_{\Delta\Delta}P_{\Sigma\Sigma} + \omega^2 G_{12}G_{21}\mathrm{e}^{-2\mathrm{i}\omega\tau}|^2}\right)\omega^2 g'^2 S_{\mathrm{nn}}, \tag{4.47}$$

$$S_\Delta^{\mathrm{fb}}(S_{\mathrm{nn}}) = \left(\frac{r^2|P_{\Sigma\Sigma}|^2 + 2r\omega G_{21}\Im(P_{\Sigma\Sigma}\mathrm{e}^{\mathrm{i}\omega\tau}) + \omega^2 G_{21}^2}{|P_{\Delta\Delta}P_{\Sigma\Sigma} + \omega^2 G_{12}G_{21}\mathrm{e}^{-2\mathrm{i}\omega\tau}|^2}\right)\omega^2 g'^2 S_{\mathrm{nn}}, \tag{4.48}$$

where $g' = gq_\Sigma$ is the effective scalar gain, $\Im(X)$ denotes imaginary part of X and $r = q_\Delta/q_\Sigma$ is the charge ratio. In the case of cooling just one of the modes a_Σ or a_Δ, the corresponding modal coefficient c_Σ or c_Δ is set to 1 and the coefficient for the uncooled mode is set to 0. Since Eq. (4.46) was also used for fitting experimental data connected to the experiments with cooling of optically bound particles, in which there are also measurement noise (S_{nn}) and feedback noise ($S^{\mathrm{fb}}_{\Sigma,\Delta}$), these noises are also included in the resulting equations as additional independent terms of PSD. It can also be noticed in the equation that the mentioned noises are added only to the diagonal terms xx and yy, i.e. to the x and y axes separately in which the actual cooling measurements were made.

4.2. Cold damping experiments with two particles

In this section, the details of the experimental set-up for two-particle experiments will be described, with a focus on the detection part and the feedback loop. It will be explained how to properly align the detection path for two particles to minimize crosstalks between the transverse axes x and y for a single particle and also eliminate the influence of the second particle. Subsequently, the experiments with two trapped particles will be presented and the procedures for data evaluation will be described along with the corresponding theoretical models.

4.2.1. Experimental set-up for two optically bound particles

The schema of the experimental set-up for cold damping of the motion of two optically bound particles is shown in Fig. 4.5. Using the DMD, two independent dual-beam optical traps were created in the vacuum chamber (VCH). The trapping part was already described in Section 2.3.1; here, I will pay more attention to the detection part of the system.

To detect simultaneously the positions of two levitated particles, the polarization of the trapping beams propagating from the bottom to the top in Fig. 4.5 was rotated by $\sim 5°$ degrees using the half-wave plate placed in front of the VCH. Due to this small polarization misalignment, a part of the trapping beams could be reflected toward detectors by the polarized beam splitter PBS$_2$. Since two particles are confined in independent traps, two detection laser beams propagating side-by-side (one for each particle) have to be routed to two separate detectors QPD$_1$ and QPD$_2$. Such separation of the detection beams was achieved using a D-shaped mirror, which allowed the beam for one particle to pass towards QPD$_1$, whereas the other beam was reflected towards QPD$_2$. The first detection beam was transformed by the telescope L$_{12}$ and L$_{13}$ and the second detection beam was transformed by the telescope L$_{12}$ and L$_{14}$. These two telescopes changed the diameter of the beams to the desired value to fill the apertures of the respective detectors QPD$_1$ and QPD$_2$.

Both sets of QPD signals were then independently read out using an NI USB card and used for the data acquisition and processing. The second NI FPGA card processed the feedback for cold damping of both normal modes. An amplifier A was connected to the output of the FPGA card and amplified the signal 15 times. The amplified signal was then brought to one electrode in the VCH, while the second electrode was grounded. The acquisition and amplification of the individual signals were controlled using a PC. Using this arrangement, we had full control over the magnitude of the applied voltage controlling the motion of both optically bound particles via the CD process.

4.2.2. Feedback loop for cold damping of optically bound particles

The algorithm of the feedback loop for cold damping of the motion of two optically bound particles was analogical to the 2D CD described in Section 3.5.3. Here, however, two independent optical traps with circular Gaussian profiles of optical intensity were created using the DMD. The position signals were then collected from the corresponding QPDs (see Section 4.2.1), however only the signal corresponding to the axis oriented along the

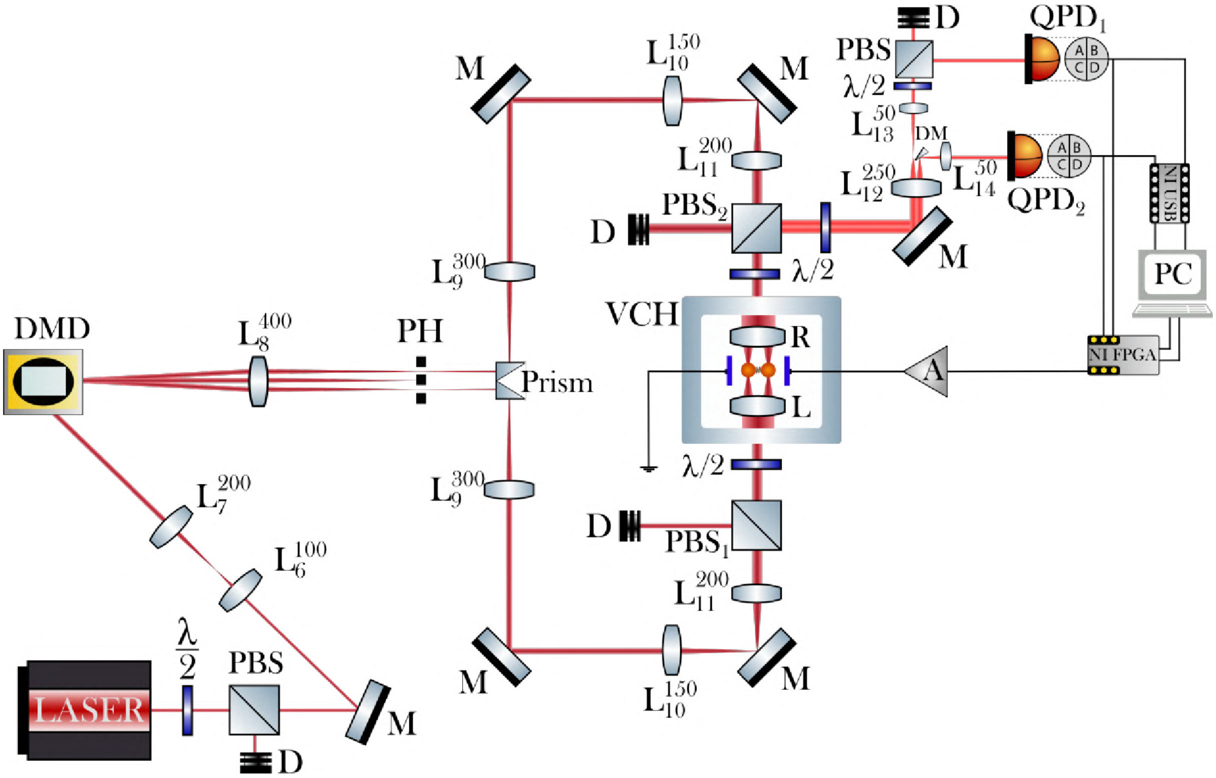

Figure 4.5: Schema of the experimental set-up for cold damping experiments with two optically bound particles. The abbreviation DM indicates a D-shaped mirror that serves for the separation of the two detection beams, the other used abbreviations were previously defined in Fig. 2.7.

line (x-axis) connecting the particles was used for the CD feedback. Instead of cooling the individual displacements x_1 and x_2 of the two particles, we directly cooled the normal modes of the particles' oscillation. Specifically, signals x_1 and x_2 from the two QPDs were added to each other to obtain the coordinate of the Center-of-mass (CoM, Σ) normal mode x_Σ and subtracted from each other to obtain the coordinate of the Breathing (Br, Δ) normal mode x_Δ. Motional modes of individual particles are schematically shown in Fig. 4.6. The particles move in the same direction in the CoM mode, and in the opposite direction in the Br mode.

The overall detection hardware and signal processing in the FPGA card are the same as in Section 3.5.2, except here two QPDs are used. As we illustrate in Fig. 4.7, the signals x_Σ and x_Δ passed through the low-pass filter (suppressing noise above 300 kHz), differentiated to get velocities and multiplied by independent gains $\times c_c$ and $\times c_b$ corresponding to the individual modes. Parameter $\times g$ adjusted the overall feedback voltage and consequently the gain of the feedback loop.

(a) (b)

Figure 4.6: Normal modes of oscillation of two optically bound particles. (a) Center of mass mode x_Σ. (b) Breathing mode x_Δ.

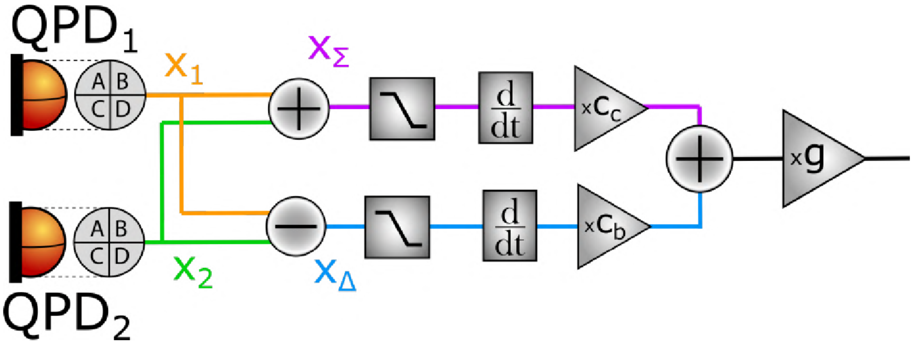

Figure 4.7: Signal processing in FPGA board for the feedback loop of cold damping of normal modes of two optically bound particles.

4.2.3. Alignment of the detection path for two particles

After successful stable confinement of two particles in independent optical traps, described in Section 2.5.3, and evacuation of the vacuum chamber to the required pressure of 1 mbar, it was necessary to align both detection paths to minimize crosstalks between different axes and trapping paths to maximize the frequencies of the particles' oscillation.

Both QPD detectors were centered on the corresponding detection beams, using the same procedure as described in Section 3.5.4 for the single-particle case. Subsequently, the crosstalks between the x- and y-axes of individual particles were minimized by very slight rotation of the corresponding QPDs. The crosstalks between the CoM and Br modes along the x-axis were suppressed by rotating the half-wave plate placed in front of QPD$_1$ (see Fig. 4.5). Furthermore, the magnitudes of the position signal corresponding to x_1 and x_2 were put to the same level by adjusting gains by coefficients c_c and c_b (see Fig. 4.7). During the alignment process, the crosstalks were observed in real-time using the PSDs of the axes of interest calculated by the LabView program running in the control PC.

In the end, the frequencies of particles' oscillations were maximized by adjusting the mirrors in the trapping beam paths (located between the prism creating the two independent trapping paths and the vacuum chamber) along the x-axis.

4.2.4. Experimental protocol for two particles

After stable trapping of two particles (see Section 2.5.3) and the correct setting of both detection paths (see Section 4.2.3), the trapped particles were driven by an external electric field generated by an AC voltage from a signal generator. A sinusoidal voltage was applied to the electrodes and the response of the particles' was investigated to verify that both particles were electrically charged. Afterward, the feedback loop was turned on and the charge polarity was tested to ensure the proper setting of the feedback gains c_c and c_b to achieve a similar cooling rate (not heating) of both particles. Subsequently, I tried several different feedback loop gains for both normal modes and approximately mapped the region where the cooling of the normal modes occurred and the particles were not lost. After that, I applied feedback voltages with different gains to the electrodes and gradually recorded the resulting positional trajectory of both particles, using simultaneously the QPDs and the camera for the proper calibration of the QPD signals. Typically, I recorded 200 000 positions in 1 second-long recording.

4.2.5. Data evaluation of two particles

In order to calibrate the QPD position traces, a high-speed camera was implemented in the experimental setup and a record of the particles' motion in $x-z$ plane was saved. Each frame of the video record was processed using a Gaussian filter, which removed noise from the image, and then the background was subtracted from the images. This removal of unwanted image features increased the accuracy of locating the particle in the image following the procedure of [53].

All the data related to the cold damping experiments with two optically bound particles were processed by my colleague Mgr. Oto Brzobohatý, Ph.D. using the Julia programming language. I subsequently took over the calibrated and fitted experimental data and further processed them in Python into the final graphs presented in this thesis. After recording the QPD position traces, performing their calibration using a high-speed camera (see Section 2.6.2) normal modes of oscillation were calculated from the measured data using Eq. (4.31) and recorded.

To find out other system parameters, the PSD was calculated and fitted with the theoretical equation Eq. (4.46). As all the parameters had different orders of magnitude, they were first rescaled to similar numerical values, so that the fitting of the model to the experimental data was more robust. First, oscillation eigenfrequency and viscous damping rate due to the ambient atmosphere were determined by fitting the data recorded without cooling (zero gain of the feedback loop). In the subsequent analysis of the data obtained from cooled particles, these parameters were kept constant, because the electric field applied to the particles to induce cold damping had no effect on them. The peak amplitude (term $2k_\mathrm{B}T\xi_0$), background noise and the parameter c appearing in the matrix G were determined by fitting the position PSDs of cooled trajectories obtained for varied settings of the feedback loop gain. The value of the feedback loop delay τ was determined by an independent measurement using an oscilloscope to be 5.6 µs, as in the case of a single particle. The fitting procedure was always carried out independently for each mode.

The effective kinetic temperatures of the CoM and Br modes, which characterize the motion of the trapped particles and the rate of their cooling, were calculated for the individual measurements from the equipartition theorem for velocity as

$$T_{\mathrm{kin,eff},\Sigma/\Delta} = \frac{2\langle E^{\mathrm{kin}}_{\Sigma/\Delta}\rangle}{k_\mathrm{B}} = \frac{m\langle \dot{a}^2_{\Sigma/\Delta}\rangle}{k_\mathrm{B}} \tag{4.49}$$

where $a_{\Sigma/\Delta}$ are the coordinates of the CoM and Br modes, respectively.

4.3. Cooling of normal modes of two particles via cold damping – results

In this section, the results of the cooling of normal modes for two particles via the cold damping will be presented at the ambient pressure of 1 mbar. In this geometry, the beam had a circular shape as in Section 3.6, but there were two particles confined in two parallel optical traps. This case can also be considered roughly analogous to the case in Section 3.7 for one particle – cooling of two axes for one particle vs cooling of x axes of two particles, i.e. normal modes after their coupling. As described in the theoretical Section 4, when the particles are sufficiently close, their oscillations can be decomposed into a superposition of two normal modes – CoM mode and Br mode. So, first of all the data for cooling of one of the normal modes will be presented, i.e. cooling just CoM mode (see Subsection 4.3.1) or cooling just Br mode (see Subsection 4.3.2) and at the end simultaneous cooling of both modes will be described (see Subsection 4.3.3).

4.3.1. Cooling of the center of mass mode only

In this case, I set the cooling coefficient for Br mode equal to zero ($c_\Delta = 0$). In Fig. 4.8 the PSDs of both modes are shown. In all graphs in this section, the red color corresponds to the CoM mode and the blue color corresponds to the Br mode. A significant decrease and broadening of the PSD peak can be observed for the cooled CoM mode, while the uncooled Br mode has an approximately constant value. When increasing the gain, however, there is an increase in crosstalk into the Br mode, which was not present at zero gain. The small peak on the far left then corresponds to the crosstalk from the z-axis. When the gain is increased, both peaks shift to the right due to the feedback loop delay τ. In Fig. 4.9 the decrease in an effective kinetic temperature for both modes is shown. An effective kinetic temperature of 58.4 K for CoM mode was reached for the gain = 1000, whereas the effective kinetic temperature of Br mode oscillated around the actual ambient temperature for all gain settings. The final resonance frequencies and damping rates for both were $\omega_\Sigma/2\pi = 2.5 \cdot 10^4\,\mathrm{Hz}$ for CoM mode, $\omega_\Delta/2\pi = 3.0 \cdot 10^4\,\mathrm{Hz}$ for Br mode, $\xi_\Sigma/2\pi = 2.0 \cdot 10^2\,\mathrm{Hz}$ for CoM mode and $\xi_\Delta/2\pi = 2.1 \cdot 10^2\,\mathrm{Hz}$.

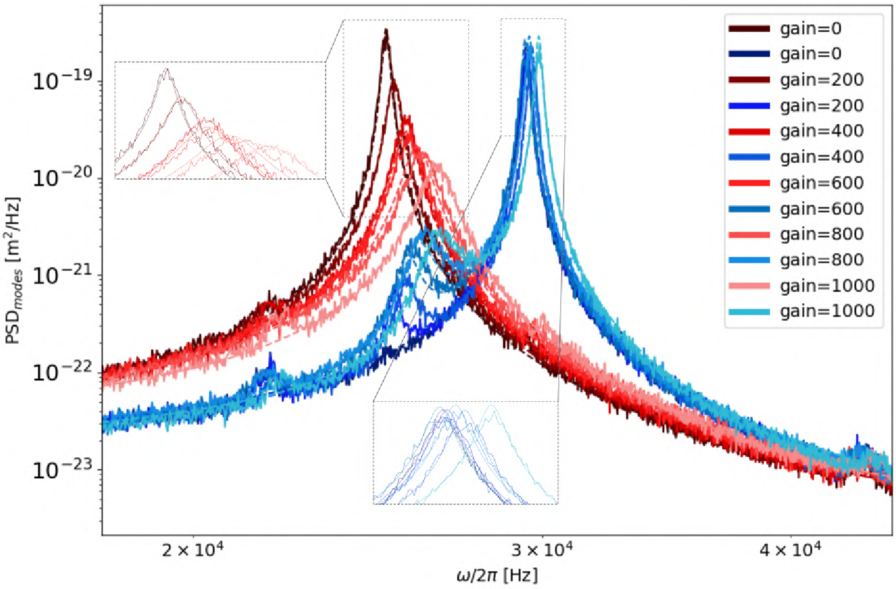

Figure 4.8: Calculated PSD of the cooled CoM mode (red color) and uncooled Br mode (blue color) and their fitting by theoretical models (dashed lines) based on Eq. (4.46) as a function of frequency. In this graph, significant decrease and broadening of the peaks for CoM mode can be seen with increasing gain of the feedback loop. The values of Br mode peak remained almost the same. Furthermore, increasing crosstalk into the Br mode can be observed, which limits cooling efficiency at pressure 1 mbar.

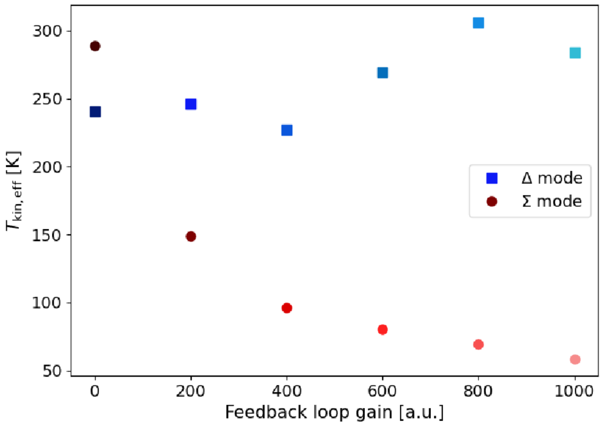

Figure 4.9: The dependence of the effective kinetic temperature on the feedback loop gain for both modes. The effective kinetic temperature of the uncooled Br mode fluctuates irregularly and does not have a clear distinct decrease here as in the case of the cooled CoM mode (red dots). Larger fluctuations in Br mode (blue squares) may be caused by crosstalk from the other mode. The lowest effective kinetic temperature 58.4 K for CoM mode was reached.

4.3.2. Cooling of the breathing mode only

In the case of cooling just Br mode, I set the cooling coefficient for CoM mode equal to zero ($c_\Sigma = 0$). The PSDs of both modes are shown in Fig. 4.10. A significant decrease and broadening can be observed only for the cooled Br mode, while the uncooled CoM mode has an approximately constant value. The crosstalk into the CoM mode, becomes stronger as the gain increases. When the gain is increased, both peaks shift to the right due to the feedback loop delay τ. In Fig. 4.11 the dependence of the effective kinetic temperature for both modes is shown, reaching a minimal value 96.7 K for the Br mode. The minimal reachable effective temperature is almost two times higher than in the case of CoM mode cooling at the same pressure. The final resonance frequencies and damping rates for both were $\omega_\Sigma/2\pi = 2.5 \cdot 10^4$ Hz for CoM mode, $\omega_\Delta/2\pi = 3.0 \cdot 10^4$ Hz for Br mode, $\xi_\Sigma/2\pi = 2.0 \cdot 10^2$ Hz for CoM mode and $\xi_\Delta/2\pi = 2.1 \cdot 10^2$ Hz.

4.3.3. Cooling of both modes simultaneously

Figure 4.12 shows the PSD of both simultaneously cooled modes for varying feedback loop gain. In this graph, one can see a significant decrease and broadening for peaks of both modes with increasing the feedback loop gain. Furthermore, stronger crosstalks into both modes appear with increasing feedback loop gain. As a result of these crosstalks, cooling of one mode with increasing gain can cause heating of the other mode. In the case of cooling of both modes, there is more effective cooling of the Br mode compared to the CoM mode for the same gain. One of the reasons may be stronger crosstalk from the Br mode to the CoM mode, causing more intense heating of the CoM mode. When the gain is increased, both peaks shift to the right due to the influence of the feedback loop delay τ. In Fig. 4.13 there is shown the decrease in an effective kinetic temperature for both modes. An effective kinetic temperature of 64.9 K for Br mode was reached and 87.2 K for CoM mode for the gain = 1000. The final resonance frequencies and damping rates

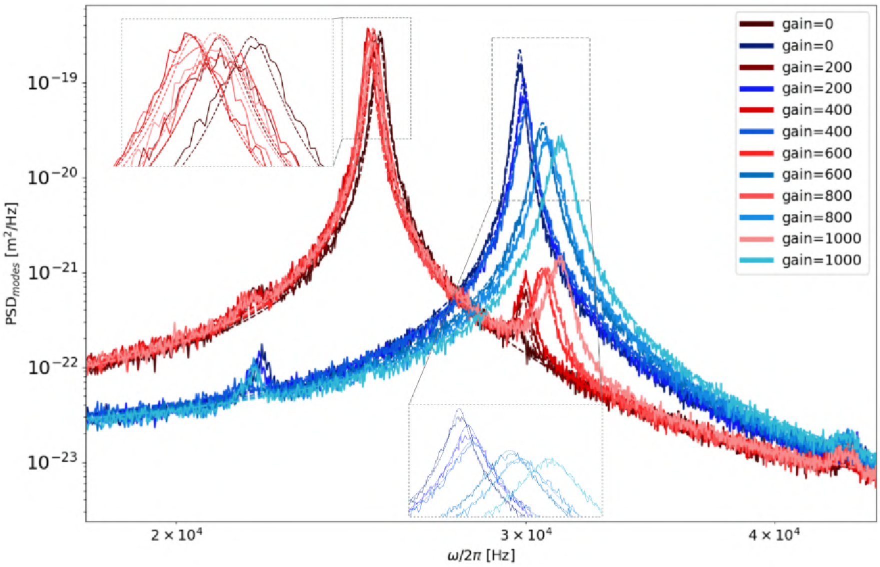

Figure 4.10: Calculated PSD of the cooled Br mode (blue color) and uncooled CoM mode (red color) and their fitting by theoretical models (dashed lines) based on Eq. (4.46) as a function of frequency. In this graph can one see a significant decrease and broadening of the peaks for Br mode with higher feedback loop gain. The values of a peak for CoM mode remained almost the same, but with the increasing gain, stronger crosstalk to the second mode occurs.

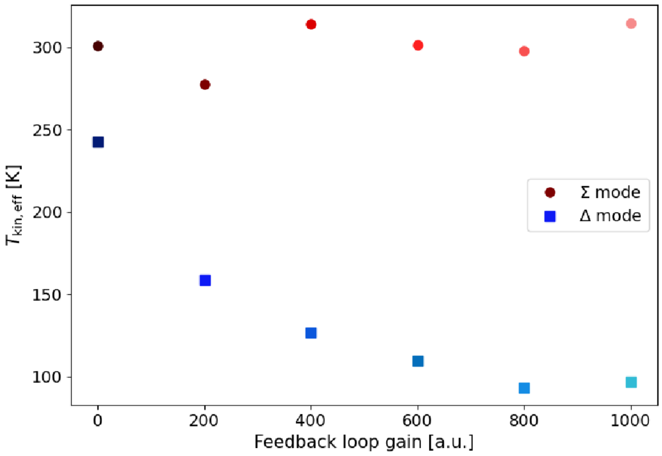

Figure 4.11: The dependence of effective kinetic temperature on the feedback loop gain for both modes. For uncooled CoM mode (red dots) the value is approximately constant, compared to the cooled Br mode (blue squares), where the temperature significantly decreases. In this case, there are also minor temperature fluctuations for CoM mode, compared to the previous cooling of Br mode. The minimal effective kinetic temperature 96.7 K was reached for Br mode.

for both were $\omega_\Sigma/2\pi = 2.5 \cdot 10^4$ Hz for CoM mode, $\omega_\Delta/2\pi = 3.0 \cdot 10^4$ Hz for Br mode, $\xi_\Sigma/2\pi = 2.0 \cdot 10^2$ Hz for CoM mode and $\xi_\Delta/2\pi = 2.1 \cdot 10^2$ Hz.

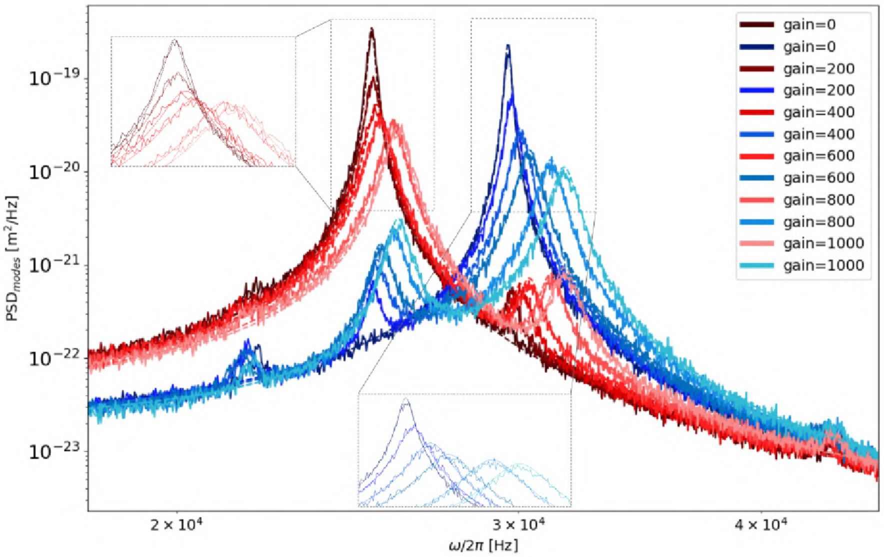

Figure 4.12: Calculated PSD of the cooling of both modes simultaneously and their fitting by theoretical models (dashed lines) based on Eq. (4.46) as a function of frequency. A significant decrease and broadening can be observed for both modes. When increasing the gain, however, there is again an increase in crosstalks in both modes, which limited their cooling.

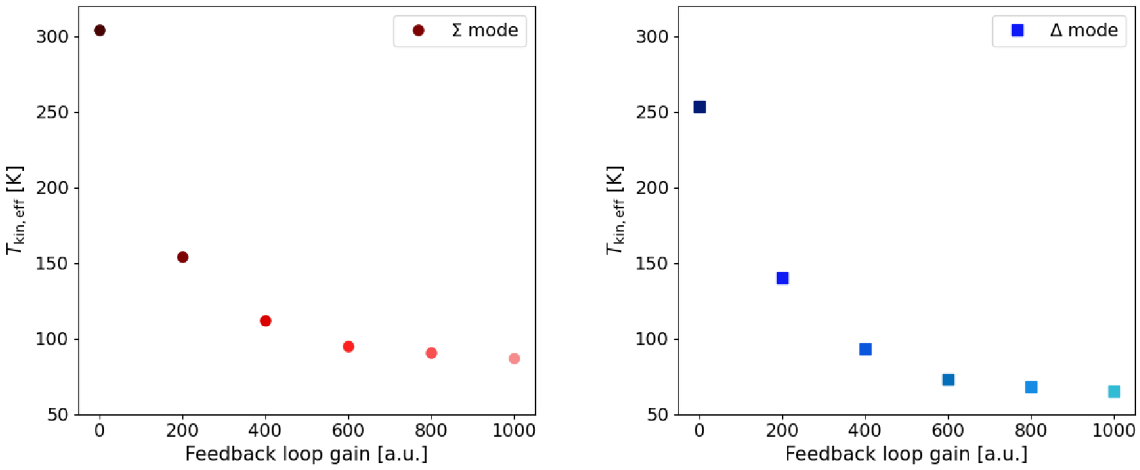

(a) (b)

Figure 4.13: The dependence of the effective kinetic temperature on the feedback loop gain for both modes. The temperature for both modes significantly decreases with increasing of feedback loop gain. The minimal effective kinetic temperature for Br and CoM mode was 64.9 K and 87.2 K, respectively.

5. Conclusion

As part of my diploma thesis, I expanded my theoretical knowledge and experimental skills in the field of optical micromanipulation and cooling of the thermal motion of optically levitating nanoparticles. I participated in the construction of an experimental set-ups that followed the objectives of the diploma thesis that can be seen in Figs. 2.7 and 3.7 for one particle and in Figs. 2.7 and 4.5 for two particles. The real appearance of the set-up is shown in Figs. 2.15 and 2.16. To carry out the cooling, I used the cold damping method, which uses an external electric force acting against the velocity vector of the trapped particle as shown in Fig. 3.3. This force can also be thought of as adding extra damping to the trapped particle system, thereby reducing the variance of its motion. I subsequently quantified the cooling by the introduction of the effective kinetic temperature, which was related to the variance of the particle position through the equipartition theorem (see Eqs. (2.23) and (4.49)).

As the first experimental test, I used the configuration of a laser beam with a circular lateral intensity profile and applied the cooling method on the particle thermal movement along the direction of the external electric field defined by the electrodes (x-axis). The results are shown in the PSD plots in Fig. 3.10 for the cooled axis and in Fig. 3.11 for the uncooled axis and in the plots of the probability density of the particle positions in Fig. 3.14. The experimental PSDs were fitted with the theoretical model and the parameters of the system and feedback were determined. I found very good agreement between the shape of the experimental power spectral densities (PSD) of particle positions with the theoretical ones and the lowest effective temperature of the cooled x-axis 13.5 K was reached whereas the y-axis stayed without a significant impact at the room temperature. Figures. 3.12(a) and 3.12(b) present values of the feedback loop time delay and gain determined from the fits and the loop delays reasonably well correspond to an independent determination.

In the second type of experiment, we extended the number of cooled axes to two and investigated the behavior of one particle in an elliptical lateral profile of the laser beam intensity (see Fig. 3.6). The main axes of such elliptical beam profile followed x- and y-axes that were now aligned at 45° with respect to the electric field. The beam formed optical traps along x- and y- axes where the particle oscillated at different frequencies. Two feedback loops, working at different frequencies of both particles, were applied and the suppression of the thermal motion of the particle along both axes was observed. A visible effect of such two-dimensional cooling along both axes are demonstrated for different gains of the feedback loop in the form of PSDs in Fig. 3.18, probability densities of particle positions in Fig. 3.22, and the kinetic effective temperatures in Fig. 3.21. The corresponding effective kinetic temperatures 14.0 K and 13.0 K were found for x and y-axis, respectively. This configuration also allowed switching off the cooling along one axis and such results along x-axis are presented in Section 3.7.1 in Figs. 3.15 – 3.17. Again, a significant cooling was reached, corresponding to the effective kinetic temperature 13.4 K.

The third modification of the experiment dealt with two particles levitating in two independent beams of the circular lateral intensity profile of the laser beams. The electric field was applied along the inter-particle axis. The detection path (see Fig. 4.5) was extended by one quadrant photodetector so that each particle was detected by its own detector. After finding the appropriate distance between the two particles, the normal modes were formed and were visible in the PSD plots (see theoretical Section 4.1.1). The feedback of the cold damping was applied to cool just one mode (see Figs. 4.8 and 4.9 for the center of mass mode CoM, and Figs. 4.10 and 4.11 for the breathing mode Br) or both modes simultaneously (see Figs. 4.12 and 4.13). For the first time we demonstrated that cold damping can cool simultaneously thermal motion of two particles, although the reached minimal effective temperatures were higher than in the 2D cooling of a single particle. For the CoM or Br mode, the effective kinetic temperature 58.4 K or 96.7 K was reached, respectively. In the case of simultaneous cooling of both modes, the temperatures were 87.2 K and 64.9 K for the CoM and Br mode, respectively. This is mainly caused by a crosstalk between the two modes, which limits the achievement of lower temperatures at relatively high pressure. The next experiments will be performed at lower pressures with more sophisticated control electronics.

All the measurements were also fitted with theoretical models and relevant parameters of the system were determined - damping of the ambient atmosphere, resonant frequency of the particle oscillations, effective temperature, parameters of the cold damping (gain and feedback loop time delay) etc. Found values corresponded appropriately to the expected experimental parameters.

The systematic experimental results obtained in my master's thesis can be used in designing advanced experiments aiming at approaching the quantum ground state of the center-of-mass oscillatory motion of optically levitated particles. The study of optical coupling of two simultaneously levitated particles can then form the basis for experiments directed towards investigation of quantum entanglement between mesoscopic objects.

Bibliography

[1] Ashkin, A.: Acceleration and trapping of particles by radiation pressure. *Phys. Rev. Lett.,* 24, 1970, p. 156–159. ISSN 0031-9007.

[2] Ashkin, A. and Dziedzic, J. M.: Optical levitation by radiation pressure. *Appl. Phys. Lett.,* 19, 1971, p. 283–285. ISSN 0003-6951.

[3] Ashkin, A. *et al.*: Observation of a single-beam gradient force optical trap for dielectric particles. *Opt. Lett.,* 11, 1986, p. 288–290. ISSN 0146-9592.

[4] Jones, P.H *et al.*: *Optical tweezers: Principles and applications*, Cambridge University Press, Cambridge, 2015. ISBN 978-9810240585.

[5] Ashkin, A.: *Optical trapping and manipulation of neutral particles using lasers.* World Scientific, London, 2006. ISBN 978-9810240585.

[6] Millen, J. *et al.*: Optomechanics with levitated particles. *Rep. Prog. Phys.,* 83, 2020, p. 026401. ISSN 0034-4885.

[7] Ranjit, G. *et al.*: Zeptonewton force sensing with nanospheres in an optical lattice. *Phys. Rev. A,* 93, 2016, p. 053801. ISSN 2469-9934.

[8] Tebbenjohanns, F. *et al.*: Quantum control of a nanoparticle optically levitated in cryogenic free space. *Nature,* 595, 7867, 2021, p. 378–382. ISSN 0028-0836.

[9] Magrini, L. *et al.*: Real-time optimal quantum control of mechanical motion at room temperature. *Nature,* 595, 7867, 2021, p. 373–377. ISSN 0028-0836.

[10] Ashkin, A. and Dziedzic, J.: Optical levitation in high vacuum. *Appl. Phys. Lett.,* 28, 1976, p. 333–335. ISSN 0003-6951.

[11] Yin, Z.-Q., Geraci, A. A., and Li, T.: Optomechanics of levitated dielectric particles. *Int. J. Mod. Phys. B,* 27, 2013, p. 1330018. ISSN 1793-6578.

[12] Gieseler, J. *et al.*: Subkelvin parametric feedback cooling of a laser-trapped nanoparticle. *Phys. Rev. Lett.,* 109, 2012, p. 103603. ISSN 0031-9007.

[13] Rondin, L. *et al.*: Direct measurement of Kramers turnover with a levitated nanoparticle. *Nat. Nanotechnol.,* 12, 2017, p. 1130. ISSN 1748-3395.

[14] Geraci, A. A., Papp, p. B., and Kitching, J.: Short-range force detection using optically cooled levitated microspheres. *Phys. Rev. Lett.,* 105, 2010, p. 101101. ISSN 0031-9007.

[15] Hebestreit, E. *et al.*: Sensing static forces with free-falling nanoparticles. *Phys. Rev. Lett.,* 121, 2018, p. 063602. ISSN 0031-9007.

[16] Novotny, L. and Hecht, B.: *Principles of nano-Optics.* Cambridge University Press, Cambridge, 2006. ISBN 1107005469.

[17] Zemánek, P. *et al.*: Optical trapping of Rayleigh particles using a Gaussian standing wave. *Opt. Commun.,* 151, 1998, p. 273–285. ISSN 0030-4018.

[18] Ashkin, A.: Forces of a single-beam gradient laser trap on a dielectric sphere in the ray optics regime. *Biophysical Journal,* 61, 1992, p. 569–582. ISSN 1542-0086.

[19] Jonáš, A. and Zemánek, P.: Light at work: The use of optical forces for particle manipulation, sorting, and analysis. *Electophoresis,* 29, 2008, p. 4813–4851. ISSN 0173-0835.

[20] Zemánek, P., Jonáš, A., and Liška, M.: Simplified description of optical forces acting on a nanoparticle in the Gaussian standing wave. *J. Opt. Soc. Am. A,* 19, 2002, p. 1025–1034. ISSN 1084-7529.

[21] Coffey, W. T., Kalmykov, Y. T., and Waldron, J. T.: *The Langevin Equation.* World Scientific, Singapore, 2004. ISBN 978-981-4355-66-7.

[22] Nørrelykke, p. F. and Flyvbjerg, H.: Harmonic oscillator in heat bath: Exact simulation of time-lapse-recorded data and exact analytical benchmark statistics. *Phys. Rev. E,* 83, 2011, p. 041103. ISSN 2470-0045.

[23] Goodman, J. W.: *Stastical optics.* John Wiley & Sons, 1985. ISBN 0-472-39926-7.

[24] Nørrelykke, p. F. and Flyvbjerg, H.: Power spectrum analysis with least-squares fitting: Amplitude bias and its elimination, with application to optical tweezers and atomic force microscope cantilevers. *Rev. Sci. Instrum.,* 81, 2010, p. 075103. ISSN 1089-7623.

[25] Gieseler, J. *et al.*: Optical tweezers — from calibration to applications: A tutorial. *Adv. Opt. Photon.* 13, 2021, p. 74–241. ISSN 1943-8206.

[26] Ren, Y.-X., Lu, R.-D., and Gong, L.: Tailoring light with a digital micromirror device. *Ann. Phys.* 527, 2015, p. 447–470. ISSN 0003-4916.

[27] Stuart, D., Barter, O., and Kuhn, A.: Fast algorithms for generating binary holograms. *arXiv*, p. 1409.1841, 2014.

[28] Lee, W.-H.: Computer generated holograms: techniques and applications. *Progress in Optics,* XVI, 1978, p. 121–229. ISSN 0079-6638.

[29] Turtaev, S. *et al.*: Comparison of nematic liquid-crystal and DMD based spatial light modulation in complex photonics. *Opt. Express,* 25, 2017, p. 29874–29884. ISSN 1094-4087.

[30] Conkey, D. B., Caravaca-Aguirre, A. M., and Piestun, R.: High-speed scattering medium characterization with application to focusing light through turbid media. *Opt. Express,* 20, 2012, p. 1733–1740. ISSN 1094-4087.

[31] Flajšmanová, J. *et al.*: Using the transient trajectories of an optically levitated nanoparticle to characterize a stochastic Duffing oscillator. *Scientific Reports,* 10, 2020, p. 14436. ISSN 2045-2322.

[32] Hebestreit, E. *et al.*: Calibration and energy measurement of optically levitated nanoparticle sensors. *Rev. Sci. Instrum.,* 89, 2018, p. 033111. ISSN 1089-7623.

[33] Penny, T. W., Pontin, A., and Barker, P. F.: Performance and limits of feedback cooling methods for levitated oscillators: A direct comparison. *Phys. Rev. A,* 104, 2021, p. 023502. ISSN 2469-9934.

[34] Jain, V. *et al.*: Direct Measurement of Photon Recoil from a Levitated Nanoparticle. *Phys. Rev. Lett.,* 116, 2016, p. 243601. ISSN 0031-9007.

[35] Iwasaki, M. *et al.*: Electric feedback cooling of single charged nanoparticles in an optical trap. *Phys. Rev. A,* 99, 2019, p. 051401. ISSN 2469-9934.

[36] Aspelmeyer, M., Meystre, P., and Schwab, K.: Quantum optomechanics. *Physics Today,* 65, 2012, p. 29–35. ISSN 1945-0699.

[37] Delić, U.: *Cavity cooling by coherent scattering of a levitated nanosphere in vacuum.* PhD thesis, University of Vienna, 2019. p.166.

[38] Aspelmeyer, M., Kippenberg, T. J., and Marquardt, F.: Cavity optomechanics. *Rev. Mod. Phys.* 86, 2014, p. 1391–1452. ISSN 0034-6861.

[39] Delić, U. *et al.*: Cavity cooling of a levitated nanosphere by coherent scattering. *Phys. Rev. Lett.,* 122, 2019, p. 123602. ISSN 0031-9007.

[40] Cohadon, P. F., Heidmann, A., and Pinard, M.: Cooling of a mirror by radiation pressure. *Phys. Rev. Lett.,* 83, 1999, p. 3174–3177. ISSN 0031-9007.

[41] Kleckner, D. and Bouwmeester, D.: Sub-kelvin optical cooling of a micromechanical resonator. *Nature,* 444, 2006, p. 75–78. ISSN 0028-0836.

[42] Poggio, M. *et al.*: Feedback cooling of a cantilever's fundamental mode below 5 mK. *Phys. Rev. Lett.,* 99, 2007, p. 017201. ISSN 0031-9007.

[43] Steixner, V., Rabl, P., and Zoller, P.: Quantum feedback cooling of a single trapped ion in front of a mirror. *Phys. Rev. A,* 72, 2005, p. 043826. ISSN 2469-9934.

[44] Bushev, P. *et al.*: Feedback cooling of a single trapped ion. *Phys. Rev. Lett.,* 96, 2006, p. 043003. ISSN 0031-9007.

[45] Pinard, M. *et al.*: Full mechanical characterization of a cold damped mirror. *Phys. Rev. A,* 63, 2000, p. 013808. ISSN 2469-9934.

[46] Tebbenjohanns, F. *et al.*: Cold damping of an optically levitated nanoparticle to microkelvin temperatures. *Phys. Rev. Lett.,* 122, 2019, p. 223601–6. ISSN 0031-9007.

[47] Conangla, G. P. *et al.*: Optimal feedback cooling of a charged levitated nanoparticle with adaptive control. *Phys. Rev. Lett.,* 122, 2019. p. 223602. ISSN 0031-9007.

[48] Press, W. H. *et al.*: *Numerical recipes in C.* Cambridge University Press, Cambridge, 1992. ISBN 0-521-43108-5.

[49] Dholakia, K. and Zemánek, P.: Gripped by light: Optical binding. *Rev. Mod. Phys.,* 82, 2010, p. 1767–1791. ISSN 0034-6861.

[50] Svak, V. *et al.*: Stochastic dynamics of optically bound matter levitated in vacuum. *Optica,* 8, 2021, p. 220–229. ISSN 2334-2536.

[51] Rieser, J. *et al.*: Tunable light-induced dipole-dipole interaction between optically levitated nanoparticles. *Science (New York, N.Y.)* 377, 2022, p. 987–990. ISSN 1095-9203.

[52] Liska, V. *et al.*: Cold damping of levitated optically coupled nanoparticles. *arXiv*, 2023, p. 2305.11809.

[53] Leite, I. T. *et al.*: Three-dimensional holographic optical manipulation through a high-numerical-aperture soft-glass multimode fibre. *Nat. Photonics,* 12, 2018, p. 33–39. ISSN 1749-4885.

List of abbreviations

1D – One-dimensional

2D – Two-dimensional

Br – Breathing mode

CD – Cold damping

CoM – Center of mass mode

CP – Cross-polarized

CPB – Counter-propagating beams

DMD – Digital micro-mirrors device

IPA – Isopropyl alcohol

ISI CAS – Institute of Scientific Instruments of the Czech Academy of Sciences

LASER – Light Amplification by Stimulated Emission of Radiation

LE – Langevin equation

MP – Microparticle

NA – numerical aperture

NP – Nanoparticle

OT – Optical tweezers

PSD – Power spectral density

QPD – Quadrant photodiode

SLM – Spatial light modulator

SW – Standing wave

VCH – vacuum chamber